iScience

CellPress
OPEN ACCESS

Article

Enzyme-Constrained Models and Omics Analysis of *Streptomyces coelicolor* Reveal Metabolic Changes that Enhance Heterologous Production

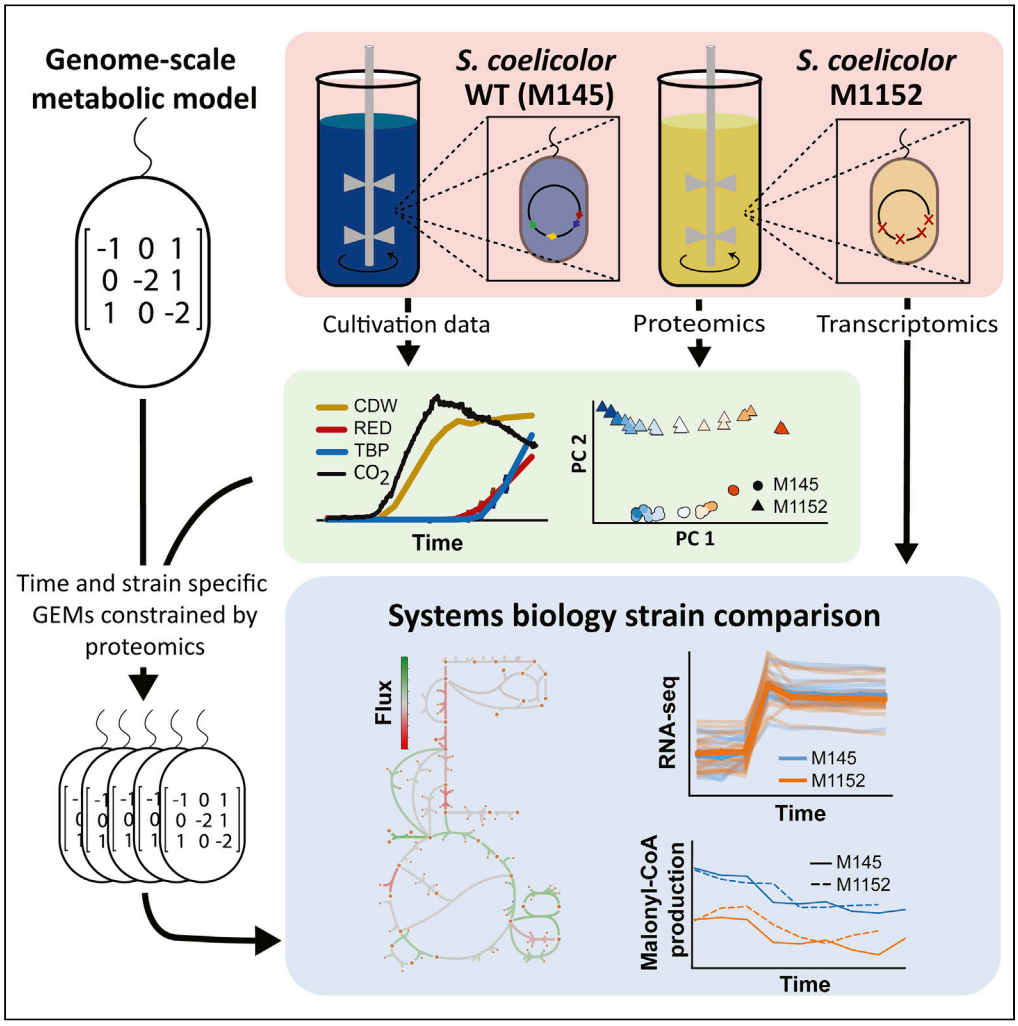

Snorre Sulheim, Tjaša Kumelj, Dino van Dissel, ..., Eivind Almaas, Alexander Wentzel, Eduard J. Kerkhoven

eduardk@chalmers.se

HIGHLIGHTS

Time-series transcriptomics and proteomics of S. coelicolor M145 and M1152

Application of GEM to interpret changes in the proteome on the systems level

Limited effect of improved precursor supply on enhanced production in M1152

Reduced rate of germicidin in M1152 suggests a need for other expression hosts

Sulheim et al., iScience *23*, 101525
September 25, 2020
https://doi.org/10.1016/j.isci.2020.101525

iScience

CellPress
OPEN ACCESS

Article

Enzyme-Constrained Models and Omics Analysis of *Streptomyces coelicolor* Reveal Metabolic Changes that Enhance Heterologous Production

Snorre Sulheim,[1,2] Tjaša Kumelj,[2] Dino van Dissel,[1] Ali Salehzadeh-Yazdi,[3] Chao Du,[4] Gilles P. van Wezel,[4] Kay Nieselt,[5] Eivind Almaas,[2,6] Alexander Wentzel,[1] and Eduard J. Kerkhoven[7,8,9,*]

SUMMARY

Many biosynthetic gene clusters (BGCs) require heterologous expression to realize their genetic potential, including silent and metagenomic BGCs. Although the engineered *Streptomyces coelicolor* M1152 is a widely used host for heterologous expression of BGCs, a systemic understanding of how its genetic modifications affect the metabolism is lacking and limiting further development. We performed a comparative analysis of M1152 and its ancestor M145, connecting information from proteomics, transcriptomics, and cultivation data into a comprehensive picture of the metabolic differences between these strains. Instrumental to this comparison was the application of an improved consensus genome-scale metabolic model (GEM) of *S. coelicolor*. Although many metabolic patterns are retained in M1152, we find that this strain suffers from oxidative stress, possibly caused by increased oxidative metabolism. Furthermore, precursor availability is likely not limiting polyketide production, implying that other strategies could be beneficial for further development of *S. coelicolor* for heterologous production of novel compounds.

INTRODUCTION

The bacterium *Streptomyces coelicolor* has been the *de facto* model actinomycete for the production of antibiotics. Being known for over 100 years, the interest in this organism predates the golden age of antibiotic research. With its complex life cycle, featuring mycelial growth and differentiation, spore formation, programmed cell death, and the ability to produce multiple colored secondary metabolites, it has assisted greatly in our understanding of how streptomycetes sense their surrounding (Hahn et al., 2002; Hutchings et al., 2004; Nothaft et al., 2010; Rigali et al., 2008; Sola-Landa et al., 2005), activate their developmental cycle (Chandra and Chater, 2014), and regulate the production of antibiotics (Nieselt et al., 2010; Thomas et al., 2012). Further aided by the publication of its genome sequence (Bentley et al., 2002), the antibiotic coelimycin P1 (yellow), produced from the formerly cryptic polyketide gene cluster known as *cpk*, was added to this list (Gomez-Escribano et al., 2012). Today, the widespread use of *S. coelicolor* continues as a host for heterologous production of biosynthetic gene clusters (BGCs) (Castro et al., 2015; Gomez-Escribano and Bibb, 2011, 2014; Kumelj et al., 2019; Thanapipatsiri et al., 2015; Yin et al., 2015). Heterologous expression is a powerful strategy for novel compound discovery from BGCs that are either natively silent or originate from an unculturable source (Nepal and Wang, 2019). These BGCs represent an untapped resource of microbial biodiversity, nowadays made evident and accessible due to recent advances within the fields of metagenomics, molecular biology, and bioinformatics (Rutledge and Challis, 2015).

The efficiency of *S. coelicolor* as a heterologous production host relies on a metabolism that has evolved to provide the necessary precursors to produce a broad range of complex molecules. Many of these molecules are produced when the strain is experiencing nutrient-limiting conditions that lead to growth cessation and complex re-modelling of its metabolism (Wentzel et al., 2012a). Metabolic switching in response to phosphate and glutamate depletion has been studied in detail at a variety of metabolic levels in *S. coelicolor* M145 (Nieselt et al., 2010; Thomas et al., 2012; Wentzel et al., 2012b), the most well-known wild-type strain devoid of the two plasmids SCP1 and SCP2 present in the parent strain *S. coelicolor* A3(2) (Kieser et al., 2000). This has unraveled a complex sequence of switching events that ultimately lead to the biosynthesis of calcium-dependent antibiotic (CDA), and the colored antibiotics actinorhodin

[1]Department of Biotechnology and Nanomedicine, SINTEF Industry, 7034 Trondheim, Norway

[2]Department of Biotechnology and Food Science, NTNU - Norwegian University of Science and Technology, 7491 Trondheim, Norway

[3]Department of Systems Biology and Bioinformatics, Faculty of Computer Science and Electrical Engineering, University of Rostock, 18057 Rostock, Germany

[4]Microbial Biotechnology, Institute of Biology, Leiden University, 2300 Leiden, the Netherlands

[5]Integrative Transcriptomics, Center for Bioinformatics, University of Tübingen, 72070 Tübingen, Germany

[6]K.G. Jebsen Center for Genetic Epidemiology, Department of Public Health and General Practice, NTNU - Norwegian University of Science and Technology, 7491 Trondheim, Norway

[7]Systems and Synthetic Biology, Department of Biology and Biological Engineering, Chalmers University of Technology, 412 96 Gothenburg, Sweden

[8]Novo Nordisk Foundation Center for Biosustainability, Chalmers University of Technology, 412 96 Gothenburg, Sweden

[9]Lead Contact

*Correspondence: eduardk@chalmers.se

https://doi.org/10.1016/j.isci.2020.101525

(Act, blue) and undecylprodigiosin (Red, red). The biosynthesis of coelimycin P1 occurs earlier than the three other compounds in the growth cycle and appears to be independent of the major metabolic switch (Nieselt et al., 2010).

To improve *S. coelicolor* M145 as a host for heterologous BGC expression, strain M1146 was created by the sequential deletion of its four major BGCs (*act, red, cda,* and *cpk*) (Gomez-Escribano and Bibb, 2011). This should increase precursor availability for the production of a whole range of heterologous products and provides a cleaner chromatographic background to more easily identify novel compounds. *S. coelicolor* M1152 is a derivative of M1146, which besides the deletion of the four main BGCs bears the C1298T point mutation in the *rpoB* gene that encodes the beta subunit of RNA polymerase. This mutation was shown to have strong positive effects on the production of various antibiotics (Gomez-Escribano and Bibb, 2011; Hu et al., 2002). Up to now, M1152 is a preferred general "superhost" for heterologous BGC expression (Braesel et al., 2019; Castro et al., 2015; Kepplinger et al., 2018; Li et al., 2013; Thanapipatsiri et al., 2015) and is the starting point for further strain development.

Previous research on the metabolism of *S. coelicolor* M1152 has been confined to transcriptome profiling of batch fermentations (Battke et al., 2010; Jager et al., 2011; Liao et al., 2014; Love et al., 2014; Mi et al., 2019), and further development of this strain as a "superhost" calls for a better understanding of how the genetic modifications have affected the regulatory system and metabolism of M1152. To this end we measure both protein and transcript levels of both M1152 and its parent strain, M145, at different time steps during batch fermentation where the metabolic switch is triggered by depletion of phosphate. As enzymes are catalyzing most metabolic transformations, assessing protein abundance provides information about the metabolic capacity of the organism. Furthermore, we do not only consider the protein abundances in isolation but also use these measurements to confine fluxes predicted by a genome-scale metabolic model (GEM) of *S. coelicolor* to the maximum capacity of the enzymes. By doing so we propagate differences in the abundance of individual enzymes in M145 and M1152 to metabolic rearrangements on the systems level.

The metabolic network in the cell is described in a GEM (Gu et al., 2019). GEMs are valuable resources of strain-specific knowledge, mathematical models able to predict steady-state flux distributions, and frameworks for interpretation and integration of different "omics" data, e.g., transcriptomics and proteomics (Robinson and Nielsen, 2016). The increased interest in using genome-scale models of *S. coelicolor* is conspicuous. Since the first reconstruction in 2005 (Borodina et al., 2005) five GEMs have been published (Alam et al., 2010; Amara et al., 2018; Kim et al., 2014; Kumelj et al., 2019; Wang et al., 2018), including three in 2018: iKS1317 (Kumelj et al., 2019), Sco4 (Wang et al., 2018), and iAA1259 (Amara et al., 2018). In addition, as a model organism for the *Actinomycetes,* the GEMs of *S. coelicolor* are frequently used as template for model development of closely related strains (Mohite et al., 2019), such as *Streptomyces clavuligerus* (Toro et al., 2018), *Saccharopolyspora erythraea* (Licona-Cassani et al., 2012) and *Streptomyces lividans* (Valverde et al., 2018). The recent updates of the *S. coelicolor* GEM were developed in parallel by different research groups: although all groups share the common interest of utilizing a high-quality model for predictions and data analysis, the prevailing approach of independent parallel development is inefficient. In addition to duplicating a considerable amount of work, lack of common standards for documentation of progress and issues, evaluation of model performance, as well as the use of different annotations makes it cumbersome to compare and merge models.

To increase the rate and quality of model reconstruction, in this study two research groups of the *S. coelicolor* GEM community, responsible for two of the latest model updates (Kumelj et al., 2019; Wang et al., 2018), have joined forces to merge existing GEMs of *S. coelicolor* into one consensus model that is publicly hosted on GitHub and can be continuously updated and improved by all members of the community. Hosting the model on GitHub has many advantages: (1) open access and contribution, (2) version control, (3) continuous development and integrated quality control with memote (Lieven et al., 2020), (4) new improvements released instantly (no publication lag time), and (5) complete documentation of model reconstruction. Such an approach has historic precedents: model reconstruction as a community effort has been a success for the human GEM (Thiele et al., 2013), baker's yeast (Aung et al., 2013; Dobson et al., 2010; Heavner et al., 2012, 2013; Herrgard et al., 2008; Lu et al., 2019), and Chinese hamster ovary cells (Hefzi et al., 2016). The recent developments in *S. coelicolor* model and strain improvements in different research groups prove that it is an opportune time now to join forces in the *Streptomyces* modeling efforts as well.

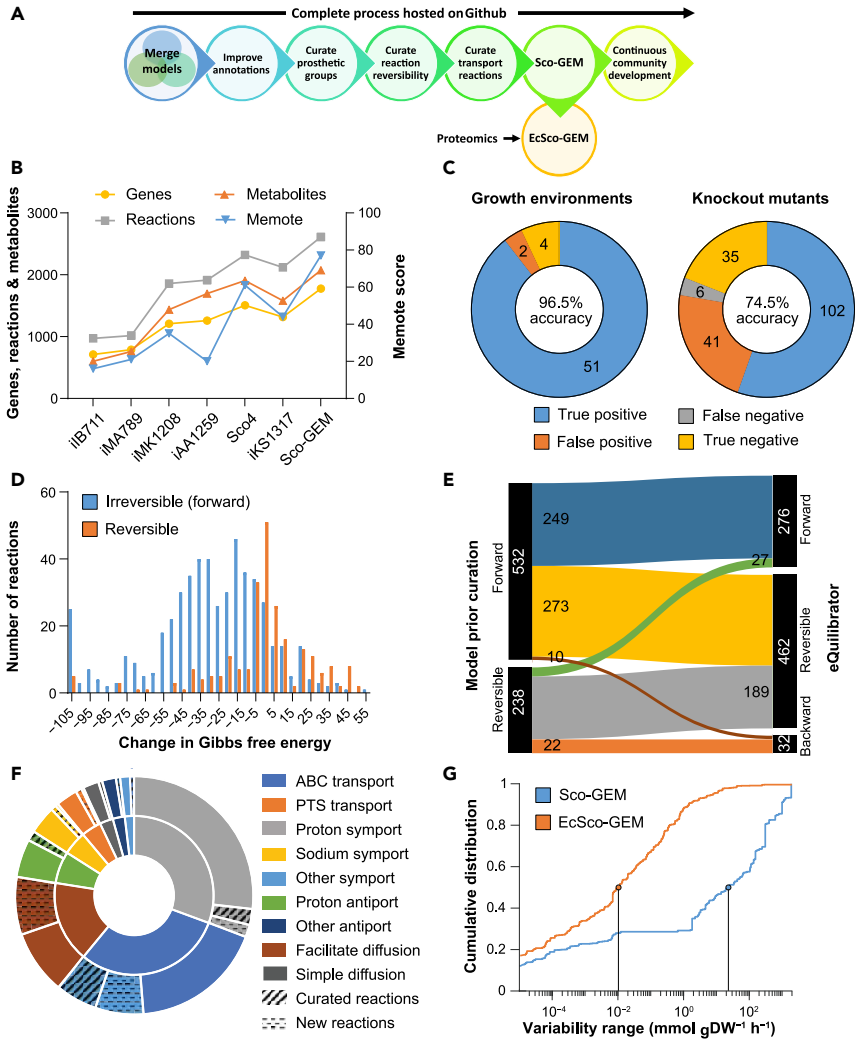

Figure 1. Sco-GEM Development and Analysis

(A) Schematic overview of the various steps in the Sco-GEM reconstruction process.

(B) The overall memote score and number of genes, reactions, and metabolites for the seven published *S. coelicolor* GEMs.

(C) Assessment of the model quality by comparing *in vivo* observations with *in silico* predictions across in total 241 tests: accuracy = 0.80; sensitivity = 0.96; specificity = 0.48; Matthews correlation coefficient = 0.53.

(D) The change in Gibbs free energy for 770 reactions that were annotated as either reversible or forward (i.e., forward irreversible) in the model before curation of reaction reversibility. The histogram is truncated at −105 kJ/mol, and more negative values are assigned to the leftmost bin.

(E) Analysis and comparison of the directionality and reversibility of reactions before curation and the direction inferred from the change in Gibbs free energy as estimated by eQuilibrator. Reactions labeled "forward" or "backward" are irreversible.

(F) Overview of the 369 transport reactions included in Sco-GEM, whereof 42 were curated and 65 were added during this work. The inner ring categorizes the reactions into nine different subgroups, whereas the outer ring displays the amount of curated and added reactions within each category. In the outer ring, the sections representing curated and new reactions are hatched and dotted, respectively.

(G) Comparison of cumulative flux variability distributions in Sco-GEM and EcSco-GEM.

RESULTS

Reconstruction of the Consensus Genome-Scale Model of *S. Coelicolor*

We conducted a stepwise reconstruction of Sco-GEM, the consensus genome-scale metabolic model of *S. coelicolor*, while tracking development using Git for version control (Figure 1A, Data S1, Table 1).

Sco-GEM is the most comprehensive and highest quality GEM of this organism (Figure 1B), comprising 1,777 genes, 2,612 reactions, 2,073 metabolites, and a memote score of 77%, which is indicative of the overall model quality (Lieven et al., 2020). Sco-GEM features an accuracy of 96.5% and 74.5% (Figure 1C) in predicting correct phenotypes for growth environments and knockout mutants, respectively, yielding in total a Matthews coefficient of correlation of 0.53 with the test data previously described (Kumelj et al., 2019).

With the recently published iKS1317 model (Kumelj et al., 2019) as a starting point, Sco-GEM was first developed by including genes, reactions, and metabolites from the equally recently published models iAA1259 (Amara et al., 2018) and Sco4 (Wang et al., 2018). The curations from iAA1259 were primarily related to coelimycin P1, butyrolactone, xylan, and cellulose pathways, whereas the 377 reactions added to Sco-GEM from Sco4 were scattered across a large range of different subsystems, covering both primary and secondary metabolism (Figure S1). Subsequent to merging the existing *S. coelicolor* GEMs, we performed a number of further curations of the model (Figure 1A): including improvement of annotations, both in terms of coverage and number of different databases, e.g., KEGG (Kanehisa, 2000; Kanehisa et al., 2019), BioCyC (Karp et al., 2019), ChEBI (Hastings et al., 2016), and MetaNetX (Moretti et al., 2016). All reactions and metabolites have been given identifiers according to the BiGG namespace (King et al., 2016), and all reactions are categorized into 15 different subsystems, covering 128 different pathways.

The biomass composition was curated to reflect estimated levels of prosthetic groups that are associated to cellular proteins. Proteomics data, as discussed later, were used to estimate protein levels, while UniProt (The UniProt Consortium, 2019) provided annotations of proteins with prosthetic groups, which was used to estimate overall prosthetic group levels (Data S1, Table 2).

Reaction Reversibility Updated for Almost a Third of Queried Reactions

The determination of reaction directionality and reversibility is an important step in a GEM reconstruction (Thiele and Palsson, 2010). However, the thermodynamic consistency of reactions was not considered in previous *S. coelicolor* models. We calculated Gibbs free energy changes for 770 of the 2,612 model reactions (Data S1, Table 3) using eQuilibrator (Flamholz et al., 2012) and found hardly any consistency between the calculated change in Gibbs free energy and the reversibility previously assigned to the model reactions (Figure 1D). To address this issue we decided to reassign the reversibility of the model reactions by using a relatively lenient threshold of −30 kJ/mol to classify a reaction as irreversible (Bar-Even et al., 2012; Feist et al., 2007), with the intent not to over-constrain the model (Figure 1E). The proposed changes in reversibility were evaluated against growth and knockout data (Kumelj et al., 2019), discarding 61 of the 332 proposed reactions, and consequentially, the flux bounds of 271 reactions were modified (see Transparent Methods). In addition, all ATP-driven reactions were manually curated and generally assumed irreversible unless they had an estimated positive change in Gibbs free energy or were known to be reversible. Examples of this include nucleoside diphosphate kinase (Chakrabarty, 1998) and ATP synthase (Yoshida et al., 2001). The manual curation of ATP-driven reactions led to a change in reversibility for 56 reactions.

Curation of Transport Reactions

As transport reactions have previously not been extensively curated in *S. coelicolor* models, we performed a thorough curation of transporters by querying various databases and BLAST analysis as detailed in Methods. This culminated in adding 43 new transport reactions and updating 39 of the 262 existing reactions in Sco-GEM (Figure 1F; Data S1, Table 4). The majority of the transporters comprise primary active transport proteins and secondary carriers (46%), in accordance with previous work (Getsin et al., 2013). Most primary active transporters are ATP-binding cassette (ABC) transporters (30%), whereas proton symports (30%) dominate the secondary carriers.

Development of the Enzyme-Constrained Model EcSco-GEM

To include explicit constraints regarding enzymes catalyzing metabolic reactions, the GECKO formalism (Sanchez et al., 2017) was applied to consider that catalyzing capacity is constrained by enzyme turnover rates (k_{cat}) and abundances. The GECKO toolbox modifies the structure of an existing GEM to integrate turnover rates and proteome data. Consequentially, this constrains the range of estimated fluxes to a biologically feasible range as determined by the amount and efficiency of each enzyme. Note that this approach regards the maximum catalytic activities but does not consider other kinetic parameters such as affinity constants. The overall flux variability of the resulting enzyme-constrained model (EcSco-GEM) is drastically reduced compared with the classic genome-scale model (Figure 1G), particularly due to the

considerably reduced fraction of reactions that have very high (10^1) flux variability. As reactions with high variability result in low certainty in the estimated fluxes, the observed reduction in flux variability is therefore a qualitative measure of the increased accuracy achieved by constraining the range of possible fluxes to those satisfying the limitation in protein allocation.

In our endeavor to describe the metabolic differences between M145 and M1152 we generated in total 17 time- and strain-specific enzyme-constrained models by combining EcSco-GEM with estimated growth, secretion, and uptake rates, as well as proteome data from cultivations that are detailed and analyzed later in the article.

Framework for Further Development of Sco-GEM by the Community

The Sco-GEM model is hosted as an open repository as suggested by memote, a recently developed tool for transparent and collaborative model development (Lieven et al., 2020). The memote tool is incorporated in the repository through Travis CI and tracks the model development on every change of the model. Sco-GEM v1.2.0 achieved a memote score of 77%, which is superior to that achieved by any previous model of *S. coelicolor* (Figure 1B; Supplemental Information).

Hosting Sco-GEM on GitHub with memote integration ensures continuous quality control and enables public insight into all aspects of model reconstruction and curation: any user can report errors or suggest changes through issues and pull requests. As contributions to the model development are fully trackable and can therefore be credited fairly, Sco-GEM is positioned as a community model that we envision to be continuously updated and widely used by the *S. coelicolor* research community. Although the major steps of model reconstruction have been detailed in the preceding sections, every detail of the process and every iteration of the model is accessible on the public model repository at https://github.com/SysBioChalmers/Sco-GEM.

In the remaining parts of the Results section, we have applied Sco-GEM along with transcriptome and proteome data, to study and compare the responses of *S. coelicolor* M145 and M1152 to phosphate depletion on a systems level and for the first time provide detailed insight into the distinct physiological features of engineered "superhost" strain M1152, which will be of value for its further development.

Random Sampling of Enzyme-Constrained GEMs Capture Metabolic Rearrangements in Response to Phosphate Depletion in M145

To evaluate whether the (Ec)Sco-GEM models can simulate behaviors of *S. coelicolor* metabolism, we analyzed time course sampled cultivations of secondary metabolite-producing strain M145 using the generated models. For this purpose, *S. coelicolor* M145 was cultivated in batch fermentations using standardized protocols reported earlier (Wentzel et al., 2012a). Cultures were sampled for "omics" data, as well as substrate utilization and secondary metabolite measurements to identify regulatory, proteomic, and metabolic changes during the metabolic switch. The online and offline measurements showed that phosphate depletion in the cultivation medium was reached approximately 35 h after inoculation. Shortly after, the culture growth ceased, and first Red and subsequently Act were detected in the culture medium (Figures 2A and 2B). Act levels were determined by measuring the amount of total blue pigments because this covers both the intracellular and secreted variants of actinorhodin, and is considered to be the preferred method (Bystrykh et al., 1996; Wentzel et al., 2012a). Both D-glucose and L-glutamate were consumed concomitantly, and their consumption continued after phosphate depletion, whereas both remained in excess until the end of cultivation. Note that *Streptomyces* can utilize intracellular phosphate storages after the medium is phosphate depleted (Smirnov et al., 2015). The RNA sequencing (RNA-seq) and untargeted proteomic data were analyzed in the light of previous studies (Nieselt et al., 2010; Thomas et al., 2012) and were in good agreement with data previously obtained from microarrays or targeted proteomics (Alam et al., 2010; Nieselt et al., 2010) (Figures 2C and S2). This confirmed the high reproducibility of the experiments across independent cultivations and high reliability of the chosen cultivation and analytic procedures (Figure 2).

The proteome data and calculated uptake/secretion rates (Table S1) were incorporated into EcSco-GEM to yield time-specific metabolic models of M145, giving insight on the changes occurring in the metabolic activity of different pathways during batch cultivation. Metabolic fluxes were estimated using an unbiased approach of random sampling, as alternative to optimization of a well-defined cellular objective used in flux balance analysis (Orth et al., 2010). It is possible that *S. coelicolor* is wired to maximize its growth

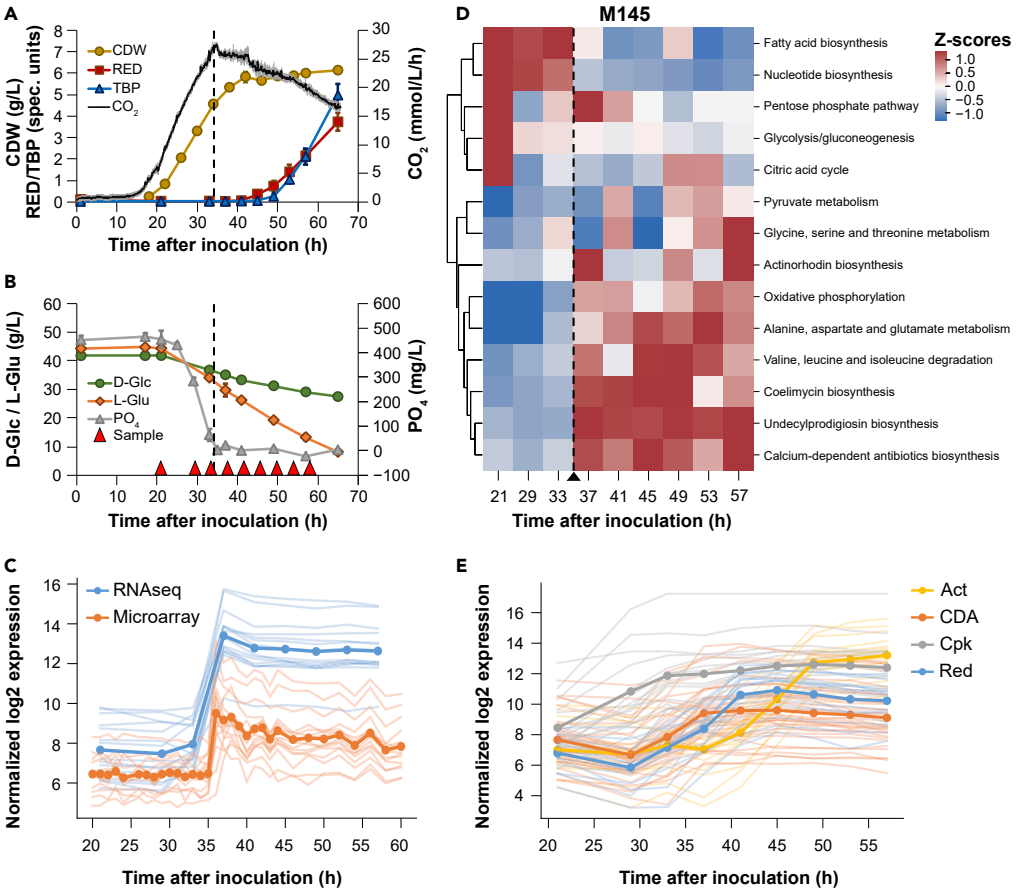

Figure 2. Batch Cultivation of *S. Coelicolor* M145 and the Effect of Phosphate Depletion

(A and B) Compounds produced (A) and consumed (B) during batch fermentation of *S. coelicolor* M145. Time points for sampling for transcriptome and proteome analysis are indicated with red triangles. The dashed vertical line indicates when phosphate in the medium has been depleted. Error bars are standard deviations of three biological replicates. CDW, cell dry weight; Red, undecylprodigiosin; TBP, total blue pigments/actinorhodins; CO_2, volume-corrected respiration; D-Glc, D-glucose; L-Glu, L-glutamate; PO_4, phosphate.

(C) Comparison of previously published microarray data (Nieselt et al., 2010) and RNA-seq data (this study) for genes previously found to respond to phosphate depletion (Nieselt et al., 2010). The transparent lines correspond to individual genes, whereas the bold lines represent the average expression level for each dataset.

(D) Clustered heatmap of CO_2-normalized *Z* scores for each of the top 10 varying pathways plus the pathways for the four major BGCs in M145, as revealed by simulations with the proteomics-integrated EcSco-GEM model. The pathways are sorted based on hierarchical clustering to facilitate visual interpretation of similarity between pathways. The dashed vertical line indicates the time point of the metabolic switch.

(E) RNA-seq data of the four major BGCs show the onset of biosynthesis of actinorhodin (Act), calcium-dependent antibiotic (CDA), coelimycin P1 (Cpk), and undecylprodigiosin (Red) at different time points during the batch fermentations of M145.

rate before phosphate depletion, but after the metabolic switch, it is difficult to define a clear cellular objective. We applied an approach that samples the vertices of the solution space (Bordel et al., 2010) and used their mean values to compare the metabolic fluxes between the two strains and between different time points. The variation in predicted fluxes through different pathways in M145 is an initial validation of the approach (Figure 2D): the most drastic change in fluxes occur in response to phosphate depletion, in agreement with observations in the transcriptome, metabolome, and proteome (Nieselt et al., 2010; Thomas et al., 2012; Wentzel et al., 2012b).

The response to phosphate depletion from the medium is achieved by a set of genes, positively regulated by PhoP, that are involved in phosphate scavenging, uptake, and saving (Martin et al., 2012; Martin-Martin

et al., 2018; Sola-Landa et al., 2003). In our cultivations the metabolic switch can be readily identified from the RNA-seq data by the rapid upregulation of this regulon after 35 h of cultivation in M145 (Figure 2C), thereby corroborating the model simulations (Figure 2D) and providing a more detailed picture of the underlying regulation. PhoP also represses nitrogen assimilation (Martin et al., 2017), which can partly explain the change in amino acids metabolism after phosphate depletion (Figure 2D). Indeed, from the RNA-seq data we find that glutamate import, the glutamate sensing system *gluR-gluK* (Li et al., 2017), *glnR* (Fink et al., 2002), and *glnA* are downregulated immediately subsequent to phosphate depletion (Figure S3). As PhoP is also known to regulate negatively the biosynthesis of secondary metabolites, the switching of its expression likely delays these pathways (Martin, 2004; Martin et al., 2017). However, after 37 h of cultivation the upregulation of the *cda* and *red* genes was observed, whereas that of the *act* genes was initiated at 41 h (Figure 2E). Production of Red and Act was measurable in the culture medium after 41 and 49 h of cultivation, respectively (Figure 2A). The enzyme-constrained models predict an immediate increase in fluxes through the biosynthetic pathways for the four main compounds Act, Red, CDA, and coelimycin P1 after the metabolic switch (Figure 2D).

The Onset of Secondary Metabolism Is Strongly Correlated with an Increase in Oxidative Phosphorylation and a Decrease in Fatty Acid Biosynthesis in M145

The metabolic switch was shown to be correlated with an enhanced degradation of branched-chain amino acids (valine, leucine, and isoleucine), an increase in oxidative phosphorylation, and a decrease in fatty acid biosynthesis (Figures 2D and S4). An active oxidative phosphorylation relies on an active tricarboxylic acid (TCA) cycle that generates reduced co-factors whose re-oxidation by the respiratory chain generates a proton gradient that drives ATP synthesis by the ATP synthase. The feeding of the TCA cycle requires acetyl-CoA, as well as nitrogen. Nitrogen likely originates from degradation of glutamate and branched-chain amino acids, whereas acetyl-CoA likely originates from glycolysis, as well as from the degradation of these amino acids as previously demonstrated (Stirrett et al., 2009). Indeed, the model predicts an increased flux through citrate synthase feeding acetyl-CoA into the TCA cycle (Figure S5A). The predicted increase in oxidative phosphorylation is supported by the RNA-seq data showing upregulation of enzymes belonging to the respiratory chain (Figure S5B). This is consistent with the clear correlation previously reported between high ATP/ADP ratio, resulting from an active oxidative phosphorylation, and actinorhodin production (Esnault et al., 2017). Furthermore, the consumption of acetyl-CoA by the TCA cycle to support the oxidative metabolism logically impairs fatty acids biosynthesis (Esnault et al., 2017).

The pentose phosphate pathway provides the main redox cofactor NADPH for polyketide biosynthesis, as well as to combat oxidative stress, and its model-predicted flux increase upon initiation of polyketide synthesis (Figure 2D) is in agreement with previous studies (Borodina et al., 2008; Jonsbu et al., 2001). A clear positive correlation was also noticed between the biosynthesis of alanine, aspartate, and glutamate, which are precursors for CDA and/or coelimycin P1 (Figure 2D), and the biosynthesis of these antibiotics. Similar observations were made in the antibiotic-producing *Amycolatopsis sp.* (Gallo et al., 2010). Our EcSco-GEM model proved to be in good agreement with previously reported findings, indicating that it is able to capture *S. coelicolor* metabolic behavior.

Model-Assisted Characterization of Engineered *S. Coelicolor* M1152 and Its Responses to Phosphate Depletion

As detailed earlier, EcSco-GEM shed a new light on the metabolic switch in secondary metabolite-producing strain M145. *S. coelicolor* M1152 (Gomez-Escribano and Bibb, 2011) is an M145 derivative devoid of the four major BGCs and bearing a point mutation in the *rpoB* gene. A better systemic understanding of M1152 metabolism would benefit to its further development as a performing host. To do so, a comparative analysis of gene expression levels and metabolic fluxes was carried out in the strains M145 and M1152.

Batch cultivations of M1152 were performed using identical conditions and comparable sampling regimes as for M145 reported earlier. This enabled a direct comparison of the two strains at a systems level, revealing both expected and unexpected effects of the strains' genetic differences (Figure 3). As anticipated, the products of the Cpk, CDA, Red, and Act biosynthetic pathways were undetectable in M1152 (Figure 3A). As previously observed (Gomez-Escribano and Bibb, 2011), the growth rate of M1152 is reduced compared with M145 (0.15 h^{-1} versus 0.21 h^{-1} in the initial exponential growth phase), delaying phosphate depletion by M1152 to 47 h after inoculation (Figure 3B), 12 h after M145 (Figure 2B).

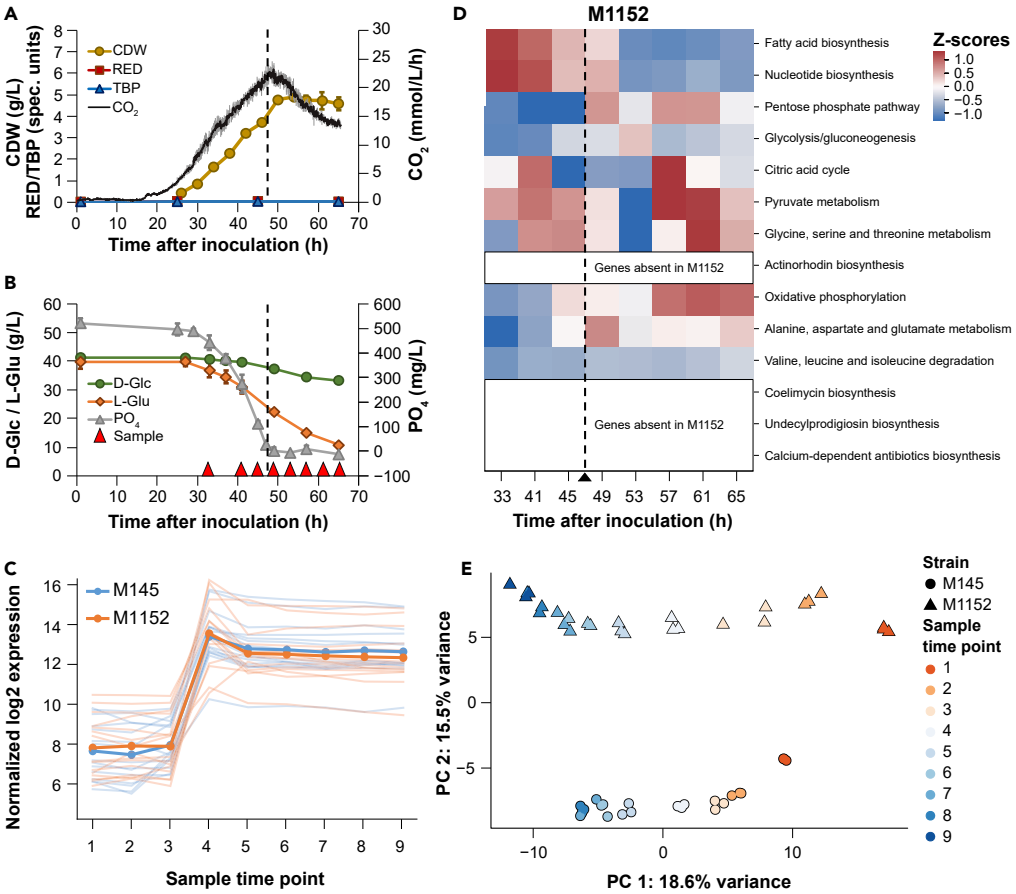

Figure 3. Batch Cultivation of *S. Coelicolor* M1152

(A and B) Compounds produced (A) and consumed (B) during batch fermentation of *S. coelicolor* M1152. Time points for sampling for transcriptome and proteome analysis are indicated with red triangles. The dashed vertical line indicates when phosphate in the medium has been depleted. Error bars are standard deviations of three biological replicates. CDW, cell dry weight; Red, undecylprodigiosin; TBP, total blue pigments/actinorhodins; CO_2, volume-corrected respiration; D-Glc, D-glucose; L-Glu, L-glutamate; PO_4, phosphate.

(C) Alignment of sample time points of M145 and M1152 cultivations based on the expression profiles of genes that were earlier found to respond to phosphate depletion with respect to the metabolic switch (Nieselt et al., 2010).

(D) Principle-component analysis of the proteomics data for M145 (triangles) and M1152 (circles), for each time point and culture. The first principal component separates the time points, whereas the second principal component separates the two strains.

(E) CO_2-normalized *Z* scores of pathway fluxes predicted by EcSco-GEM for 10 of the most varying pathways in M145 and M1152. To make this heatmap comparable to the results for M145 (Figure 2D), the data are standardized for both strains simultaneously and the row order is identical.

The sampling time points for proteome and transcriptome were adjusted accordingly (Figure 3B), enabling pairwise comparison of measurements between the two strains. Genes responsive to phosphate depletion, members of the PhoP regulon (Nieselt et al., 2010), were used to align the different sample datasets for M145 or M1152 (Figure 3C). Principle-component analysis of the proteome data confirms high consistency between corresponding biological replicates and incremental changes between sample points for both M145 and M1152 (mainly explained by principal component 1 (PC1): 18.6% variance, Figure 3E). A clear strain-dependent clustering of the data (PC2: 15.5% variance) indicates globally significant differences at the protein level. EcSco-GEM was subsequently used to create time-specific metabolic models from proteome data and estimated rates (Table S2) and predict metabolic changes in M1152. Interestingly we find that most patterns in M145 are retained in M1152 (Figure 3D): fatty acid and nucleotide biosynthesis is still downregulated after phosphate depletion, and similar trends of upregulation at later time points are observed for oxidative phosphorylation, glycine, serine and threonine, and pyruvate metabolism. It is

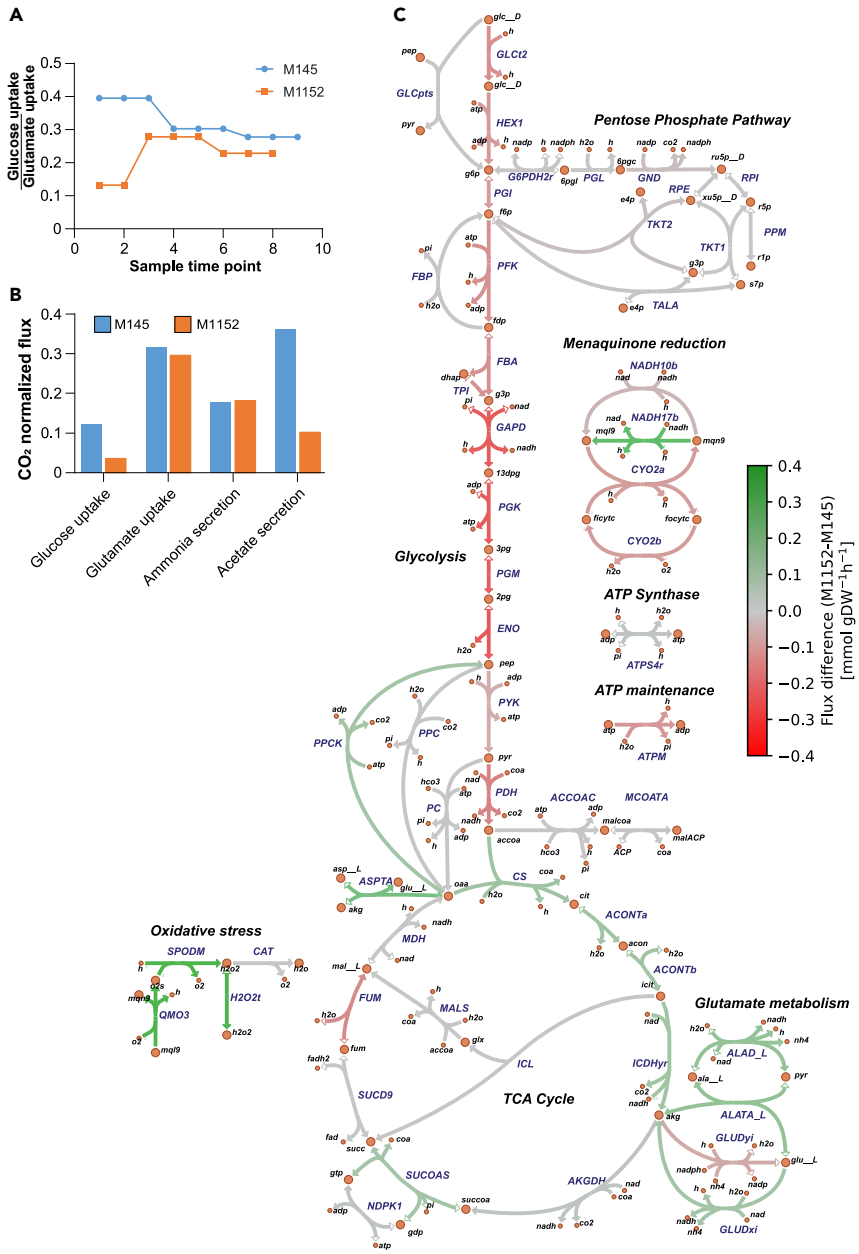

Figure 4. Predicted Carbon Fluxes in M145 and M1152

(A) The ratio between estimated uptake rates of glucose and glutamate for each sample time point for M145 and M145 shows that M1152 acquires a smaller part of its carbon from glucose compared with M145.

(B) Bar chart showing CO_2-normalized fluxes for the second sampling time point for M145 and M1152, i.e., after 29 and 41 h, respectively. There is a clear difference in the uptake of glucose and production of acetate, whereas the rates are comparable for the consumption of glutamate and secretion of ammonium.

(C) Comparison of predicted fluxes for the second sampling time points shows clear differences between the two strains in their relative utilization of the glycolysis and TCA cycle. The strength of the color of the lines corresponds to the flux difference between the strains; green reactions have higher flux in M1152, and red reactions have higher flux in M145.

striking that the upregulation of the branched-chain amino acid degradation and the alanine, aspartate, and glutamate metabolism seen as a response to phosphate depletion in M145 are absent in M1152.

The different glutamate and glucose consumption rates of M145 and M1152 (Figures 4A and 4B) resulted in substantial metabolic differences between the two strains before phosphate depletion. During cultivation

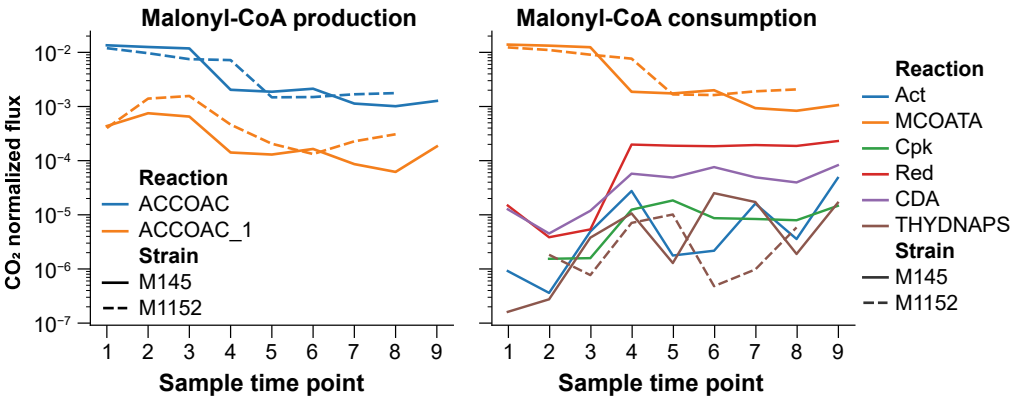

Figure 5. Production and Consumption of Malonyl-CoA as the Branching Point between Fatty Acid Biosynthesis and Production of Polyketides

Both panels display CO_2-normalized fluxes for both M145 and M1152 for all sampling time points as predicted by EcSco-GEM. The left panel shows the sources of malonyl-CoA, namely, acetyl-CoA carboxylase (ACCOAT; blue) and acetyl-CoA carboxytransferase (ACCOAT_1; orange). We observe a downregulation of the malonyl-CoA production after the metabolic switch (between time points 3 and 4) in both strains. The right panel presents reactions consuming malonyl-CoA. The consumption is dominated by malonyl-CoA-ACP transacylase (MCOATA) leading to biosynthesis of fatty acids. The other drains for malonyl-CoA are the pathways encoded by the four major BGCs (Act, Cpk, Red, and CDA) in addition to biflaviolin synthase (THYDNAPS).

on SSBM-P medium, where glutamate is the sole nitrogen source, glucose and glutamate are co-consumed. M1152, as M1146 (Esnault et al., 2017), has an increased growth yield on glucose compared with M145 (Figure S6). It thus obtains a larger share of its carbon from glutamate (Figures 4A and 4B) and has consequently also a higher nitrogen availability than M145. The increased nitrogen availability does, however, not increase the secretion of ammonium, indicating that the consumed nitrogen is directed toward growth or production of secondary metabolites. A reduced flux through glycolysis has also been reported previously for strain M1146 (Coze et al., 2013). This might be an effect of the predicted increased concentration of ATP in M1146 compared with M145, which inhibits glucose uptake and phosphofructokinase (Coze et al., 2013; Esnault et al., 2017). As Act was proposed to act as an electron acceptor reducing the efficiency of the oxidative phosphorylation, it is suggested that the lack of Act in M1146 causes the elevated ATP levels (Esnault et al., 2017). However, we find the largest difference in glycolytic flux at early time points, before phosphate depletion and Act production in M145, proving that Act itself cannot explain this observation.

The EcSco-GEM predicts the consequences of the reduced glucose uptake of M1152 on its central carbon metabolism, as displayed by mapping relative reaction fluxes from the second sampling time point onto a map of the central carbon metabolism in *Streptomyces* (Figure 4C). The map is based on the reaction network in Sco-GEM and created using Escher (King et al., 2015). A less-active glycolysis in M1152 than in M145 leads to a lower carbon flow toward acetyl-CoA and thus lower excretion of acetate compared with M145 (Figure 4B). Furthermore, EcSco-GEM reveals an increased flux from glutamate to alpha-ketoglutarate. Indeed, a fraction of the pool of oxaloacetate might be converted into alpha-ketoglutarate by aspartate transaminase to feed the TCA cycle. The rest might be converted into phosphoenolpyruvate (PEP) by PEP carboxykinase for gluconeogenesis because PEP carboxykinase was shown to carry higher fluxes in M1152 than in M145 (Figure 4C).

As recent studies have demonstrated a negative correlation and a competition for common precursors between secondary metabolite and triacylglycerol (TAG) biosynthesis in *S. lividans* and *S. coelicolor* (Craney et al., 2012; Esnault et al., 2017; Millan-Oropeza et al., 2017), one can speculate that the acetyl-CoA/malonyl-CoA units yielded by glycolysis for the biosynthesis of antibiotics in M145 are being used for enhanced growth and/or fatty acids and TAG biosynthesis in M1152. However, this is likely not the case, as M1152 has rather a reduced growth rate compared with M145, and fatty acid biosynthesis remains downregulated after the switch (Figure 5). Malonyl-CoA is predominantly shuttled toward fatty acid biosynthesis through malonyl-CoA-ACP transacylase, and this consumption seems to be well balanced by the amount of malonyl-CoA produced by acetyl-CoA carboxylase. It is noteworthy that the flux toward this acetyl-CoA/

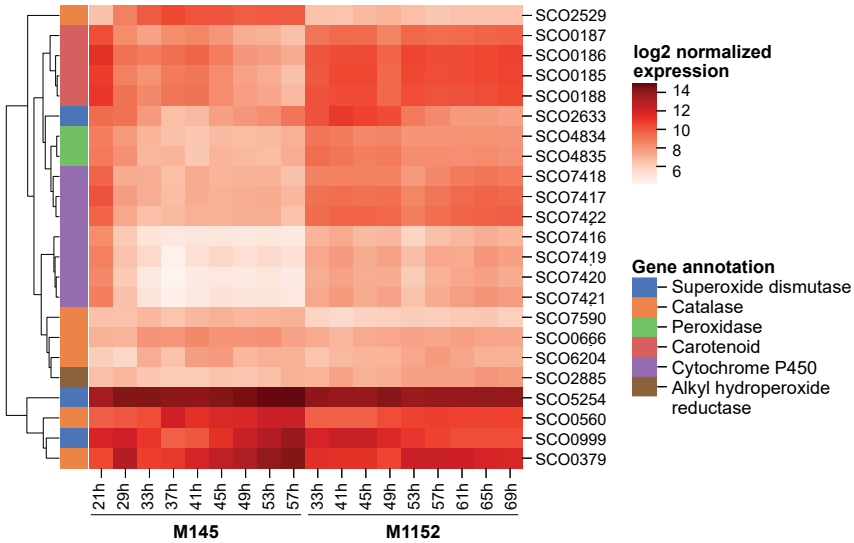

Figure 6. Heatmap Displaying Log-Transformed RNA-Seq Data of Genes Associated with Oxidative Stress

The genes included are related to oxidative stress and either present in Sco-GEM or within the 499 differentially expressed genes. These genes are categorized based on their functional annotation to distinguish differences and similarities between these functional groups. To further enhance visual interpretation the genes are ordered based on hierarchical clustering to align genes with similar expression profiles across M145 and M1152 next to each other.

malonyl-CoA drain is 3- to 6-fold larger than the total flux going into secondary metabolite biosynthesis, even after the metabolic switch. We thus propose that together with enhanced nitrogen availability, acetyl-CoA made available from the deletion of these BGCs is used to feed the TCA cycle to support the oxidative metabolism in M1152. This would generate oxidative stress whose toxic effects might be responsible for the growth delay of this strain.

Transcriptome Analysis Reveals Differential Expression of Global Regulators

Although the proteome data are an integral part of the EcSco-GEM models, RNA-seq data were used to both verify the trends and to gain further insights into the regulatory changes that are not captured by the metabolic models. As the proteomic data, the RNA-seq data showed large global differences between M1152 and M145, revealing 499 differentially expressed genes with a significance threshold of $p < 0.01$.

Unsupervised clustering of the significantly changed genes reveal differences in regulatory systems related to redox regulation, signaling, and secondary metabolism. The significantly changed genes were clustered into seven groups with K-means clustering, with clusters 1–3 containing genes that are upregulated in M1152 compared with M145, and clusters 4–7 vice versa (Figure S7A; Data S2). A Gene Ontology (Ashburner et al., 2000; The Gene Ontology Consortium, 2019) enrichment analysis of the seven clusters was conducted to identify upregulated processes in each of the two strains (Figure S8, cf. Figure S7A).

The enriched processes upregulated in M1152 point to increased oxidative stress (Figure S8): antioxidant and peroxidase activity (SCO2633 [sodF]; SCO4834-35) in addition to biosynthesis of carotenoid (SCO0185–SCO0188), a known antioxidant (Latifi et al., 2009; Stahl and Sies, 2003). The putative proteins within the cytochrome-P450 family (SCO7416–SCO7422) found in cluster 1 might be linked not only to increased oxidative stress (Zangar et al., 2004) but also to oxidation of precursors used for the synthesis of macrolides (Lamb et al., 2003). Indeed, by comparing the time series expression levels for genes related to oxidative stress we observe that the majority of genes related to oxidative stress are upregulated in M1152 (Figure 6). These changes correlate to a more active oxidative metabolism, TCA cycle, and oxidative stress as predicted by Ec-ScoGEM (Figure 4).

In cluster 2 we find *scbA* (SCO6266) and its downstream gene *scbC* (SCO6267), which stands out by being almost 6-fold upregulated in M1152. This high expression level is likely due to the deletion of *scbR2* (SCO6286), the last gene selected to be part of the *cpk* BGC (Bednarz et al., 2019). Besides regulation of

the *cpk* cluster, ScbR2 binds upstream of several global regulators of development and secondary metabolism, including AfsK, SigR, NagE2, AtrA, AdpA, and ArgR (Li et al., 2015). It also acts together with ScbR to regulate ScbA, which produces the γ-butyrolactone SCB1. However, when looking at the genes regulated by ScbR (Li et al., 2015), we only observe a clear difference in expression for genes regulated by AfsR (phosphorylated by AfsK) (Horinouchi, 2003; Lee et al., 2002), whereas this is not the case for genes regulated by ArgR, AdpA, or ScbR itself (Figures S5C-S5F).

Among the genes upregulated in M145, in cluster 4 we find genes related to the redox-regulated transcription factor SoxR (Naseer et al., 2014), and a similar pattern is observed for the entire SoxR regulon (Figure S7B). SoxR is known to react directly to the presence of actinorhodin (Dela Cruz et al., 2010; Shin et al., 2011), and indeed, in M145 this group of genes follows the production profile of actinorhodin, whereas their expression remains low in M1152 as Act is not produced. The benzoquinone Act, as electron acceptor, is thought to reduce respiration efficiency and thus energy charge, as well as to combat oxidative stress (Esnault et al., 2017). Consistently, the RNA-seq data revealed that the ATP-synthase gene cluster (SCO5366–SCO5374) was upregulated almost 2-fold in M1152 compared with M145, most prominently in the stationary phase during Act production (Figure S7C). This agrees with observations in the M1146 strain (Coze et al., 2013). Cluster 4 also contains the genes directly up- and downstream of the deleted actinorhodin BGC in M1152 (SCO5071–SCO5072, encoding 3-hydroxyacyl-CoA dehydrogenase, and SCO5091–SCO5092, encoding a two-component flavin-dependent monooxygenase system) (Valton et al., 2008). In clusters 5, 6, and 7 we find genes with reduced expression in M1152, and the enriched processes are related to cellular and iron ion homeostasis, development, signaling, and morphology. This corresponds to the delayed sporulation observed for M1152 (Gomez-Escribano and Bibb, 2011).

Elevated Expression of Ribosomal Proteins in M1152 after Phosphate Depletion

An increased transcription of genes encoding ribosomal proteins could be observed in M1152 after phosphate depletion (Figure S7D). The *rpoB* mutation of the RNA polymerase present in M1152 is thought to induce a conformational change mimicking the binding of guanosine tetraphosphate (ppGpp) to this enzyme (Hu et al., 2002). ppGpp is synthesized in response to nutritional stress and reduces the transcription of genes related to active growth, such as genes encoding ribosomal RNAs and ribosomal proteins (Burgos et al., 2017), whereas it upregulates those involved in development/differentiation and antibiotic production (Hesketh et al., 2007; Srivatsan and Wang, 2008). In consequence the upregulation of ribosomal proteins was unexpected in M1152, especially because the expression of the ppGpp regulon was not found to be significantly changed in M1152 (Figure S5G and S5H). We hypothesize that the ribosomal upregulation originates from the higher ATP content of M1152 compared with M145 post phosphate depletion, as high nucleoside triphosphate levels are known to have a positive impact on ribosome synthesis (Gaal et al., 1997). Such difference in ribosomal protein expression is mainly seen in the antibiotic production phase and correlated with production of Act in M145, which has a negative impact on the energetic state of the cell (Esnault et al., 2017).

Reduced Production of the Polyketide Germicidin in M1152

One could reasonably anticipate that the production of a secondary metabolite would increase if other drains competing for same precursor compounds were removed from the organism by gene deletion. However, the production rate of the polyketides germicidin A and B (Chemler et al., 2012), autologous to both M145 and M1152, were reduced in M1152 by 92% and 82% for germicidin A and B, respectively (Figure 7). This could be explained by the more active oxidative metabolism of M1152 compared with M145, as suggested by the enzyme-constrained model (Figure 4) and supported by the upregulation of genes associated with oxidative stress (Figure 6). In M1152 the pool of acetyl-CoA rather feeds the TCA cycle instead of being directed toward germicidin biosynthesis.

To further elucidate the cause of the reduced production in M1152, we also measured germicidin production in the intermediate strain M1146 (Figures 7 and S7E), which does not feature the *rpoB* mutation but is missing the four BGCs also deleted in M1152 (Gomez-Escribano and Bibb, 2011). The production rate of germicidin A and B in M1146 was found to be reduced by 27% and 25%, respectively, compared with M145. When compared with the strong reduction in germicidin production that can be assigned to the *rpoB* mutation in M1152, removal of only the four BGCs in M1146 has a moderate effect on germicidin production. This conforms with the minor contribution of the BGCs compared with fatty acid biosynthesis on the total consumption of malonyl-CoA (Figure 5). Nonetheless, it remains contradictory that the removal of polyketide precursor drains negatively impacts the production of other polyketides.

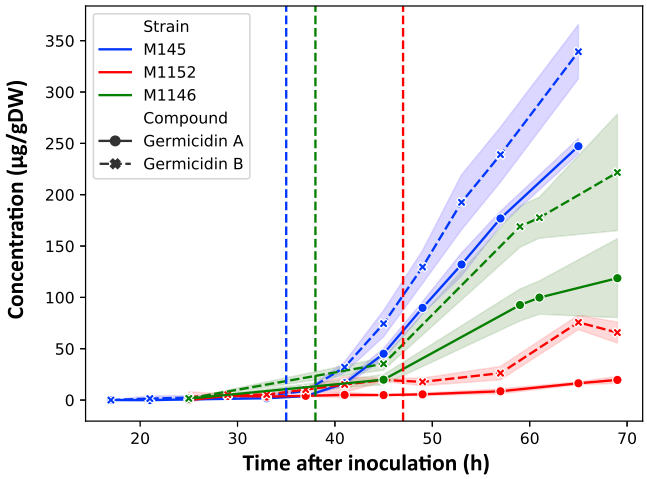

Figure 7. Concentrations of Germicidin A and B Produced by M145, M1146, and M1152

The concentrations are normalized by the biomass of each strain. The shaded regions display the uncertainty range (±1 standard deviation) based on three replicate cultivations. Note that the growth rate is different between the strains, displayed by the vertical lines representing phosphate depletion at 35, 38, and 47 h for M145, M1146, and M1152, respectively.

DISCUSSION

In this work, we carried out a multi-omics study to compare the metabolic changes of *Streptomyces coelicolor* M145 and the BGC deletion mutant M1152 during batch fermentation. The defined cultivation medium used in this work was chosen because it supports sufficient growth and a delayed, well-defined onset of secondary metabolism, necessary to study the metabolic switch (Wentzel et al., 2012a). We aimed at defining the metabolic features differing between the two strains, both during exponential growth and stationary phase after phosphate depletion.

To achieve this from a systems biology perspective, we combined time course sampled cultivation and transcriptome analysis with enzyme-constrained genome-scale models generated with proteome data. Such genome-scale models are extensively used to connect transcriptome and proteome data to metabolic fluxes. Leveraging metabolic simulations to contextualize transcriptional changes is mainly impacted by the quality of the computational model used. Here, two teams joined efforts to improve a consensus model of *S. coelicolor*, yielding a comprehensive model useful for the scientific community.

Genome-Scale Models Provide Hypothesis for Slow Growth of M1152

The reduced growth rate of M1152 is correlated with reduced glucose uptake and enhanced glutamate uptake compared with M145. This is expected to lead to a less active glycolysis but a more active TCA cycle, and thus, a more active oxidative metabolism in M1152 compared with M145. An active oxidative metabolism is known to generate oxidative stress, and indeed, the *in vivo* data, as well as the genome-scale model, predict an increased oxidative stress in M1152. The toxicity of oxidative stress might, at least in part, be responsible for the growth delay of M1152, whereas the *rpoB* mutation may add to this phenotype, because one of the functions of the ppGpp-associated RNA polymerase is to promote a growth arrest in conditions of nutritional stress.

Further Development May Improve M1152 as Host for Heterologous Expression

The strain M1152 has several advantages as a host for heterologous production of secondary metabolites. The deletion of the four major BGCs not only removes presumed competing drains for valuable precursors but also generates a clean background to ease the identification of novel products by mass spectrometry. M1152 has already been proved to be more efficient than M145 and M1146 in heterologous production of the nitrogen-containing antibiotics chloramphenicol and congocidine, as well as Act production from reintroduction of its BGC (Gomez-Escribano and Bibb, 2011). Strains M1146 and M1152 produce, respectively, 3- to 5-fold and 20- to 40-fold more chloramphenicol and congocidine from respective heterologous clusters than M145, a clear demonstration of the huge impact on production due to the *rpoB* mutation. Although this contrasts with our data

showing that M1152 has the lowest production of germicidin, it is relevant to note that chloramphenicol and congocidine are non-ribosomal peptide synthases relying on amino acids rather than malonyl-CoA as precursors. Although our data show reduced degradation of branched-chain amino acids and metabolism of alanine, aspartate, and glutamate as the clearest metabolic divergence upon phosphate depletion in M1152, as congocidine and chloramphenicol are based on aromatic amino acids the connection to increased production of these NRPs is not obvious. Another option is that the increased oxidative metabolism in M1152 provides more redox cofactors to drive the synthesis of these molecules. If competition for valuable precursors was rate limiting, the absence of the polyketides actinorhodin and coelimycin P1 should at least enhance the production of germicidin, all being dependent on malonyl-CoA. Moreover, differences in cultivation media further convolute cross-study comparisons: the aforementioned study use a complex growth medium, whereas we used a defined medium with glucose and glutamate, which has previously been optimized for studying the metabolic switch (Wentzel et al., 2012a).

Furthermore, (re-)introduction of a (secondary) copy of germicidin synthase gene *gcs* in strains M1152 and M1317—derived from M1152 by additional removal of three type III PKS genes including *gcs*—gave a 7.8- and 10.7-fold increase in germicidin production, respectively, compared with M1152 with only the native copy of *gcs* (Thanapipatsiri et al., 2015). Thus, the largest increase in production is not achieved by removal of competing precursor drains, but rather effected by the re-introduction of *gcs*, probably because expression of the inserted gene is not constrained by the same regulatory mechanism as the native gene.

Although earlier work has suggested a competition for common precursors between fatty acids and secondary metabolites biosynthesis (Craney et al., 2012), our results suggest that other approaches than deletion of competing precursor drains may be more efficient in the development of an optimized expression host, and it seems likely that different classes of BGCs may require different hosts for maximal production. Our comparative analysis of M145 and M1152 supports this development, not only as a systemic description connecting non-trivial associations between phenotypic, genetic, and metabolic differences but also by highlighting cellular processes that seem to be out of balance in M1152. These include upregulation of ribosomal genes, most likely an effect of the *rpoB* mutation, and increased oxidative metabolism and oxidative stress. As Act itself works as an electron acceptor one may hypothesize that its presence could relieve some of this stress. Another approach is to reintroduce *scbR2* to avoid influencing the related regulators of development and secondary metabolism.

Although *S. coelicolor* seems to have a complex and not fully elucidated regulatory system, several studies have shown that manipulation of regulatory genes can affect the production of secondary metabolites (Jones et al., 2011; Kim et al., 2003; Okamoto et al., 2003; Rodriguez et al., 2012). The complex regulation of secondary metabolite biosynthesis makes rational strain design difficult (Liu et al., 2013), but black-box approaches including random mutations and screening are still viable approaches for strain development (van den Berg et al., 2008; Crook and Alper, 2012). The Sco-GEM can aid this development by predicting the impact of these genetic alterations and to interpret "omics" data.

Limitations of the Study

We have performed a thorough comparison, of *S. coelicolor* M1145 and M1152, but to fully attribute changes in metabolism to the different genetic modifications as well as to unravel possible epistatic interactions we believe that a comprehensive analysis that also includes the intermediate strain M1146, and possibly also an M145 strain featuring only the *rpoB* mutation (Xu et al., 2002), will be necessary.

Resource Availability

Lead Contact

Further information and requests for resources and reagents should be directed to and will be fulfilled by the Lead Contact, Eduard J Kerkhoven (eduardk@chalmers.se).

Materials Availability

This study did not generate new unique reagents.

Data and Code Availability

The models and scripts generated during this study are available at GitHub (https://github.com/SysBioChalmers/Sco-GEM). Here, the latest version of the Sco-GEM is available in both YAML and

SBML level 3 Version 1. In addition, users can contribute to further model development by posting issues or suggest changes. The proteomics data are available from ProteomeXchange: PXD013178 via the PRIDE partner repository (Perez-Riverol et al., 2019). Normalized proteome data are also available in Data S3. The transcriptomics data are available from NCBI GEO: GSE132487 (M145) and GSE132488 (M1152). Normalized counts are also found in Data S4.

METHODS

All methods can be found in the accompanying Transparent Methods supplemental file.

SUPPLEMENTAL INFORMATION

Supplemental Information can be found online at https://doi.org/10.1016/j.isci.2020.101525.

ACKNOWLEDGMENTS

The authors would like to acknowledge Bogdan I. Florea of Leiden University, Leiden, Netherlands, for running and monitoring the proteome measurements and the bio-organic synthesis group at Leiden University for providing the opportunity to use their instrumentation. The authors would also like to acknowledge co-workers at SINTEF Industry, Trondheim, Norway: Ingemar Nærdal, Anna Lewin, and Kari Hjelen for running the batch fermentations and Anna Nordborg, Janne Beate Øiaas, and Tone Haugen for performing offline analyses and the germicidin analytics. The RNA-seq sequencing was carried out by c.ATG, Tübingen, Germany.

This study was conducted in the frame of ERA-net for Applied Systems Biology (ERA-SysAPP) project SYSTERACT and the project INBioPharm of the Center for Digital Live Norway (Research Council of Norway grant no. 248885), with additional support of SINTEF internal funding.

AUTHOR CONTRIBUTIONS

Conceptualization, E.J.K., E.A., A.W., S.S., A.S.-Y., and T.K.; Methodology and Software, E.J.K., S.S., A.S.-Y., and T.K; Validation and Formal Analysis, C.D., K.N., D.v.D., S.S., T.K., and E.J.K. Investigation, T.K., A.W., S.S., E.J.K.; Data Curation, S.S. and T.K.; Writing – Original Draft, S.S., T.K., D.V.D., C.D., and K.N.; Writing – Review & Editing, all authors; Visualization, S.S., E.K., C.D., and D.v.D.; Supervision, A.W., E.A., E.J.K., and G.P.v.W.; Project Administration, A.W.; Funding Acquisition: A.W., E.J.K., E.A., and G.P.v.W.

DECLARATION OF INTERESTS

The authors declare no competing interests.

Received: May 8, 2020
Revised: July 19, 2020
Accepted: August 31, 2020
Published: September 25, 2020

REFERENCES

Alam, M.T., Merlo, M.E., (stream), T.S.C., Hodgson, D.A., Wellington, E.M., Takano, E., and Breitling, R. (2010). Metabolic modeling and analysis of the metabolic switch in Streptomyces coelicolor. BMC Genomics *11*, 202.

Amara, A., Takano, E., and Breitling, R. (2018). Development and validation of an updated computational model of Streptomyces coelicolor primary and secondary metabolism. BMC Genomics *19*, 519.

Ashburner, M., Ball, C.A., Blake, J.A., Botstein, D., Butler, H., Cherry, J.M., Davis, A.P., Dolinski, K., Dwight, S.S., Eppig, J.T., et al. (2000). Gene ontology: tool for the unification of biology. The Gene Ontology Consortium. Nat. Genet. *25*, 25–29.

Aung, H.W., Henry, S.A., and Walker, L.P. (2013). Revising the Representation of fatty acid, glycerolipid, and glycerophospholipid metabolism in the consensus model of yeast metabolism. Ind. Biotechnol. *9*, 215–228.

Bar-Even, A., Flamholz, A., Noor, E., and Milo, R. (2012). Thermodynamic constraints shape the structure of carbon fixation pathways. Biochim. Biophys. Acta *1817*, 1646–1659.

Battke, F., Symons, S., and Nieselt, K. (2010). Mayday–integrative analytics for expression data. BMC Bioinformatics *11*, 121.

Bednarz, B., Kotowska, M., and Pawlik, K.J. (2019). Multi-level regulation of coelimycin synthesis in Streptomyces coelicolor A3(2). Appl. Microbiol. Biotechnol. *103*, 6423–6434.

Bentley, S.D., Chater, K.F., Cerdeño-Tárraga, A.-M.A.-M., Challis, G.L., Thomson, N.R., James, K.D., Harris, D.E., Quail, M.A., Kieser, H., Harper, D., et al. (2002). Complete genome sequence of the model actinomycete Streptomyces coelicolor A3(2). Nature *417*, 141–147.

van den Berg, M.A., Albang, R., Albermann, K., Badger, J.H., Daran, J.-M., Driessen, A.J.M., Garcia-Estrada, C., Fedorova, N.D., Harris, D.M., Heijne, W.H.M., et al. (2008). Genome sequencing and analysis of the filamentous fungus *Penicillium chrysogenum*. Nat. Biotechnol. *26*, 1161–1168.

Bordel, S., Agren, R., and Nielsen, J. (2010). Sampling the solution space in genome-scale metabolic networks reveals transcriptional regulation in key enzymes. PLOS Comput. Biol. *6*, e1000859.

Borodina, I., Krabben, P., and Nielsen, J. (2005). Genome-scale analysis of Streptomyces coelicolor A3(2) metabolism. Genome Res. *15*, 820–829.

Borodina, I., Siebring, J., Zhang, J., Smith, C.P., Keulen, G.van, Dijkhuizen, L., and Nielsen, J. (2008). Antibiotic overproduction in streptomyces coelicolor A3(2) mediated by phosphofructokinase deletion. J. Biol. Chem. *283*, 25186–25199.

Braesel, J., Tran, T.A., and Eustáquio, A.S. (2019). Heterologous expression of the diazaquinomycin biosynthetic gene cluster. J. Ind. Microbiol. Biotechnol. *46*, 1359–1364.

Burgos, H.L., O'Connor, K., Sanchez-Vazquez, P., and Gourse, R.L. (2017). Roles of transcriptional and translational control mechanisms in regulation of ribosomal protein synthesis in Escherichia coli. J. Bacteriol. *199*, e00407-17.

Bystrykh, L.V., Fernández-Moreno, M.A., Herrema, J.K., Malpartida, F., Hopwood, D.A., and Dijkhuizen, L. (1996). Production of actinorhodin-related "blue pigments" by Streptomyces coelicolor A3(2). J. Bacteriol. *178*, 2238–2244.

Castro, J.F., Razmilic, V., Gomez-Escribano, J.P., Andrews, B., Asenjo, J.A., and Bibb, M.J. (2015). Identification and heterologous expression of the chaxamycin biosynthesis gene cluster from streptomyces leeuwenhoekii. Appl. Environ. Microbiol. *81*, 5820–5831.

Chakrabarty, A.M. (1998). Nucleoside diphosphate kinase: role in bacterial growth, virulence, cell signalling and polysaccharide synthesis. Mol. Microbiol. *28*, 875–882.

Chandra, G., and Chater, K.F. (2014). Developmental biology of Streptomyces from the perspective of 100 actinobacterial genome sequences. FEMS Microbiol. Rev. *38*, 345–379.

Chemler, J.A., Buchholz, T.J., Geders, T.W., Akey, D.L., Rath, C.M., Chlipala, G.E., Smith, J.L., and Sherman, D.H. (2012). Biochemical and structural characterization of germicidin synthase: analysis of a type III polyketide synthase that employs acyl-ACP as a starter unit donor. J. Am. Chem. Soc. *134*, 7359–7366.

Coze, F., Gilard, F., Tcherkez, G., Virolle, M.-J., and Guyonvarch, A. (2013). Carbon-flux distribution within streptomyces coelicolor metabolism: a comparison between the actinorhodin-producing strain M145 and its non-producing derivative M1146. PLoS One *8*, e84151.

Craney, A., Ozimok, C., Pimentel-Elardo, S.M., Capretta, A., and Nodwell, J.R. (2012). Chemical perturbation of secondary metabolism demonstrates important links to primary metabolism. Chem. Biol. *19*, 1020–1027.

Crook, N., and Alper, H. (2012). Classical Strain Improvement. Engineering Complex Phenotypes in Industrial Strains (John Wiley & Sons, Inc.). http://Dx. Doi. Org/10.1002/9781118433034.Ch1.

Dela Cruz, R., Gao, Y., Penumetcha, S., Sheplock, R., Weng, K., and Chander, M. (2010). Expression of the Streptomyces coelicolor SoxR regulon is intimately linked with actinorhodin production. J. Bacteriol. *192*, 6428–6438.

Dobson, P.D., Smallbone, K., Jameson, D., Simeonidis, E., Lanthaler, K., Pir, P., Lu, C., Swainston, N., Dunn, W.B., Fisher, P., et al. (2010). Further developments towards a genome-scale metabolic model of yeast. BMC Syst. Biol. *4*, 145.

Esnault, C., Dulermo, T., Smirnov, A., Askora, A., David, M., Deniset-Besseau, A., Holland, I.-B., and Virolle, M.-J. (2017). Strong antibiotic production is correlated with highly active oxidative metabolism in Streptomyces coelicolor M145. Sci. Rep. *7*, 200.

Feist, A.M., Henry, C.S., Reed, J.L., Krummenacker, M., Joyce, A.R., Karp, P.D., Broadbelt, L.J., Hatzimanikatis, V., and Palsson, B.Ø. (2007). A genome-scale metabolic reconstruction for Escherichia coli K-12 MG1655 that accounts for 1260 ORFs and thermodynamic information. Mol. Syst. Biol. *3*, 121.

Fink, D., Weißschuh, N., Reuther, J., Wohlleben, W., and Engels, A. (2002). Two transcriptional regulators GlnR and GlnRII are involved in regulation of nitrogen metabolism in *Streptomyces coelicolor* A3(2). Mol. Microbiol. *46*, 331–347.

Flamholz, A., Noor, E., Bar-Even, A., and Milo, R. (2012). eQuilibrator—the biochemical thermodynamics calculator. Nucleic Acids Res. *40*, D770–D775.

Gaal, T., Bartlett, M.S., Ross, W., Turnbough, C.L., and Gourse, R.L. (1997). Transcription regulation by initiating NTP concentration: rRNA synthesis in bacteria. Science *278*, 2092–2097.

Gallo, G., Renzone, G., Alduina, R., Stegmann, E., Weber, T., Lantz, A.E., Thykaer, J., Sangiorgi, F., Scaloni, A., and Puglia, A.M. (2010). Differential proteomic analysis reveals novel links between primary metabolism and antibiotic production in Amycolatopsis balhimycina. Proteomics *10*, 1336–1358.

Getsin, I., Nalbandian, G.H., Yee, D.C., Vastermark, A., Paparoditis, P.C., Reddy, V.S., and Saier, M.H. (2013). Comparative genomics of transport proteins in developmental bacteria: myxococcus xanthus and Streptomyces coelicolor. BMC Microbiol. *13*, 279.

Gomez-Escribano, J.P., and Bibb, M.J. (2011). Engineering Streptomyces coelicolor for heterologous expression of secondary metabolite gene clusters. Microb. Biotechnol. *4*, 207–215.

Gomez-Escribano, J.P., and Bibb, M.J. (2014). Heterologous expression of natural product biosynthetic gene clusters in Streptomyces coelicolor: from genome mining to manipulation of biosynthetic pathways. J. Ind. Microbiol. Biotechnol. *41*, 425–431.

Gomez-Escribano, J.P., Song, L., Fox, D.J., Yeo, V., Bibb, M.J., and Challis, G.L. (2012). Structure and biosynthesis of the unusual polyketide alkaloid coelimycin P1, a metabolic product of the cpk gene cluster of Streptomyces coelicolor M145. Chem. Sci. *3*, 2716–2720.

Gu, C., Kim, G.B., Kim, W.J., Kim, H.U., and Lee, S.Y. (2019). Current status and applications of genome-scale metabolic models. Genome Biol. *20*, 121.

Hahn, J.-S., Oh, S.-Y., and Roe, J.-H. (2002). Role of OxyR as a peroxide-sensing positive regulator in streptomyces coelicolor A3(2). J. Bacteriol. *184*, 5214–5222.

Hastings, J., Owen, G., Dekker, A., Ennis, M., Kale, N., Muthukrishnan, V., Turner, S., Swainston, N., Mendes, P., and Steinbeck, C. (2016). ChEBI in 2016: improved services and an expanding collection of metabolites. Nucleic Acids Res. *44*, D1214–D1219.

Heavner, B.D., Smallbone, K., Barker, B., Mendes, P., and Walker, L.P. (2012). Yeast 5 – an expanded reconstruction of the Saccharomyces cerevisiae metabolic network. BMC Syst. Biol. *6*, 55.

Heavner, B.D., Smallbone, K., Price, N.D., and Walker, L.P. (2013). Version 6 of the consensus yeast metabolic network refines biochemical coverage and improves model performance. Database *2013*, bat059.

Hefzi, H., Ang, K.S., Hanscho, M., Bordbar, A., Ruckerbauer, D., Lakshmanan, M., Orellana, C.A., Baycin-Hizal, D., Huang, Y., Ley, D., et al. (2016). A consensus genome-scale reconstruction of Chinese hamster ovary cell metabolism. Cell Syst. *3*, 434–443.e8.

Herrgard, M.J., Swainston, N., Dobson, P., Dunn, W.B., Arga, K.Y., Arvas, M., Blüthgen, N., Borger, S., Costenoble, R., Heinemann, M., et al. (2008). A consensus yeast metabolic network reconstruction obtained from a community approach to systems biology. Nat. Biotechnol. *26*, 1155–1160.

Hesketh, A., Chen, W.J., Ryding, J., Chang, S., and Bibb, M. (2007). The global role of ppGpp synthesis in morphological differentiation and antibiotic production in Streptomyces coelicolor A3(2). Genome Biol. *8*, R161.

Horinouchi, S. (2003). AfsR as an integrator of signals that are sensed by multiple serine/threonine kinases in Streptomyces coelicolor A3(2). J. Ind. Microbiol. Biotechnol. *30*, 462–467.

Hu, H., Zhang, Q., and Ochi, K. (2002). Activation of antibiotic biosynthesis by specified mutations in the rpoB gene (encoding the RNA polymerase β subunit) of Streptomyces lividans. J. Bacteriol. *184*, 3984–3991.

Hutchings, M.I., Hoskisson, P.A., Chandra, G., and Buttner, M.J. (2004). Sensing and responding to diverse extracellular signals? Analysis of the sensor kinases and response regulators of Streptomyces coelicolor A3(2). Microbiology *150*, 2795–2806.

Jager, G., Battke, F., and Nieselt, K. (2011). Tiala — time series alignment analysis. In 2011 IEEE Symposium on Biological Data Visualization (BioVis), pp. 55–61.

Jones, G., Sol, R.D., Dudley, E., and Dyson, P. (2011). Forkhead-associated proteins genetically linked to the serine/threonine kinase PknB regulate carbon flux towards antibiotic

biosynthesis in Streptomyces coelicolor. Microb. Biotechnol. *4*, 263–274.

Jonsbu, E., Christensen, B., and Nielsen, J. (2001). Changes of in vivo fluxes through central metabolic pathways during the production of nystatin by Streptomyces noursei in batch culture. Appl. Microbiol. Biotechnol. *56*, 93–100.

Kanehisa, M. (2000). KEGG: kyoto encyclopedia of genes and genomes. Nucleic Acids Res. *28*, 27–30.

Kanehisa, M., Sato, Y., Furumichi, M., Morishima, K., and Tanabe, M. (2019). New approach for understanding genome variations in KEGG. Nucleic Acids Res. *47*, D590–D595.

Karp, P.D., Billington, R., Caspi, R., Fulcher, C.A., Latendresse, M., Kothari, A., Keseler, I.M., Krummenacker, M., Midford, P.E., Ong, Q., et al. (2019). The BioCyc collection of microbial genomes and metabolic pathways. Brief. Bioinform. *20*, 1085–1093.

Kepplinger, B., Morton-Laing, S., Seistrup, K.H., Marrs, E.C.L., Hopkins, A.P., Perry, J.D., Strahl, H., Hall, M.J., Errington, J., and Allenby, N.E.E. (2018). Mode of action and heterologous expression of the natural product antibiotic vancoresmycin. ACS Chem. Biol. *13*, 207–214.

Kieser, T., Bibb, M.J., Buttner, M.J., Chater, K.F., and Hopwood, D.A. (2000). Practical Streptomyces Genetics (Norwich, UK: John Innes Foundation).

Kim, D.-J., Huh, J.-H., Yang, Y.-Y., Kang, C.-M., Lee, I.-H., Hyun, C.-G., Hong, S.-K., and Suh, J.-W. (2003). Accumulation of S-Adenosyl-l-Methionine enhances production of actinorhodin but inhibits sporulation in streptomyces lividans TK23. J. Bacteriol. *185*, 592–600.

Kim, M.W., Sang Yi, J., Kim, J.-N.J.J.-N.N.J., Kim, J.-N.J.J.-N.N.J., Kim, M.W., and Kim, B.-G.G. (2014). Reconstruction of a high-quality metabolic model enables the identification of gene overexpression targets for enhanced antibiotic production in streptomyces coelicolor A3(2). Biotechnol. J. *9*, 1185–1194.

King, Z.A., Dräger, A., Ebrahim, A., Sonnenschein, N., Lewis, N.E., and Palsson, B.O. (2015). Escher: a web application for building, sharing, and embedding data-Rich visualizations of biological pathways. PLOS Comput. Biol. *11*, e1004321.

King, Z.A., Lu, J., Dräger, A., Miller, P., Federowicz, S., Lerman, J.A., Ebrahim, A., Palsson, B.O., and Lewis, N.E. (2016). BiGG Models: a platform for integrating, standardizing and sharing genome-scale models. Nucleic Acids Res. *44*, D515–D522.

Kumelj, T., Sulheim, S., Wentzel, A., and Almaas, E. (2019). Predicting strain engineering strategies using iKS1317: a genome-scale metabolic model of *Streptomyces coelicolor*. Biotechnol. J. *14*, 1800180.

Lamb, D.C., Ikeda, H., Nelson, D.R., Ishikawa, J., Skaug, T., Jackson, C., Omura, S., Waterman, M.R., and Kelly, S.L. (2003). Cytochrome P450 complement (CYPome) of the avermectin-producer Streptomyces avermitilis and comparison to that of Streptomyces coelicolor A3(2). Biochem. Biophys. Res. Commun. *307*, 610–619.

Latifi, A., Ruiz, M., and Zhang, C.-C. (2009). Oxidative stress in cyanobacteria. FEMS Microbiol. Rev. *33*, 258–278.

Lee, P.-C., Umeyama, T., and Horinouchi, S. (2002). afsS is a target of AfsR, a transcriptional factor with ATPase activity that globally controls secondary metabolism in Streptomyces coelicolor A3(2). Mol. Microbiol. *43*, 1413–1430.

Li, T., Du, Y., Cui, Q., Zhang, J., Zhu, W., Hong, K., and Li, W. (2013). Cloning, characterization and heterologous expression of the indolocarbazole biosynthetic gene cluster from marine-derived streptomyces sanyensis FMA. Mar. Drugs *11*, 466–488.

Li, X., Wang, J., Li, S., Ji, J., Wang, W., and Yang, K. (2015). ScbR- and ScbR2-mediated signal transduction networks coordinate complex physiological responses in *Streptomyces coelicolor*. Sci. Rep. *5*, 14831.

Li, L., Jiang, W., and Lu, Y. (2017). A novel two-component system, GluR-GluK, involved in glutamate sensing and uptake in streptomyces coelicolor. J. Bacteriol. *199*, e00097-17.

Liao, Y., Smyth, G.K., and Shi, W. (2014). featureCounts: an efficient general purpose program for assigning sequence reads to genomic features. Bioinformatics *30*, 923–930.

Licona-Cassani, C., Marcellin, E., Quek, L.-E., Jacob, S., and Nielsen, L.K. (2012). Reconstruction of the Saccharopolyspora erythraea genome-scale model and its use for enhancing erythromycin production. Antonie van Leeuwenhoek *102*, 493–502.

Lieven, C., Beber, M.E., Olivier, B.G., Bergmann, F.T., Ataman, M., Babaei, P., Bartell, J.A., Blank, L.M., Chauhan, S., Correia, K., et al. (2020). MEMOTE for standardized genome-scale metabolic model testing. Nat. Biotechnol. *38*, 272–276.

Liu, G., Chater, K.F., Chandra, G., Niu, G., and Tan, H. (2013). Molecular regulation of antibiotic biosynthesis in streptomyces. Microbiol. Mol. Biol. Rev. *77*, 112–143.

Love, M.I., Huber, W., and Anders, S. (2014). Moderated estimation of fold change and dispersion for RNA-seq data with DESeq2. Genome Biol. *15*, 550.

Lu, H., Li, F., Sánchez, B.J., Zhu, Z., Li, G., Domenzain, I., Marcišauskas, S., Anton, P.M., Lappa, D., Lieven, C., et al. (2019). A consensus *S. cerevisiae* metabolic model Yeast8 and its ecosystem for comprehensively probing cellular metabolism. Nat. Commun. *10*, 1–13.

Martin, J.F. (2004). Phosphate control of the biosynthesis of antibiotics and other secondary metabolites is mediated by the PhoR-PhoP system: an unfinished story. J. Bacteriol. *186*, 5197–5201.

Martín, J.F., Santos-Beneit, F., Rodríguez-García, A., Sola-Landa, A., Smith, M.C.M., Ellingsen, T.E., Nieselt, K., Burroughs, N.J., and Wellington, E.M.H. (2012). Transcriptomic studies of phosphate control of primary and secondary metabolism in Streptomyces coelicolor. Appl. Microbiol. Biotechnol. *95*, 61–75.

Martin, J.F., Rodríguez-García, A., and Liras, P. (2017). The master regulator PhoP coordinates phosphate and nitrogen metabolism, respiration, cell differentiation and antibiotic biosynthesis: comparison in *Streptomyces coelicolor* and *Streptomyces avermitilis*. J. Antibiot. *70*, 534–541.

Martin-Martin, S., Rodríguez-García, A., Santos-Beneit, F., Franco-Domínguez, E., Sola-Landa, A., and Martín, J.F. (2018). Self-control of the PHO regulon: the PhoP-dependent protein PhoU controls negatively expression of genes of PHO regulon in *Streptomyces coelicolor*. J. Antibiot. *71*, 113–122.

Mi, H., Muruganujan, A., Ebert, D., Huang, X., and Thomas, P.D. (2019). PANTHER version 14: more genomes, a new PANTHER GO-slim and improvements in enrichment analysis tools. Nucleic Acids Res. *47*, D419–D426.

Millan-Oropeza, A., Henry, C., Blein-Nicolas, M., Aubert-Frambourg, A., Moussa, F., Bleton, J., and Virolle, M.-J. (2017). Quantitative proteomics analysis confirmed oxidative metabolism predominates in streptomyces coelicolor versus glycolytic metabolism in streptomyces lividans. J. Proteome Res. *16*, 2597–2613.

Mohite, O.S., Weber, T., Kim, H.U., and Lee, S.Y. (2019). Genome-scale metabolic reconstruction of actinomycetes for antibiotics production. Biotechnol. J. *14*, 1800377.

Moretti, S., Martin, O., Van Du Tran, T., Bridge, A., Morgat, A., and Pagni, M. (2016). MetaNetX/MNXref – reconciliation of metabolites and biochemical reactions to bring together genome-scale metabolic networks. Nucleic Acids Res. *44*, D523–D526.

Naseer, N., Shapiro, J.A., and Chander, M. (2014). RNA-Seq analysis reveals a six-gene SoxR regulon in Streptomyces coelicolor. PLoS One *9*, e106181.

Nepal, K.K., and Wang, G. (2019). Streptomycetes: surrogate hosts for the genetic manipulation of biosynthetic gene clusters and production of natural products. Biotechnol. Adv. *37*, 1–20.

Nieselt, K., Battke, F., Herbig, A., Bruheim, P., Wentzel, A., Jakobsen, Ø.M., Sletta, H., Alam, M.T., Merlo, M.E., Moore, J., et al. (2010). The dynamic architecture of the metabolic switch in Streptomyces coelicolor. BMC Genomics *11*, 10.

Nothaft, H., Rigali, S., Boomsma, B., Swiatek, M., McDowall, K.J., van Wezel, G.P., and Titgemeyer, F. (2010). The permease gene nagE2 is the key to N-acetylglucosamine sensing and utilization in Streptomyces coelicolor and is subject to multi-level control. Mol. Microbiol. *75*, 1133–1144.

Okamoto, S., Lezhava, A., Hosaka, T., Okamoto-Hosoya, Y., and Ochi, K. (2003). Enhanced expression of S-adenosylmethionine synthetase causes overproduction of actinorhodin in streptomyces coelicolor A3(2). J. Bacteriol. *185*, 601–609.

Orth, J.D., Thiele, I., and Palsson, B.Ø.O. (2010). What is flux balance analysis? Nat. Biotech. *28*, 245–248.

Perez-Riverol, Y., Csordas, A., Bai, J., Bernal-Llinares, M., Hewapathirana, S., Kundu, D.J., Inuganti, A., Griss, J., Mayer, G., Eisenacher, M.,

et al. (2019). The PRIDE database and related tools and resources in 2019: improving support for quantification data. Nucleic Acids Res. *47*, D442–D450.

Rigali, S., Titgemeyer, F., Barends, S., Mulder, S., Thomae, A.W., Hopwood, D.A., and van Wezel, G.P. (2008). Feast or famine: the global regulator DasR links nutrient stress to antibiotic production by Streptomyces. EMBO Rep. *9*, 670–675.

Robinson, J.L., and Nielsen, J. (2016). Integrative analysis of human omics data using biomolecular networks. Mol. Biosyst. *12*, 2953–2964.

Rodriguez, E., Navone, L., Casati, P., and Gramajo, H. (2012). Impact of malic enzymes on antibiotic and triacylglycerol production in streptomyces coelicolor. Appl. Environ. Microbiol. *78*, 4571–4579.

Rutledge, P.J., and Challis, G.L. (2015). Discovery of microbial natural products by activation of silent biosynthetic gene clusters. Nat. Rev. Microbiol. *13*, 509–523.

Sanchez, B.J., Zhang, C., Nilsson, A., Lahtvee, P.-J., Kerkhoven, E.J., and Nielsen, J. (2017). Improving the phenotype predictions of a yeast genome-scale metabolic model by incorporating enzymatic constraints. Mol. Syst. Biol. *13*, 935.

Shin, J.-H., Singh, A.K., Cheon, D.-J., and Roe, J.-H. (2011). Activation of the SoxR regulon in Streptomyces coelicolor by the extracellular form of the pigmented antibiotic actinorhodin. J. Bacteriol. *193*, 75–81.

Smirnov, A., Esnault, C., Prigent, M., Holland, I.B., and Virolle, M.-J. (2015). Phosphate homeostasis in conditions of phosphate proficiency and limitation in the wild type and the phoP mutant of streptomyces lividans. PLoS One *10*, e0126221.

Sola-Landa, A., Moura, R.S., and Martín, J.F. (2003). The two-component PhoR-PhoP system controls both primary metabolism and secondary metabolite biosynthesis in Streptomyces lividans. Proc. Natl. Acad. Sci. U S A *100*, 6133–6138.

Sola-Landa, A., Rodríguez-García, A., Franco-Domínguez, E., and Martín, J.F. (2005). Binding of PhoP to promoters of phosphate-regulated genes in Streptomyces coelicolor: identification of PHO boxes. Mol. Microbiol. *56*, 1373–1385.

Srivatsan, A., and Wang, J.D. (2008). Control of bacterial transcription, translation and replication by (p)ppGpp. Curr. Opin. Microbiol. *11*, 100–105.

Stahl, W., and Sies, H. (2003). Antioxidant activity of carotenoids. Mol. Aspects Med. *24*, 345–351.

Stirrett, K., Denoya, C., and Westpheling, J. (2009). Branched-chain amino acid catabolism provides precursors for the Type II polyketide antibiotic, actinorhodin, via pathways that are nutrient dependent. J. Ind. Microbiol. Biotechnol. *36*, 129–137.

Thanapipatsiri, A., Claesen, J., Gomez-Escribano, J.-P., Bibb, M., and Thamchaipenet, A. (2015). A Streptomyces coelicolor host for the heterologous expression of Type III polyketide synthase genes. Microb. Cell Fact. *14*, 145.

The Gene Ontology Consortium (2019). The gene ontology resource: 20 years and still GOing strong. Nucleic Acids Res. *47*, D330–D338.

The UniProt Consortium (2019). UniProt: a worldwide hub of protein knowledge. Nucleic Acids Res. *47*, D506–D515.

Thiele, I., and Palsson, B.Ø. (2010). A protocol for generating a high-quality genome-scale metabolic reconstruction. Nat. Protoc. *5*, 93–121.

Thiele, I., Swainston, N., Fleming, R.M.T., Hoppe, A., Sahoo, S., Aurich, M.K., Haraldsdottir, H., Mo, M.L., Rolfsson, O., Stobbe, M.D., et al. (2013). A community-driven global reconstruction of human metabolism. Nat. Biotechnol. *31*, 419–425.

Thomas, L., Hodgson, D.A., Wentzel, A., Nieselt, K., Ellingsen, T.E., Moore, J., Morrissey, E.R., Legaie, R., STREAM Consortium, T.S., Wohlleben, W., et al. (2012). Metabolic switches and adaptations deduced from the proteomes of Streptomyces coelicolor wild type and phoP mutant grown in batch culture. Mol. Cell. Proteomics *11*, M111.013797.

Toro, L., Pinilla, L., Avignone-Rossa, C., and Ríos-Estepa, R. (2018). An enhanced genome-scale metabolic reconstruction of Streptomyces clavuligerus identifies novel strain improvement strategies. Bioproc. Biosyst. Eng. *41*, 657–669.

Valton, J., Mathevon, C., Fontecave, M., Nivière, V., and Ballou, D.P. (2008). Mechanism and regulation of the two-component FMN-dependent monooxygenase ActVA-ActVB from streptomyces coelicolor. J. Biol. Chem. *283*, 10287–10296.

Valverde, J.R., Gullón, S., and Mellado, R.P. (2018). Modelling the metabolism of protein secretion through the Tat route in Streptomyces lividans. BMC Microbiol. *18*, 59.

Wang, H., Marcišauskas, S., Sánchez, B.J., Domenzain, I., Hermansson, D., Agren, R., Nielsen, J., and Kerkhoven, E.J. (2018). Raven 2.0: a versatile toolbox for metabolic network reconstruction and a case study on Streptomyces coelicolor. PLOS Comput. Biol. *14*, e1006541.

Wentzel, A., Bruheim, P., Øverby, A., Jakobsen, Ø.M., Sletta, H., Omara, W.A.M., Hodgson, D.A., and Ellingsen, T.E. (2012a). Optimized submerged batch fermentation strategy for systems scale studies of metabolic switching in Streptomyces coelicolor A3(2). BMC Syst. Biol. *6*, 59.

Wentzel, A., Sletta, H., Consortium, S., Ellingsen, T.E., and Bruheim, P. (2012b). Intracellular metabolite pool changes in response to nutrient depletion induced metabolic switching in streptomyces coelicolor. Metabolites *2*, 178–194.

Xu, J., Tozawa, Y., Lai, C., Hayashi, H., and Ochi, K. (2002). A rifampicin resistance mutation in the rpoB gene confers ppGpp-independent antibiotic production in Streptomyces coelicolor A3(2). Mol. Gen. Genomics *268*, 179–189.

Yin, J., Hoffmann, M., Bian, X., Tu, Q., Yan, F., Xia, L., Ding, X., Francis Stewart, A., Müller, R., Fu, J., et al. (2015). Direct cloning and heterologous expression of the salinomycin biosynthetic gene cluster from Streptomyces albus DSM41398 in Streptomyces coelicolor A3(2). Sci. Rep. *5*, 15081.

Yoshida, M., Muneyuki, E., and Hisabori, T. (2001). ATP synthase — a marvellous rotary engine of the cell. Nat. Rev. Mol. Cell Biol. *2*, 669–677.

Zangar, R.C., Davydov, D.R., and Verma, S. (2004). Mechanisms that regulate production of reactive oxygen species by cytochrome P450. Toxicol. Appl. Pharmacol. *199*, 316–331.

iScience, Volume *23*

Supplemental Information

Enzyme-Constrained Models and Omics Analysis of *Streptomyces coelicolor* Reveal Metabolic Changes that Enhance Heterologous Production

Snorre Sulheim, Tjaša Kumelj, Dino van Dissel, Ali Salehzadeh-Yazdi, Chao Du, Gilles P. van Wezel, Kay Nieselt, Eivind Almaas, Alexander Wentzel, and Eduard J. Kerkhoven

Supplemental figures

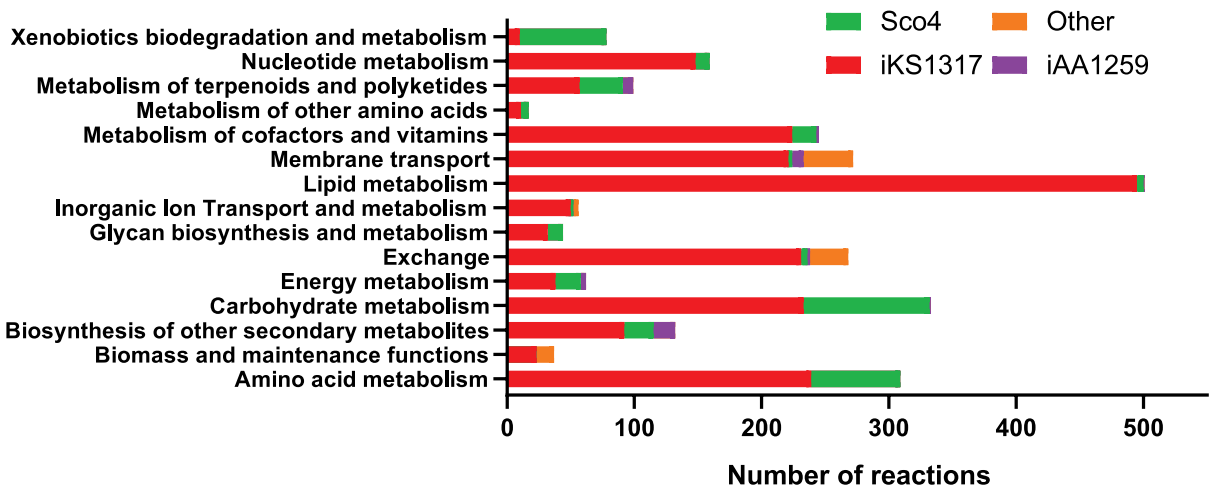

Figure S1: Reaction subsystems and origin, related to Figure 1A. The number of reactions in Sco-GEM in each of the 15 subsystems, and from which model they originate from. The other reactions (orange) are added during reconstruction of Sco-GEM.

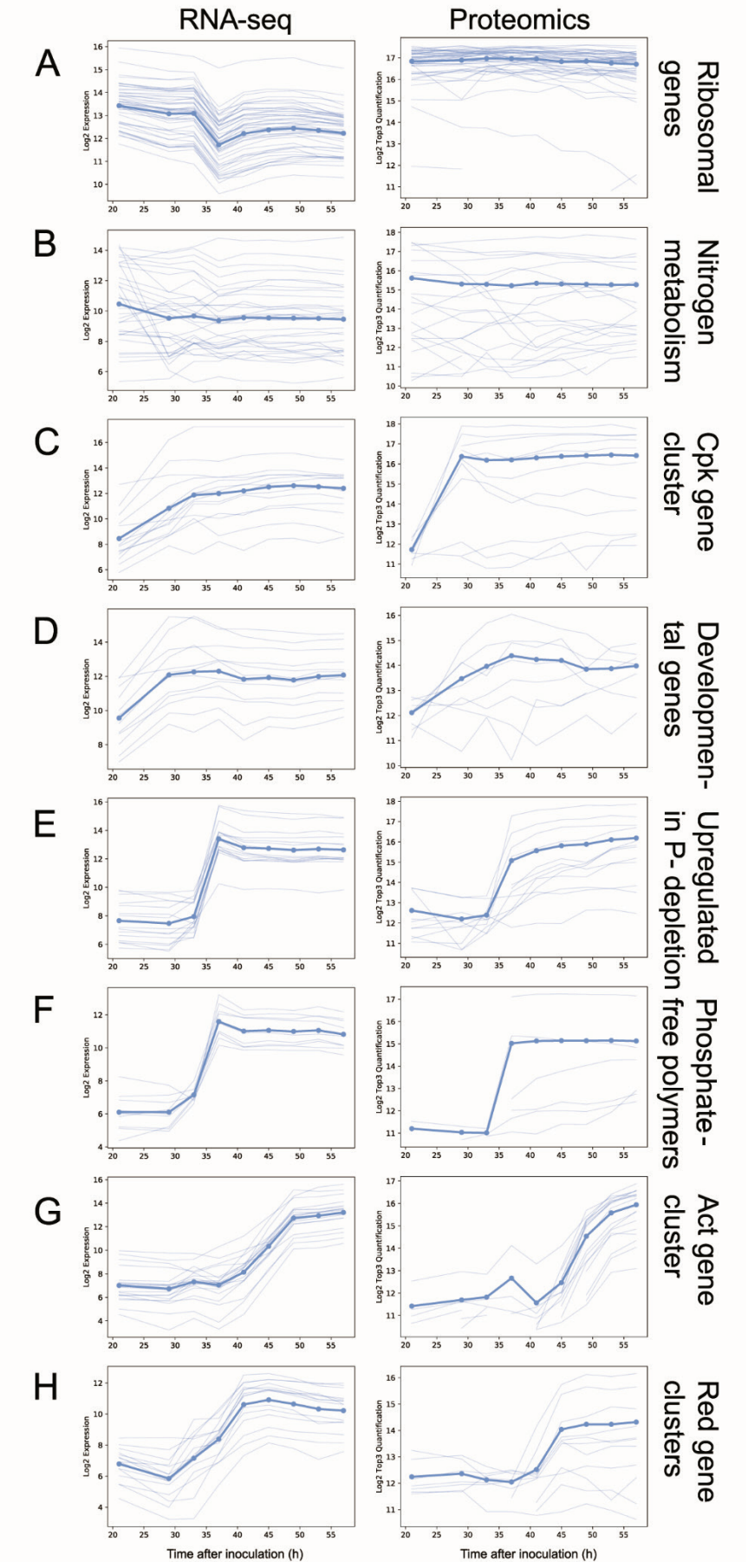

Figure S2: Gene clusters associated with metabolic switch, related to Figure 2C. RNA-seq (left column) and proteomics (right column) from M145 of the 8 gene clusters associated with the metabolic switch as previously identified (Nieselt et al., 2010). The 8 clusters are: A) genes related to ribosomal proteins; B) genes related to nitrogen metabolism; C) Cpk gene cluster; D) genes related to development; E) genes upregulated in response to phosphate depletion; F) genes involved in synthesis of phosphate-free polymers; G) Act gene cluster; H) Red gene cluster.

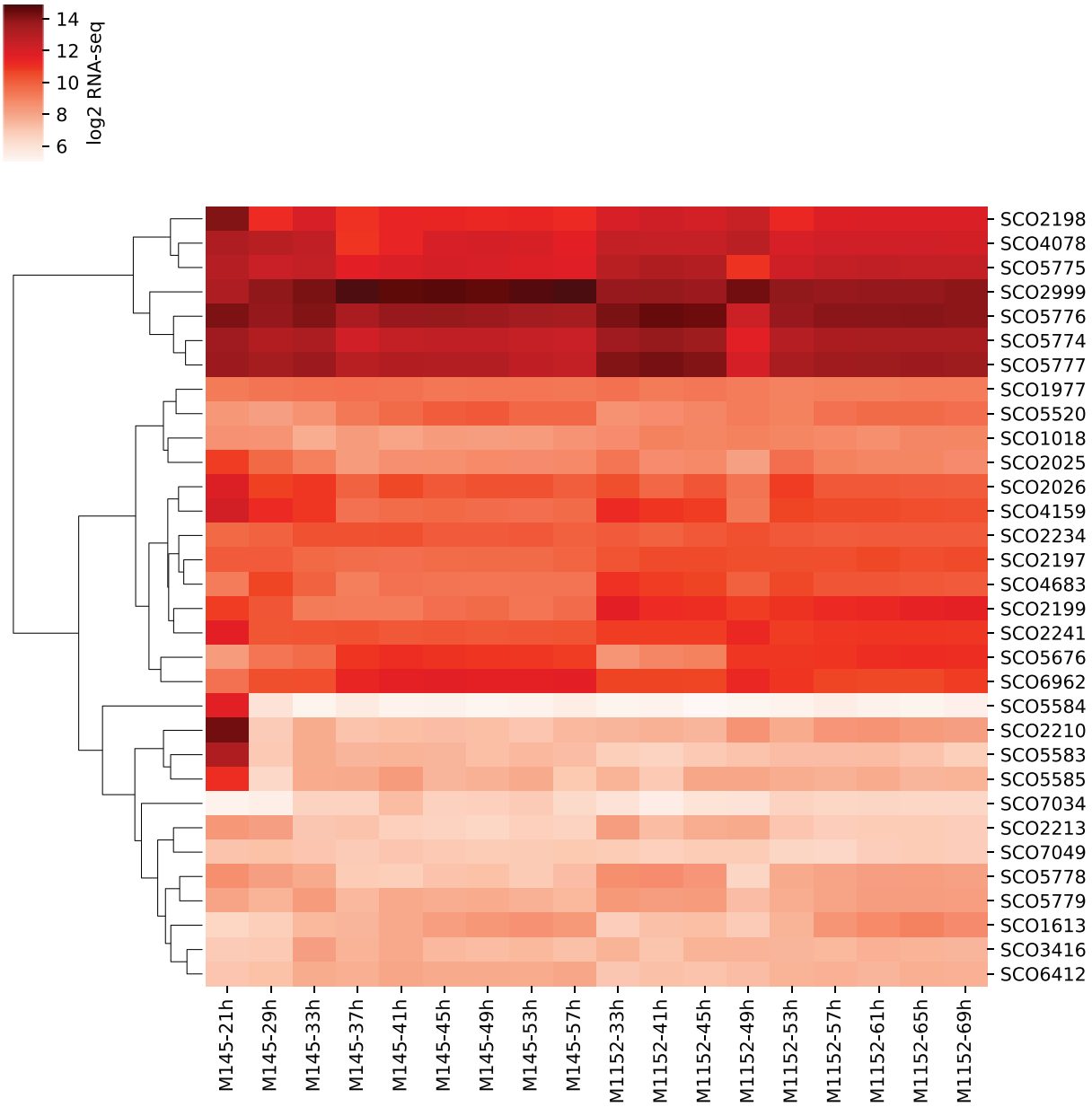

Figure S3: Log-transformed expression levels of genes associated with nitrogen metabolism, related to Figure 2D. The order of the genes is determined by hierarchical clustering to align genes with similar expression profiles next to each other. From the log2-transformed RNA-seq data we observe that glutamate import (SCO5774-5777), the glutamate sensing system *gluR-gluK* (SCO5778 and SCO57779), *glnR* (SCO4159) and *glnA* (SCO2198) are downregulated subsequent to phosphate depletion. The phosphate depletion occurs between the third and fourth time point, i.e. at 35 and 47 hours for M145 and M1152, respectively. We also observe that the first time point in M145 is very different from all other samples.

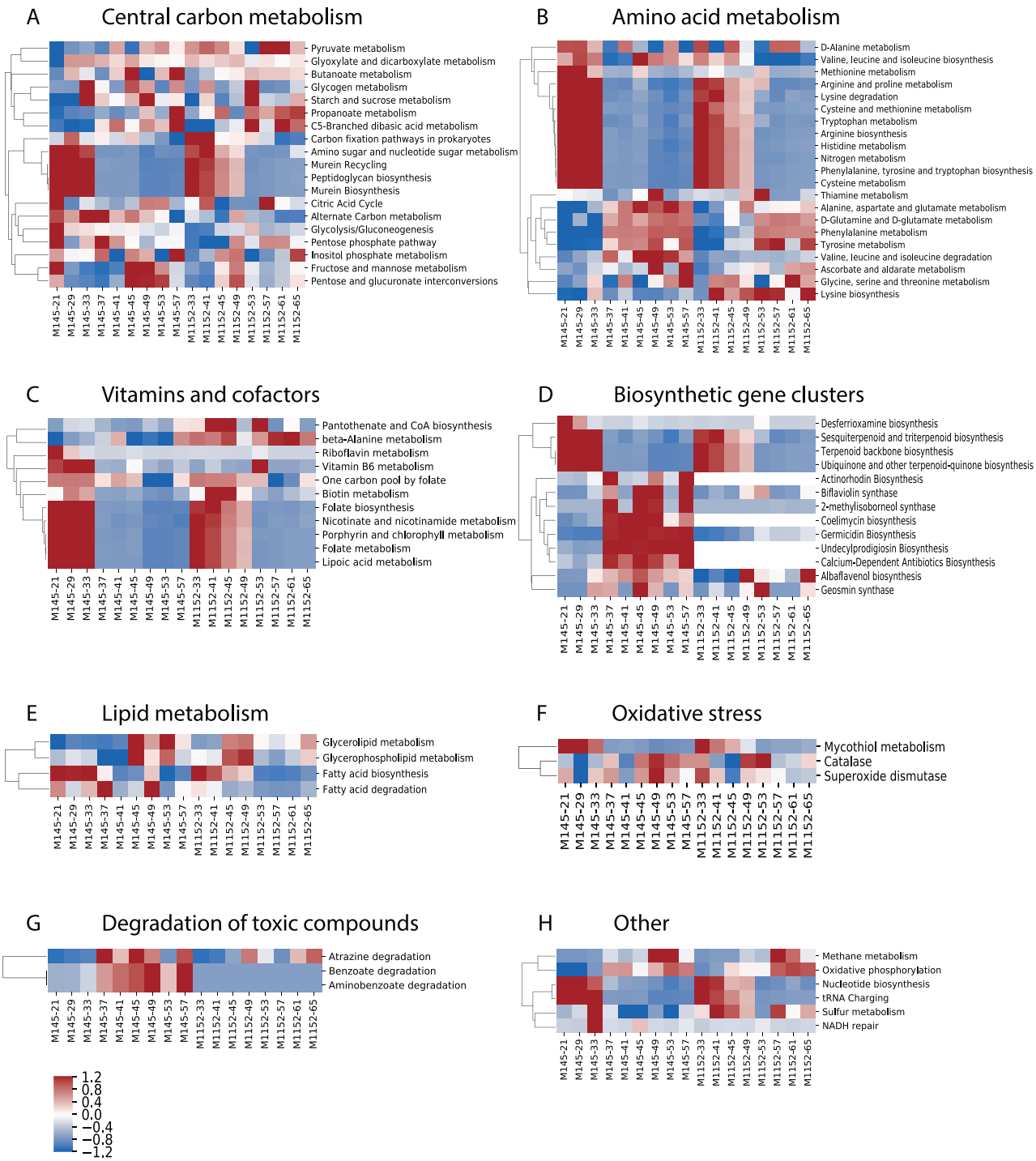

Figure S4: Clustered heatmaps of Z-score based on CO_2-normalized sum of fluxes of all pathways standardized within each pathway and separated into different subsystems / parts of the metabolism. Related to Figure 2D. A) Central carbon metabolism. B) Amino acid metabolism. C) Metabolism of vitamins and cofactors. D) Pathways of Biosynthetic gene clusters. E) Lipid metabolism. F) Oxidative stress. G) Degradation of toxic compounds. H) All other pathways. For all panels only pathway with a minimum flux of 1e-8 mmol $(g\ DW)^{-1}\ h^{-1}$ were included.

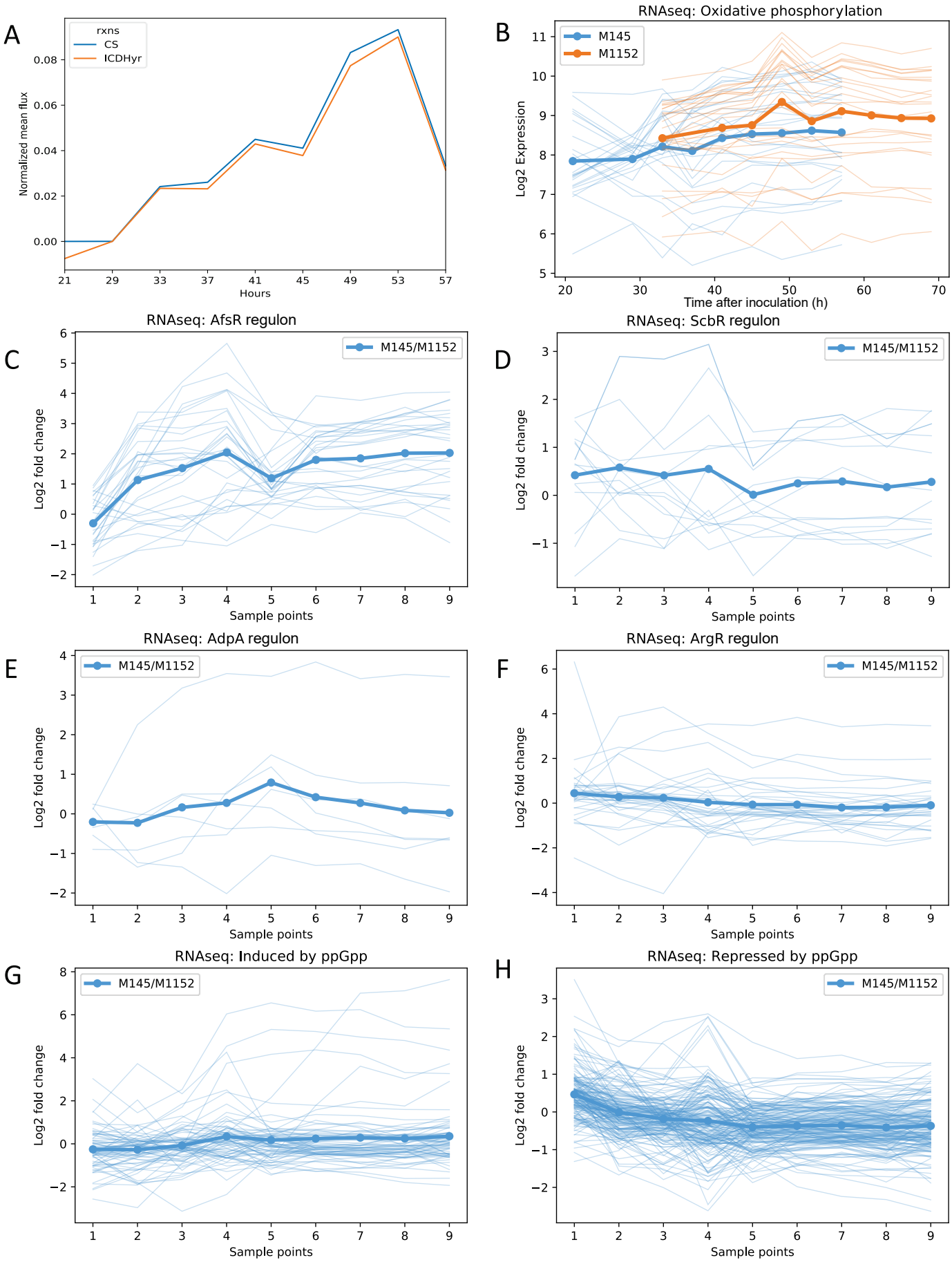
A
rxns
CS
ICDHyr
Normalized mean flux
Hours
B
RNAseq: Oxidative phosphorylation
M145
M1152
Log2 Expression
Time after inoculation (h)
C
RNAseq: AfsR regulon
M145/M1152
Log2 fold change
Sample points
D
RNAseq: ScbR regulon
M145/M1152
Log2 fold change
Sample points
E
RNAseq: AdpA regulon
M145/M1152
Log2 fold change
Sample points
F
RNAseq: ArgR regulon
M145/M1152
Log2 fold change
Sample points
G
RNAseq: Induced by ppGpp
M145/M1152
Log2 fold change
Sample points
H
RNAseq: Repressed by ppGpp
M145/M1152
Log2 fold change
Sample points

Figure S5: **RNA-seq, proteome and flux prediction of specific gene clusters and reactions. Related to Figure 2, 3 and S7.** A) This panel display increasing CO2-normalized flux through citrate synthase (CS) and isocitrate dehydrogenase (ICDHyr) at later time points in M145 as predicted by EcSco-GEM. These two reactions are both part of the TCA cycle, converting acetyl-CoA to citrate (citrate synthase) and isocitrate to alpha-ketogluterate (isocitrate dehydrogenase). B) Log2 normalized expression data of genes involved in oxidative phosphorylation for M145 (blue) and M1152 (orange). The average expression level is higher in M1152 than in M145 but increasing at later time points for both strains. The expression profiles are only partially overlapping along the x-axis (hours after inoculation) because of the reduced growth and therefore delayed cultivation of M1152. C-H) Comparison of log2 normalized expression data as calculated with (log2 M145)-log2(M1152), where positive values indicate upregulation in M145 relative to M1152, and vice versa for negative values. C) Increased expression of genes of the AfsR regulon in M145, while no significant difference in expression is observed for (D) ScbR regulon; (E) AdpA regulon; (F) ArgR regulon; (G) genes induced by ppGpp; and (H) genes repressed by ppGpp.

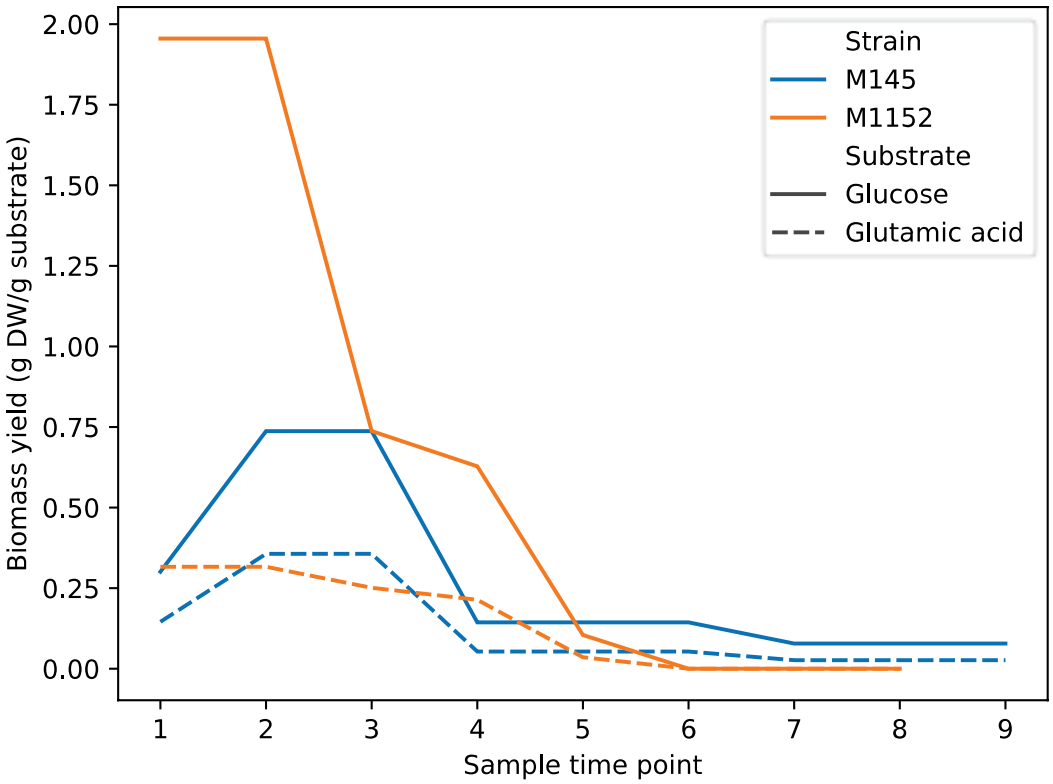

Figure S6: **Biomass yield on glucose and glutamic acid, related to Figure 4.** M1152 (orange) has a higher growth yield on glucose than M145 (blue). The yield on glutamic acid (dashed line) is similar between the two strains.

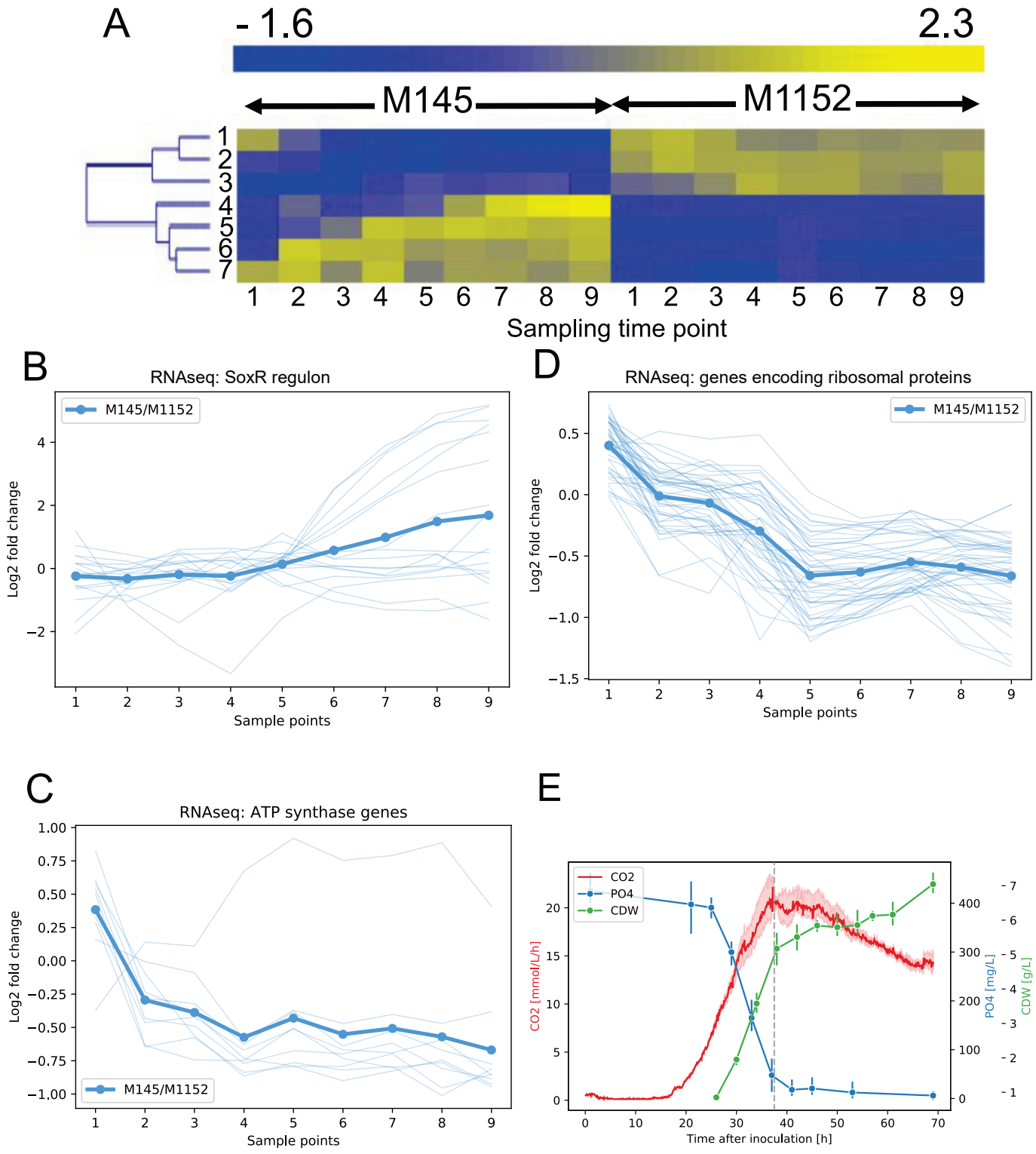

Figure S7: Analysis of transcriptome data of genes, related to Figure 2, 3, S5 and S8, and cultivation data of M1146, related to Figure 7. A) The heatmap display the mean standardized log2 expression levels for the 7 clusters of differentially expressed genes as determined by unsupervised clustering (k-means). Cluster 1-3 are upregulated in M1152, while the last four

(cluster 4-7) are upregulated from the beginning or at later time points in M145. B-D) Comparison of log2 normalized expression data as calculated with (log2 M145)-log2(M1152), where positive values indicate upregulation in M145 relative to M1152, and vice versa for negative values. B) Genes in the SoxR regulon are reducing expression in M1152 at later time points. C) Almost all genes in the ATP-synthase cluster are up-regulated in M1152 after the first time point. D) The transcription of ribosomal protein genes after the metabolic switch is increased in M1152 compared to M145. E) Batch cultivation data of *S. coelicolor* M1146, showing volume corrected respiration (CO_2), phosphate (PO_4) and cell dry weight (CDW). Error bars are standard deviations of three biological replicates.

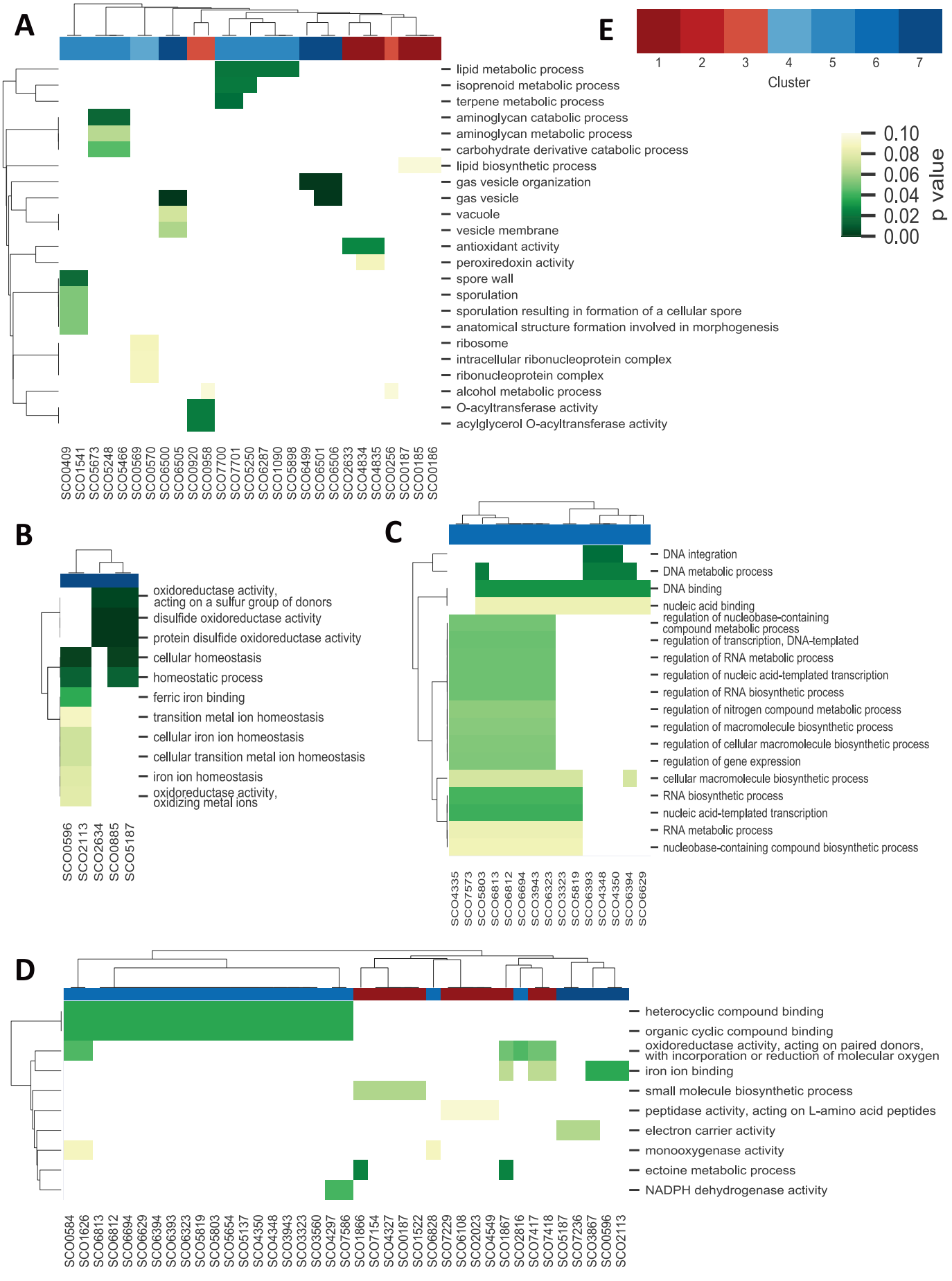
A
lipid metabolic process
isoprenoid metabolic process
terpene metabolic process
aminoglycan catabolic process
aminoglycan metabolic process
carbohydrate derivative catabolic process
lipid biosynthetic process
gas vesicle organization
gas vesicle
vacuole
vesicle membrane
antioxidant activity
peroxiredoxin activity
spore wall
sporulation
sporulation resulting in formation of a cellular spore
anatomical structure formation involved in morphogenesis
ribosome
intracellular ribonucleoprotein complex
ribonucleoprotein complex
alcohol metabolic process
O-acyltransferase activity
acylglycerol O-acyltransferase activity
SCO0409 SCO1541 SCO5673 SCO5248 SCO5466 SCO0569 SCO0570 SCO6500 SCO6505 SCO0920 SCO0958 SCO7700 SCO7701 SCO5250 SCO6287 SCO1090 SCO5898 SCO6499 SCO6501 SCO6506 SCO2633 SCO4834 SCO4835 SCO0256 SCO0187 SCO0185 SCO0186
E
1 2 3 4 5 6 7
Cluster
0.10 0.08 0.06 0.04 0.02 0.00
p value
B
oxidoreductase activity, acting on a sulfur group of donors
disulfide oxidoreductase activity
protein disulfide oxidoreductase activity
cellular homeostasis
homeostatic process
ferric iron binding
transition metal ion homeostasis
cellular iron ion homeostasis
cellular transition metal ion homeostasis
iron ion homeostasis
oxidoreductase activity, oxidizing metal ions
SCO0596 SCO2113 SCO2634 SCO0885 SCO5187
C
DNA integration
DNA metabolic process
DNA binding
nucleic acid binding
regulation of nucleobase-containing compound metabolic process
regulation of transcription, DNA-templated
regulation of RNA metabolic process
regulation of nucleic acid-templated transcription
regulation of RNA biosynthetic process
regulation of nitrogen compound metabolic process
regulation of macromolecule biosynthetic process
regulation of cellular macromolecule biosynthetic process
regulation of gene expression
cellular macromolecule biosynthetic process
RNA biosynthetic process
nucleic acid-templated transcription
RNA metabolic process
nucleobase-containing compound biosynthetic process
SCO4335 SCO7573 SCO5803 SCO6813 SCO6812 SCO6694 SCO3943 SCO6323 SCO3323 SCO5819 SCO6393 SCO4348 SCO4350 SCO6394 SCO6629
D
heterocyclic compound binding
organic cyclic compound binding
oxidoreductase activity, acting on paired donors, with incorporation or reduction of molecular oxygen
iron ion binding
small molecule biosynthetic process
peptidase activity, acting on L-amino acid peptides
electron carrier activity
monooxygenase activity
ectoine metabolic process
NADPH dehydrogenase activity
SCO0584 SCO1626 SCO6813 SCO6812 SCO6694 SCO6629 SCO6394 SCO6393 SCO6323 SCO5819 SCO5803 SCO5654 SCO5137 SCO4350 SCO4348 SCO3943 SCO3323 SCO3560 SCO4297 SCO7586 SCO1866 SCO7154 SCO4327 SCO0187 SCO1522 SCO6828 SCO7229 SCO6108 SCO2023 SCO4549 SCO1867 SCO2816 SCO7417 SCO7418 SCO5187 SCO7236 SCO3867 SCO0596 SCO2113

Figure S8: Gene Ontology enrichment analysis of the 7 clusters identified in the 499 differentially expressed genes, categorized by function into four clustered heatmaps. Related to Figure 4, 6 and S7A. Each heatmap shows the p-value for the enrichment of each GO-process. A) Genes related to reactive oxygen species, the ribosome or development process and cell wall formation. B) Oxireductase and iron / metal ion homeostasis. C) Regulation, biosynthesis and metabolism related to RNA and DNA. D) All other GO-annotations. E) This color palette is the legend for the column colors on top of each heatmap which displays which of the seven clusters each gene belongs to. The red palette covers cluster 1-3 (upregulated in M1152), while the blue palette covers cluster 4-7 (upregulated in M145). Note that no GO-processes were enriched for the genes in cluster 2.

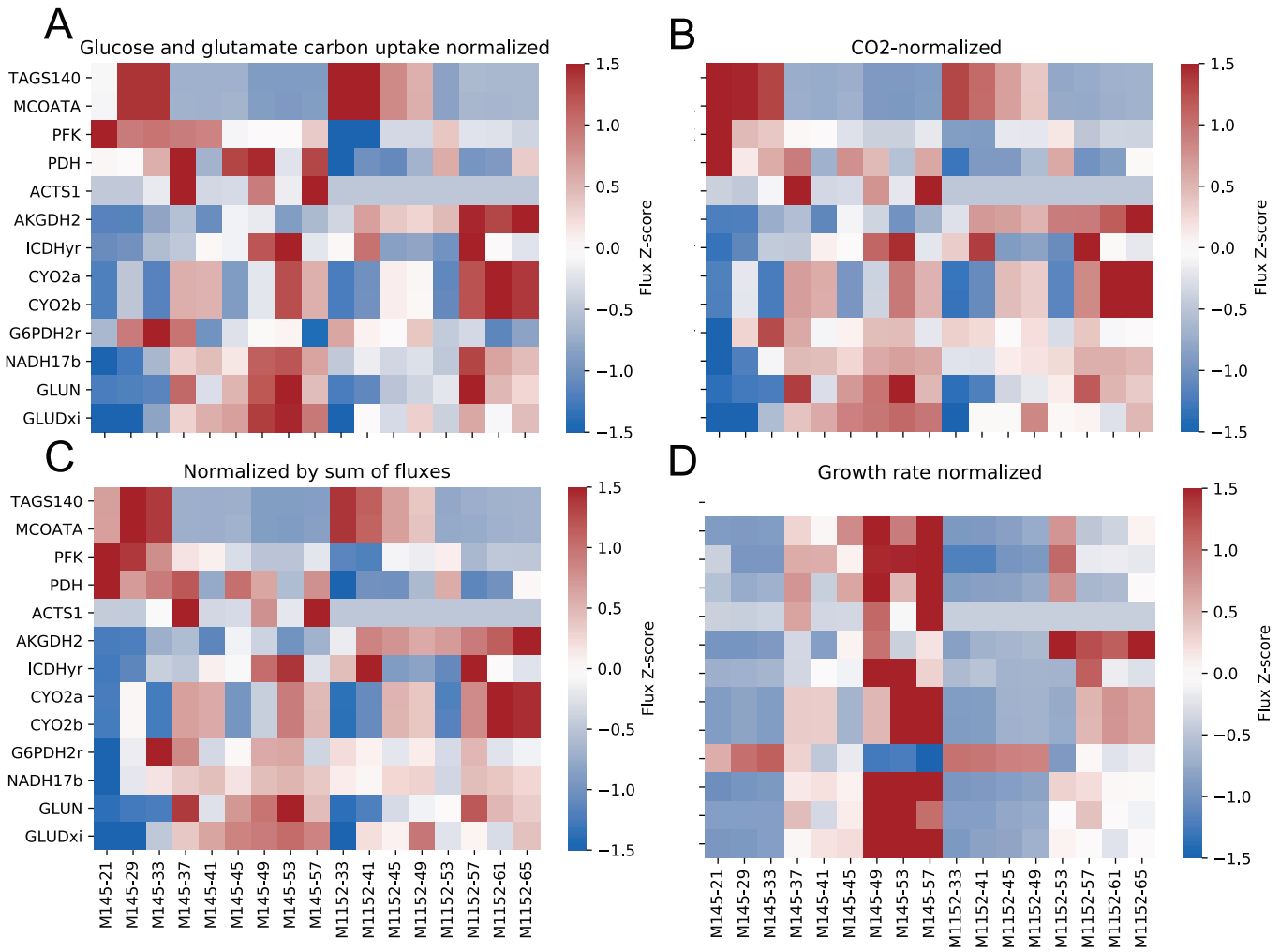

Figure S9: Comparison of normalization methods of randomly sampled fluxes, related to Figure 2D and 3D. Heatmap showing mean flux values normalized by A) total carbon uptake from glucose and glutamate, B) CO_2 production, C) sum of all fluxes and D) growth rate. Because the mean flux values in these reactions are different by several orders of magnitude, we display the data as standardized values (for each reaction).

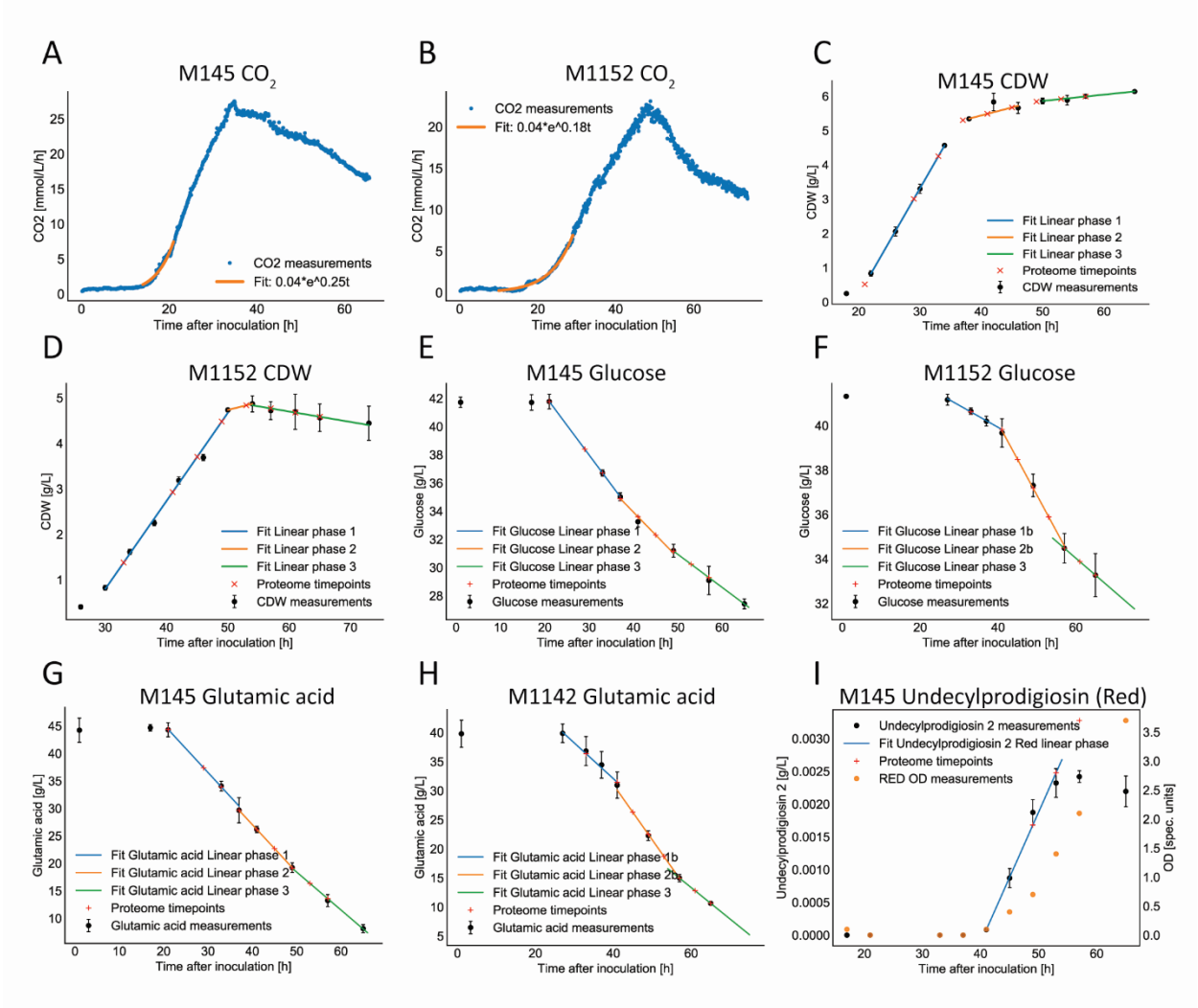

Figure S10: Estimation of rates for M145 and M1152 from cultivation data, related to Transparent methods, Table S1 and S2. A and B) Exponential fit of the CO_2 data to the exponential growth phase of M145 and M1152, respectively. C and D) Piecewise linear fit to estimate growth rates from the CDW measurements of M145 and M1152, respectively. E and F) Piecewise linear fit of glucose concentration in the cultivations of M145 and M1152, respectively. G and H) Piecewise linear fit of glutamic acid concentration in the cultivations of M145 and M1152, respectively. I) Estimated production rate of undecylprodigiosin (Red) in M145.

Table S1: Estimated cell dry weight (CDW) and growth, uptake and secretion rates for M145 at the timepoints of the proteome samples, related to Figure 2D. The unit is mmol/g DW/h for the uptake / secretion rates.

TAI	Estimated CDW [g/L]	Growth rate [h^{-1}]	Glucose	Glutamic acid	RED	Germicidin-A	Germicidin-B
21	0.517	0.246*	-4.528§	-11.462§	0	0	0
29	3.007	0.103	-0.779	-1.973	0	0	0
33	4.251	0.073	-0.551	-1.395	0	0	0
37	5.301	0.009	-0.338	-1.116	9.60E-05	5.70E-05	8.00E-05
41	5.487	0.008	-0.327	-1.078	9.20E-05	5.50E-05	7.80E-05
45	5.672	0.008	-0.316	-1.043	8.90E-05	5.40E-05	7.50E-05
49	5.845	0.003	-0.223	-0.803	8.70E-05	5.20E-05	7.30E-05
53	5.918	0.003	-0.220	-0.793	8.60E-05	5.10E-05	7.20E-05
57	5.991	0.003	-0.217	-0.784	8.50E-05	5.10E-05	7.10E-05

**This is the maximal growth rate predicted from the exponential fit of the CO_2 curve. The estimated rate from the linear fit of the CDW was unrealisticly high.*

§The values for the glucose and glutamate uptake rates are probably too high.

Table S2: Estimated cell dry weight (CDW) and growth, uptake and secretion rates for M145 at the timepoints of the proteome samples, related to Figure 3D. The unit is mmol/g DW/h for the uptake / secretion rates.

TAI	Estimated CDW [g/L]	Growth rate [h^{-1}]	Glucose	Glutamic acid	RED	Germicidin-A	Germicidin-B
33	1.379	0.140	-0.399	-3.017	0	0	0
41	2.929	0.066	-0.188	-1.421	0	0	0
45	3.704	0.052	-0.394	-1.415	0	0	0
49	4.478	0.043	-0.382	-1.374	0	0	0
53	4.835	0.007	-0.372	-1.336	0	3.00E-06	1.56E-05
57	4.767	-0.005	-0.177	-0.772	0	3.10E-06	1.58E-05
61	4.676	-0.005	-0.180	-0.787	0	3.10E-06	1.61E-05
65	4.585	-0.005	-0.184	-0.803	0	3.20E-06	1.64E-05

Transparent methods

Sco-GEM consensus model reconstruction and development

Sco-GEM, the community consensus model for *Streptomyces coelicolor* is developed, maintained, hosted and publicly available on GitHub (https://github.com/SysBioChalmers/Sco-GEM). When we refer to files in the following sections, we use the file names and relative to the main folder in this GitHub repository. By hosting the model on GitHub, we make the reconstruction transparent, the data accessible, provide a structure framework for further development by the community. To this end we also created a channel on Gitter dedicated to Sco-GEM questions and discussions (https://gitter.im/SysBioChalmers/Sco-GEM). The model repository was created using memote (Lieven et al., 2018) and we use a GitFlow structure with two main branches, the *devel* branch contains the most recent changes while the *master* branch contains the stable releases. All new features or bug fixes are performed in separate branches that are incorporated into the *devel* branch through *pull requests.* Semantics for branch names and commit messages are described in *CONTRIBUTING.rst*. The main script language for the model reconstruction is python (version > 3.6), with the exception being the *feat/ecModel* branch with the development of the enzyme-constrained model (EcSco-GEM) where Matlab (version > 7.3) is used.

In terms of folder structure data files, scripts and model files are stored in *ComplementaryData*, *ComplementaryScripts*, and *ModelFiles*, respectively. In the main folder we find the following files:

- *.gitignore*: File which describes file formats automatically ignored by git
- *.gitconfig*: Git config file
- *.gitmodules*: List of linked submodules
- *CONTRIBUTING.rst*: Guidelines describing how to contribute
- *README.md*: General information about the repository
- *HISTORY.rst*: History of model version releases
- *LICENSE.md*: License information
- *memote.ini*: File created by memote (Lieven et al., 2018)
- *requirements.txt*: List of python-packages required to run the model reconstruction

- *.travis.yml*: Config file for automatization of memote with Travis (https://travis-ci.org/)

Sco-GEM can be reconstructed at any time using the python script *ComplementaryScripts/reconstruct_scoGEM.py*. Each task of the reconstruction process is performed in a separate script and associated with an issue on GitHub (**Data Set S1**, **Tab 1**). The details of each task are described in the following paragraphs.

Curate identified issues in iKS1317

We used iKS1317 (Kumelj et al., 2019) as the starting point for the reconstruction of Sco-GEM. Since the publication of iKS1317, several issues had been identified and these were curated as the initial step in the reconstruction pipeline. The curations include correcting the mass and charge balance of the reactions NOR_syn, OAADC, SEPHCHCS and DIOP5OR, and correcting the ec-code, KEGG annotation and gene association for the reactions 3OXCOAT, MMSYNB, PGMT, PPM, ME1, GLUDyi, GLUSx, GLUSy and GLUN.

Curate and add reactions from Sco4

The Sco4 GEM of *S. coelicolor* (Wang et al., 2018) contained additional reactions that we wanted to include in Sco-GEM. However, prior to adding content from Sco4 we curated issues that had been identified since publication. Eleven reactions were found to be either duplicated or wrong in Sco4, and these were removed: RXN0-5224, METHYLGLUTACONYL-COA-HYDRATASE-RXN, GLU6PDEHYDROG-RXN, RXN-15856, 1.14.13.84-RXN_NADPH, R03998, R03999, R09692_NADPH, RXN-9930, 1.17.1.1-RXN_NADH, R09692_NADH. We additionally updated the gene annotations of the following reactions: RMPA, ABTDG, PROD2, THRPDC, ADCL, OXPTNDH, GLNTRS, CU2abc, CBIabc, CBL1abc, GSNt2, INSt2 and PDH.

To enable addition of reactions from Sco4 (Wang et al., 2018) to Sco-GEM we mapped reactions added during the Sco4 development to reactions present in iKS1317 (Kumelj et al., 2019). This mapping was performed semi-automatically: automatic mapping using KEGG and BioCyc annotations followed by manual curation. In total, 394 new reactions and 404 new metabolites were added from Sco4 to Sco-GEM (**Data Set S1, Tab 5 and 6**). Most of the reactions and metabolites added from Sco4 had IDs from the MetaCyc database (Caspi et al.,

2014), containing characters such as dash or parentheses not properly handled by the SBML parser in COBRApy (Ebrahim et al., 2013). Thus, the ID of all reactions and metabolites added from Sco4 were changed to the correct BiGG ID if possible, otherwise a new ID was created according to the guidelines given in BiGG (King et al., 2016). KEGG (Kanehisa, 2000) and MetaNetX (Moretti et al., 2016) identifiers were included as annotations when possible. Full lists of the IDs and annotations given to reactions and metabolites added from Sco4 are found in the GitHub repository folder *ComplementaryData/curation* as *added_sco4_reactions.csv* and *added_sco4_metabolites.csv*, respectively.

Add gene annotations, reactions and metabolites to Sco-GEM from iAA1259

Based on supplementary files 4 and 5 from iAA1259 (Amara et al., 2018) which list the reactions and metabolites added in iAA1259, we identified 44 reactions and 31 metabolites present in neither Sco4 or iKS1317 (**Data Set S1, Tab 7 and 8**). These 44 reactions were added from iAA1259 and were mainly related to coelimycin biosynthesis, xylan and cellulose degradation and butyrolactones pathway. We further incorporated the modification of 27 reactions curated in iAA1259, associated with oxidative phosphorylation, futalosine pathway or chitin degradation (**Data Set S1, Tab 9**). These curations mainly updated gene-reaction rules but also updated reaction bounds and deletion of two reactions (CFL and DHFUTALS). Finally, we incorporated the biomass-function which was updated in iAA1259.

Change direction of reactions that were backwards irreversible

The pipeline for reconstruction of the enzyme-constrained model required all reactions to be either reversible or forward irreversible (i.e. reactions with bounds (-1000, 0) are not allowed). Therefore, all backward irreversible reactions were rewritten (substrates were changed to products and *vice versa*) so they could be represented as forward irreversible.

Fix missing / wrongly annotated reactions and metabolites

We identified several minor issues related to reaction and metabolite IDs or annotations. These may come from the current or previous model reconstruction efforts. These issues include:

- Misspelled IDs or annotations
- Empty annotations in SBML file
- Wrong BioCyc annotations for metabolites and reactions in the germicidin pathway

- Update all MetaNetX annotations
- Exchange reactions given BioCyc annotations
- Fix chebi annotations so they comply with the MIRIAM identifiers
- Mixed up IDs for actACPmmy and malACPmmy

Create pseudo-metabolites for NADH/NADPH and NAD+/NADP+ to use in reaction were the redox cofactor is not known

For some redox reactions added from Sco4, it was not sure if NADH/NAD+ or NADPH/NADP+ was the participating cofactor pair. In this case, both possibilities were included in Sco4. However, to avoid duplicated reactions and make it explicit that the cofactor is unknown we changed these reactions to use pseudo-metabolites (acceptor_c and donor_c) as the cofactor pair. We then also included pseudo-reactions which converts NADH/NADPH and NAD+/NADP+ to donor_c and acceptor_c, respectively [pseudo-reaction IDs: PSEUDO_DONOR_NADH; PSEUDO_DONOR_NADPH; PSEUDO_ACCEPTOR_NAD; PSEUDO_ACCEPTOR_NADP). In total 17 enzymatic reactions use these pseudo-metabolites as cofactor pair: 3OCHOCDH; OXCOADH; 4DPCDH; 4HYDPRO; 4NITROB; AHLGAL; AHOPS; CADHX; DDALLO; DPCOX; GDP64HRD; HDAPMO; PHYFLUDS; HYTDES; SORBDH; ZCARDS; ZCAROTDH2.

Add SBO terms to genes, reactions and metabolites

SBO (Systems Biology Ontology) (Courtot et al., 2011) terms were included as annotations of reactions, genes and metabolites according to **Data Set S1, Tab 10**.

Update the biomass reaction

In iAA1259, the biomass reaction was curated in respect to 2-demethylmenaquinol and menaquinol, however, this resulted in a biomass reaction that combined described more than 1 g per gDCW. In addition, the biomass reaction of all *S. coelicolor* models have described small molecule and protein co-factors/prosthetic groups as components, where their abundance was arbitrarily set to complement the remaining biomass components to reach 1 g per gDCW. This is likely a gross overestimation for many of these molecules, and this proved problematic for initial simulations with the enzyme constrained model. In contrast to enzymes of central carbon metabolism, enzymes involved in biosynthesis of such co-factors and prosthetic groups

have typically lower efficiency, such that large fractions of the protein allocation would have to be devoted to these pathways if the abundances are overestimated.

The availability of proteomics data has allowed us to give more reasonable estimates of abundance of protein-linked cofactors and prosthetic groups. The new biomass reaction was estimated through the following steps:

1. By querying UniProt, a list of prosthetic groups per protein were collated (*ComplementaryData/biomass/prosthetic_groups_uniProt.txt*) and further processed (*ComplementaryScripts/ecModel/prostheticGroups.m*) as detailed below.
2. If *metal* was specified as cofactor, the abundance was split over $cobalt^{2+}$, $cupper^{2+}$, $iron^{2+}$, $zinc^{2+}$, $nickel^{2+}$, $calcium^{2+}$, $potassium^{+}$, $magnesium^{2+}$ and $manganese^{2+}$.
3. Dipyrromethane is generated by the enzyme itself from its substrate and is therefore not further considered.
4. From the M145 and M1152 cultivation data, quantitative proteomics was estimated as detailed below.
5. Cofactor abundances were estimated by combining the estimated protein levels and the protein cofactor annotation (available at *ComplementaryData/biomass/ prosthetic_groups_mets.txt*)
6. To simplify fitting of biomass components, the full biomass reaction was split into the pseudometabolites *lipid*, *dna*, *rna*, *protein*, *carbohydrate, cell_wall* and *misc*, with the latter containing the cofactors (*ComplementaryData/biomass/standard_biomass.txt*).
7. After updating the abundances of the cofactors, the remaining *misc* metabolites were refitted to ensure that the total biomass adds up to 1 g per gDCW.

The updated composition (*ComplementaryData/biomass/biomass_scaled.txt*) was subsequently used to modify the model stoichiometry (*fix_biomass.py*). A comparison of the updated biomass reaction and the biomass reaction in iAA1259 is presented in **Data Set S1, Tab 2**.

Model reversibility

By using the python-API (https://gitlab.com/elad.noor/equilibrator-api) of eQuilibrator (Flamholz et al., 2012) we calculated the change in Gibbs free energy for 770 reactions (**Data**

Set S1, Tab 3). eQuilibrator can only calculate the change in Gibbs free energy for intracellular reactions (i.e. not transport and exchange reactions) where all metabolites are mapped to KEGG (Kanehisa, 2000; Kanehisa et al., 2019). The calculations are based on the component contribution method (Noor et al., 2013). The change in Gibbs free energy was calculated at standard conditions (25 °C, 1 bar), pH7 and 1mM concentration of reactants, denoted $\Delta_r G'^m$ in eQuilibrator. We then applied a threshold of -30 kJ/mol to define a reaction as irreversible (Bar-Even et al., 2012; Feist et al., 2007), and compared the calculated reversibility with the reversibility of these reactions in the model prior to curation. We found that the reversibility was equal for 56.9% (438 / 770) of the reactions (**Figure 1E**). The majority of differences were reactions that were irreversible in the model but classified as reversible using the calculated values for the change in Gibbs free energy (35%; 273/770; **Figure 1E**).

Using the set of growth data and knockout data, we evaluated the effect of the suggested changes in reaction reversibility: by randomly applying these changes to 10 reactions at the time, we identified 13 single, 22 pairs and 13 triplets of reactions (consisting of 55 unique reactions) that reduced model accuracy when the reversibility was changed based on the change in Gibbs free energy (**Data Set S1, Tab 11**). Then we used the data set of growth and gene knockout phenotypes (Kumelj et al., 2019) to identify another 6 reactions that caused erroneous predictions if the reversibility were changed (PROD2, ARGSS, OCT, URIK1, URIK2, and UPPRT). These 61 reactions were discarded from having the reversibility changed, resulting in a total of 271 reactions with changed reversibility.

Energetic cofactors, including ATP, NADPH, NADH, FAD and any quinone, were involved in 284 of the 770 reactions for which the change in Gibbs free energy was calculated. Of the 114 reactions involving ATP, 82 reactions had an estimated change in Gibbs free energy between ±30 kJ/mol, indicating that the reactions were reversible. Because one assumes that ATP-driven reactions in general are irreversible (Thiele and Palsson, 2010), the reversibility of these 82 reactions were manually curated (**Data Set S1, Tab 12**). For the 7 quinone-associated reactions for which the change in Gibbs free energy was calculated (CYTBD2, NADH17b, NADH10b, MBCOA2, G3PD5, PDH3, NADH2r) all were defined as irreversible as previously suggested (Thiele and Palsson, 2010). The reversibility of reactions involving any of the other energetic cofactors were treated as any other reaction as previously described.

Analysis and annotation of transport reactions

Gene annotations, substrate and transport class information were mostly extracted from Transport DB 2.0 (Elbourne et al., 2017) and TCDB (Saier et al., 2016). Then, transport proteins were extracted from IUBMB-approved Transporter Classification (TC) System and categorized into 9 main classes (**Figure 1F**): 1) ABC transporter; 2) PTS transporter; 3) Proton symporter; 4) Sodium symporter; 5) Other symporter; 6) Proton antiport; 7) Other antiport; 8) Facilitated diffusion; 9) Simple diffusion. For those transport proteins with an ambiguous substrate annotation in TCDB, the specific substrate annotation was obtain by extracting annotations from KEGG (Kanehisa, 2000; Kanehisa et al., 2019), UniProt (The UniProt Consortium, 2019) or through BLAST homology search (NCBI Resource Coordinators, 2017) using a similarity threshold of 90% (**Data Set S1, Tab 4**).

Subsystem annotations

We leveraged the KEGG and BioCyc annotations of each individual reaction to extract a draft subsystem and pathway annotation for each reaction. For KEGG, this was achieved by using the python module BioServices (Cokelaer et al., 2013) while we used PythonCyc (https://github.com/latendre/PythonCyc) and PathwayTools (Karp et al., 2016) to extract pathway annotations from BioCyc (Karp et al., 2019).

The draft annotations were then curated, and each reaction was annotated to one out of 15 subsystems. When no or multiple annotations were extracted from the databases we used adjacent reactions in the metabolic network to infer the single, most correct annotation. These 15 subsystem categories are based on the categories of the KEGG Pathway Maps for metabolism (https://www.genome.jp/kegg/pathway.html) but we have included three additional categories to cover all aspects of the model: Biomass and maintenance functions, Membrane Transport, and Exchange (**Figure S1**).

We also annotated 1964 of the 2552 reactions to one out of 128 different pathways. The remaining 588 are mostly transport and exchange reactions, or possibly reactions not fitting into any of these pathways.

Export model file with alphabetical ordering

An import feature with GitHub is the ability to easily see changes in text files after every commit. However, COBRApy (Ebrahim et al., 2013) doesn't sort the list of reactions, metabolites and genes before the SBML-file is written and this make it look like there was a

lot of changes even when the model is unchanged. Thus, we now sort these lists before writing to file. The export function also stores the model-file in the YAML format which is more readable than SBML (XML). Finally, the export function creates the *requirements.txt* file which holds information about all non-standard python modules necessary to run the model reconstruction.

Development of enzymatically constrained (EcSco-GEM) model

An enzyme-constrained version of the Sco-GEM model (denoted EcSco-GEM) was generated using GECKO (Sánchez et al., 2017). The GECKO method enhances an existing GEM by explicitly constraining the maximum flux through each reaction by the maximum capacity of the corresponding enzyme, given by the product of the enzyme abundance and catalytic coefficient. Both reversible reactions and reactions catalysed by isoenzymes (redundant genes) are handled automatically by the GECKO method by splitting each occurrence into individual reactions. The Sco-GEM v1.1 model was modified using GECKO version 1.3.4. Kinetic data, in the form of k_{cat} values (s^{-1}), were automatically collected from BRENDA (Jeske et al., 2019). If BRENDA did not report a k_{cat} value for an enzyme, GECKO searched for alternative k_{cat} values by reducing specificity, on the level of substrate, enzymatic activity (EC number) and organism.

A total of 4753 k_{cat} values were matched, including separate values for forward and backward direction for reversible reactions, of which:

- 53 were matched with organism (S. coelicolor) and correct substrate
- 1541 were matched with closest organism and correct substrate
- 236 were matched with organism (S. coelicolor) and any substrate
- 15 were matched with organism (S. coelicolor) and any substrate, reported specific activities instead of k_{cat} (corrected in the model for molecular weight of the enzyme)
- 2586 were matched with closest organism and any substrate
- 322 were matched with any organism and any substrate, reported specific activities instead of k_{cat} (corrected in the model for molecular weight of the enzyme)

The algorithm first looped through these criteria above, with the full EC code. If no match

could be found, wildcards were added (e.g. EC2.3.4.- instead of EC2.3.4.5), followed by going through the list of criteria above. The statistics there is:

- 4178 were matched without any wildcards (full EC code)
- 544 were matched after adding one wildcard
- 21 were matched after adding two wildcards (e.g. EC2.3.-.-)
- 10 were matched after adding three wildcards
- 0 were matched after adding four wildcards

Using the initial set of BRENDA-suggested k_{cat} values, the model was evaluated to support simulation of experimentally measured growth rates. During this testing the NAD(H)/NAD(P)H pseudo-reactions were blocked to avoid infeasible loops.

The following k_{cat} values were identified as growth limiting resulting in the stated manual curations:

- Chorismate synthase (CHORS; EC4.2.3.5; SCO1496; Q9KXQ4)
  Sco-GEM uses 5-O-(1-Carboxyvinyl)-3-phosphoshikimate as name of the main substrate, while BRENDA uses its synonym 5-enolpyruvylshikimate 3-phosphate. This prevented automatically finding the substrate. Hence, the kcat was manually changed to 0.87 s^{-1}, as measured from *N. crassa* (Rauch et al., 2008).
- Phosphoribosylformylglycinamidine synthase (PRFGS; EC6.3.5.3; SCO4077 and SCO4078 and SCO4079; Q9RKK5 and Q9RKK6 and Q9RKK7)
  k_{cat} suggested by BRENDA used NH4+ as substrate, instead of glutamine. Specific activity using glutamine is provided for *E. coli*: 2.15 µmol/min/mg protein (Schendel et al., 1989). Assuming molecular weight of 141 kDa, this translates to k_{cat} = 5.05 s^{-1}.

- Methylmalonate-semialdehyde dehydrogenase (malonic semialdehyde) (MMSAD3; EC1.2.1.27; SCO2726; Q9L1J1)
  k_{cat} suggested by BRENDA is from archaea, instead use k_{cat} value of 2.2 s^{-1} from *B. subtilis* (Talfournier et al., 2011).

- Phosphoribosyl-ATP pyrophosphatase (PRATPP; EC3.6.1.31; SCO1439; Q9EWK0) k_{cat} suggested by BRENDA was calculated from specific activity in *Salmonella enterica*, but the reported value was measured in cell extract, not from purified enzyme. Instead, use specific activity from *S. cerevisiae*: 332 umol/min/mg protein (Keesey et al., 1979). Assuming molecular weight of 95 kDa, this translates to a k_{cat} of 526 s^{-1}.

- Glyceraldehyde 3-phosphate dehydrogenase (Q9Z518/EC1.2.1.12) - assigned k_{cat} from Corynebacterium glutamicum was highly growth limiting. Instead use specific activity measured of pentalenolactone sensitive gapdh in Streptomyces arenae: 112 umol/min/mg protein (Maurer et al., 1983).

Then, separate models were created for each strain (the gene clusters for actinorhodin, undecylprodigiosin, CDA and coelimycin P1 were removed to create M1152) and for each time point by using estimated growth, uptake rates of glutamate and glucose, secretion rates of undecylprodigiosin, germicidin A and B and proteome measurements. The estimated growth, uptake and secretion rates were estimated from raw measurements across three biological replicates (details provided in the last section). These time point specific models (9 time points for M145, 8 time points for M1152) were used to analyse the activity in individual metabolic pathways through random sampling (Bordel et al., 2010). We also created one EcSco-GEM model for each strain with a global constraint on the protein usage instead of specific protein usage, which were used for model quality control.

Continuous integration and quality control with memote

Validation and quality assessment of Sco-GEM is carried out using the test-suite in memote (Lieven et al., 2018). Memote provides by default a large range of tests, which we have used to identify issues and possible improvements. The test suite reports descriptive model statistics such as the number of genes, reactions and metabolites, and also checks the presence of SBO terms and annotations, the charge and mass balance of all reactions, the network topology and find energy-generating cycles (Fritzemeier et al., 2017). Additionally, we incorporated custom tests into the memote test-suite to automatically compare predicted phenotypes with experimental data in different growth media and for different knockout mutants. In addition to the classical binary classifiers accuracy, sensitivity and specificity we also report the Matthews correlation coefficient which is considered to be more reliable when

the number of elements in each classification category is skewed (Chicco and Jurman, 2020). The Matthews correlation coefficient (*MCC*) is calculated from the true positive (*TP*), false positive (*FP*), true negative (*TN*) and false negative (*FN*) values as $MCC = \frac{TP \cdot TN - FP \cdot FN}{\sqrt{(TP+FP)\cdot(TP+FN)\cdot(TN+FP)\cdot(TN+FN)}}$. The experimental growth and knockout data are extracted from (Kumelj et al., 2019). As a separate evaluation, we applied another method for identifying internal and unrealistic energy-generating cycles (Noor, 2018) , and no such cycles were found in Sco-GEM.

The simplest use of memote is generating snapshot reports showing the current state of the model. However, by integrating Travis CI [https://travis-ci.com/] into the gitHub repository, memote can be used to create a continuous report displaying how each commit affects the model quality. Memote version 0.9.12 was used in this work, and the memote snapshot report for Sco-GEM is given in the **Supplemental Information**.

Random sampling, normalization and pathway analysis

Because of the huge number of reactions in the EcSco-GEM, it is challenging to sample the solution space appropriately: we have chosen to use the method provided in the Raven Toolbox 2 (Bordel et al., 2010; Wang et al., 2018), which samples the vertices of the solution space. The drawback of this method is that it will not result in a uniform sampling of the solution space. However, it is more likely to span the entire solution space and also not prone to get stuck in extremely narrow parts of the solution space, which may happen with variants of the hit-and-run algorithm (Haraldsdóttir et al., 2017; Kaufman and Smith, 1998; Megchelenbrink et al., 2014). For each of the time points for each strain (17 different conditions in total) we constrained exchange reactions between 99% and 101% of the measured rates and generated 5000 random flux distributions with Gurobi as the solver. The reactions catalysed by isoenzymes were combined into the set of reactions in Sco-GEM and the reactions providing protein for each reaction. The mean of the 5000 flux distributions for each metabolic reaction was used in the following analysis.

Finally, for each of the 17 conditions, the mean fluxes were normalized by the CO_2 production rate. Then, the normalized mean fluxes were summarized for each metabolic pathway by using the curated pathway annotations, and we consider this a measure of the metabolic activity in

each pathway. To ease visual interpretation of this data we used the function clustermap with default parameters in Seaborn version 0.9.0 (Michael Waskom et al., 2018) (which uses Scipy v1.3.1 (Virtanen et al., 2020)) to perform hierarchical clustering of pathways based on the metabolic activity in M145 (**Figure 2D**). We then kept this order in **Figure 3D** to enable strain comparison.

Since glucose and glutamate uptake rates, as well as growth rates were significantly different in the two strains and at different time points, normalization of the data was necessary to compare flux distributions. We tested various proxies as indicators of overall metabolic activity for normalization, namely CO_2 production; the total carbon uptake from glucose and glutamate; growth rate and mean flux value. As golden standard, we compared the fluxes through individual reactions that are well documented to change in M145 in response to the phosphate depletion (**Figure S9**). Normalization based on CO_2 production was tested and gave similar results than the data normalized on total carbon uptake from glucose and glutamate (**Figure S9A and S9B**. The data normalized by the sum of fluxes showed similar patterns as those achieved by glucose/glutamate and CO_2-normalized data but was noisier (**Figure S9C**). Considering the huge differences in growth rate, the growth-normalized data masked any other flux patterns (**Figure S9D**). The fact that different normalizations provided similar differences in metabolic fluxes proved that the inferred changes in metabolism were not artefacts of the normalization method but represent true metabolic activity of each strain.

Strains, cultivation conditions, sampling procedures, and analyses of media components and secondary metabolites

Experiments were performed using strain M145 of *S. coelicolor* A3(2) and its derivatives M1146 and M1152. The latter two are lacking the 4 major BGCs for actinorhodin (Act), undecylprodigiosin (Red), coelimycin P1 (Cpk), and calcium-dependent antibiotic (CDA), while M1152 is also carrying the pleiotropic, previously described antibiotic production enhancing mutation *rpoB* [S433L] (Gomez-Escribano and Bibb, 2011; Hu et al., 2002). All strains were kindly provided by Mervyn Bibb at John-Innes-Centre, Norwich, UK.

Triplicate cultivations of the strains were performed based on germinated spore inoculum on 1.8 L phosphate-limited medium SSBM-P, applying all routines of the optimized submerged batch fermentation strategy for *S. coelicolor* established and described before (Wentzel et al., 2012). All media were based on ion-free water, and all chemicals used were of analytical grade.

In brief, spore batches of M145, M1146 and M1152 were generated by cultivation on soy flour-mannitol (SFM) agar plates (Kieser et al., 2000), harvesting by scraping off spores and suspension in 20% (v/v) glycerol, and storage in aliquots at −80 °C. 10^9 CFU of spores of each strain were germinated for 5 hours at 30 °C and 250 rpm in 250 mL baffled shake-flasks with 2 g of 3 mm glass beads and 50 mL 2x YT medium (Claessen et al., 2003). The germinated spores were harvested by centrifugation (3200 x g, 15 °C, 5 min) and re-suspended in 5 mL ion-free water. An even dispersion of the germinated spores was achieved by vortex mixing (30 s), ensuring comparable inocula among biological replicas. Each bioreactor (1.8 liter starting volume culture medium in a 3-liter Applikon stirred tank reactor) was inoculated with 4.5 mL germinated spore suspension (corresponding to $9x10^8$ CFU). Phosphate-limited medium SSBM-P (Nieselt et al., 2010) consisted of Na-glutamate, 55.2 g/L; D-glucose, 40 g/L; $MgSO_4$, 2.0 mM; phosphate, 4.6 mM; supplemented minimal medium trace element solution SMM-TE (Claessen et al., 2003), 8 mL/L and TMS1, 5.6 mL/L. TMS1 consisted of $FeSO_4$ x 7 H_2O, 5 g/L; $CuSO_4$ x 5 H_2O, 390 mg/L; $ZnSO_4$ x 7 H_2O, 440 mg/L; $MnSO_4$ x H_2O, 150 mg/L; Na_2MoO_4 x 2 H_2O, 10 mg/L; $CoCl_2$ x 6 H_2O, 20 mg/L, and HCl, 50 mL/L. Clerol FBA 622 fermentation defoamer (Diamond Shamrock Scandinavia) was added to the growth medium before inoculation. Throughout fermentations, pH 7.0 was maintained constant by automatic addition of 2 M HCl. Dissolved oxygen levels were maintained at a minimum of 50% by automatic adjustment of the stirrer speed (minimal agitation 325 rpm). The aeration rate was constant 0.5 L/(L x min) sterile air. Dissolved oxygen, agitation speed and carbon dioxide evolution rate were measured and logged on-line, while samples for the determination of cell dry weight, levels of growth medium components and secondary metabolites concentrations, as well as for transcriptome and proteome analysis were withdrawn throughout the fermentation trials as indicated in **Figure 2B**. For transcriptome analysis, 3 × 4 ml culture sample were applied in parallel onto three 0.45 µm nitrocellulose filters (Millipore) connected to vacuum. The biomass on each filter was immediately washed twice with 4 ml double-autoclaved ion-free water pre-heated to 30 °C, before the filters were collected in a 50 ml plastic tube, frozen in liquid nitrogen and stored at -80 °C until RNA isolation. For proteome analysis, 5 ml samples were taken and centrifuged (3200 x g, 5 min, 4 °C), and the resulting cell pellets frozen rapidly at -80 °C until further processing.

Levels of phosphate were measured spectrophotometrically by using the SpectroQuant Phosphate test kit (Merck KGaA, Darmstadt, Germany) following the manufacturer's instructions after downscaling to 96-well plate format. D-glucose and L-glutamate concentrations were determined by LC-MS using suitable standards, and measured concentrations were used to estimate specific uptake and excretion rates. Undecylprodigiosin (Red) levels were determined spectrophotometrically at 530 nm after acidified methanol extraction from the mycelium (Bystrykh et al., 1996). To determine relative amounts of actinorhodins (determined as total blue pigments, TBP), cell culture samples were treated with KOH (final concentration 1 M) and centrifuged, and the absorbance of the supernatants at 640 nm was determined (Bystrykh et al., 1996). Quantification of germicidin A and B was performed using targeted LC-MS analytics.

Proteomics

Sample preparation and NanoUPLC-MS analysis

Quantitative proteomics were performed using pipeline previously described (Gubbens et al., 2012). Mycelium pellets for proteome analysis were thawed and resuspended in the remaining liquid. 50 µL re-suspended mycelium was withdrawn and pelleted by centrifugation. 100 µL lysis buffer (4% SDS, 100 mM Tris-HCl pH 7.6, 50 mM EDTA) was added, and samples were sonicated in a water bath sonicator (Biorupter Plus, Diagenode) for 5 cycles of 30 s high power and 30 s off in ice water. Cell debris was pelleted and removed by centrifugation. Total protein was precipitated using the chloroform-methanol method described before (Wessel and Flügge, 1984). The pellet was dried in a vacuum centrifuge before dissolving in 0.1% RapiGest SF surfactant (Waters) at 95 °C. The protein concentration was measured at this stage using BCA method. Protein samples were then reduced by adding 5 mM DTT, followed by alkylation using 21.6 mM iodoacetamide. Then trypsin (recombinant, proteomics grade, Roche) was added at 0.1 µg per 10 µg protein. Samples were digested at 37 °C overnight. After digestion, trifluoroacetic acid was added to 0.5% followed by incubation at 37 °C for 30 min and centrifugation to remove MS interfering part of RapiGest SF. Peptide solution containing 8 µg peptide was then cleaned and desalted using STAGE-Tipping technique (Rappsilber et al., 2007). Final peptide concentration was adjusted to 40 ng/µL using sample solution (3% acetonitrile, 0.5% formic acid) for analysis.

200 ng (5 µL) digested peptide was injected and analysed by reversed-phase liquid chromatography on a nanoAcquity UPLC system (Waters) equipped with HSS-T3 C18 1.8 µm, 75 µm X 250 mm column (Waters). A gradient from 1% to 40% acetonitrile in 110 min (ending with a brief regeneration step to 90% for 3 min) was applied. [Glu^1]-fibrinopeptide B was used as lock mass compound and sampled every 30 s. Online MS/MS analysis was done using Synapt G2-Si HDMS mass spectrometer (Waters) with an UDMS^E method set up as described in (Distler et al., 2014).

Data processing and label-free quantification

Raw data from all samples were first analysed using the vender software ProteinLynx Global SERVER (PLGS) version 3.0.3. Generally, mass spectrum data were generated using an MS^E processing parameter with charge 2 lock mass 785.8426, and default energy thresholds. For protein identification, default workflow parameters except an additional acetyl in N-terminal variable modification were used. Reference protein database was downloaded from GenBank with the accession number NC_003888.3. The resulted dataset was imported to ISOQuant version 1.8 (Distler et al., 2014) for label-free quantification. Default high identification parameters were used in the quantification process. TOP3 result was converted to PPM (protein weight) and send to the modelers and others involved in interpreting the data (**Data Set S3**).

TOP3 quantification was filtered to remove identifications meet these two criteria: 1. identified in lower than 70% of samples of each strain and 2. sum of TOP3 value less than 1×10^5. Cleaned quantification data was further subjected to DESeq2 package version 1.22.2 (Love et al., 2014) and PCA was conducted after variance stabilizing transformation (vst) of normalized data.

Transcriptomics

RNA extraction and quality control

Bacteria were lysed using RNAprotect Bacteria (Qiagen) and following the manufacturer´s instruction. Briefly, filters containing bacteria were incubated with 4 ml of RNAprotect Bacteria reagent. After centrifugation, resulting samples were lysed using 500 µl of TE buffer (10 mM Tris·Cl, 1 mM EDTA, pH 8.0) containing 15 mg/ml lysozyme using 150-600 µm diameter glass beads (Sigma) agitated at 30 Hz for 5 minutes in the TissueLyser II (Qiagen).

Total RNA was extracted using RNeasy mini kit (Qiagen) and 700 µl of the resulting lysate complemented with 470 µl of absolute ethanol. RNAase-free DNase set (Qiagen) and centrifugation steps were performed to prevent DNA and ethanol contamination. Elution was performed using 30 µl of RNase-free water and by reloading the eluate on the column to improve the RNA yield. The RNA concentration was measured using Qubit RNA BR Assay Kit (ThermoFisher Scientific), RNA purity was assessed using A260/A280 and A260/A230 ratio using the Nano Drop ND-1000 Spectrophotometer (PEQLAB). RNA Integrity Number was estimated using RNA 6000 Nano Kit (Agilent) and the Bioanalyzer 2100 (Agilent).

Library preparation and sequencing

A total of 1 µg of total RNA was subjected to rRNA depletion using Ribo-Zero rRNA Removal Kit Bacteria (Illumina). The cDNA libraries were constructed using the resulting tRNA and the NEBNext Ultra II Directional RNA Library Prep Kit (NEB). Libraries were sequenced as single-reads (75 bp read length) on an Illumina NextSeq500 platform at a depth of 8–10 million reads each.

RNA-seq data assessment and analysis

Sequencing statistics including the quality per base and adapter content assessment of resulting transcriptome sequencing data were conducted with FastQC v0.11.5 (Andrews, 2016). All reads mappings were performed against the reference strain of *Streptomyces coelicolor A3(2)* (RefSeq ID NC_003888.3). The mappings of all samples were conducted with HISAT2 v2.1.0 (Kim et al., 2015). As parameters, spliced alignment of reads was disabled, and strand-specific information was set to reverse complemented (HISAT2 parameter --no-spliced-alignment and --rna-strandness "R"). The resulting mapping files in SAM format were converted to BAM format using SAMtools v1.6 (Li et al., 2009). Mapping statistics, including strand specificity estimation, percentage of mapped reads and fraction exonic region coverage, were conducted with the RNA-seq module of QualiMap2 v2.2.2-dev (Okonechnikov et al., 2016). Gene counts for all samples were computed with featureCounts v1.6.0 (Liao et al., 2014) based on the annotation of the respective reference genome, where the selected feature type was set to transcript records (featureCounts parameter -t transcript).

Normalization and differential gene expression

Raw count files were imported into Mayday SeaSight (Battke and Nieselt, 2011) for common, time-series-wide normalization. For this, the raw counts of all biological replicates of one strain

across the time-series were log2-transformed (with pseudocount of +1 for the genes with zero counts) and then quantile-normalized. To make the two normalized time-series data of M154 and M1152 comparable, they were again quantile-normalized against each other. The normalized RNA-seq data are provided in **Data Set S4.**

Differentially expressed genes were identified by ANOVA using Orange (v3.2) and the bioinformatic toolkit (v), with FDR of <0.01 and a minimal fold enrichment >1 for at least one aligned time point. Genes with low expression (log2 < 5 for both strains and time points) were not considered for further analysis. The differentially expressed genes were subsequently scaled to the expression average and clustered by K-means. Visualization of genes and clusters were performed in python (v3.7) with matplotlib (v3.1.1). For this, the time-series of M145 and M1152 were aligned such that in the visual representation, the expression profiles of the two strains are aligned relative to the time point of phosphate depletion. Both DAVID (Huang et al., 2009a, 2009b) and the string database (Szklarczyk et al., 2019) was used to evaluate the function of each cluster, identifying overrepresentation of function groups based on GO annotation or text mining. Identified differential clusters or regulons were extracted from literature and plotted (**Data Set S2; Figure S8**). When we display the RNA-seq data as heatmaps (**Figure 6 and S3**) the order of genes is determined by hierarchical clustering using methods as previously described for the clustering of pathways based on metabolic activity.

Estimation of growth, uptake and production rates for *Streptomyces coelicolor* M145 and M1152 from batch fermentation data

The estimated growth, uptake and secretion rates are based on average values of online and offline measurements of batch fermentation from three parallel bioreactors for each strain.

Growth rate estimation

Both the CDW (cell dry weight) measurements and CO_2 measurements can in principle be used to estimate growth rates, as there should be a linear relationship between the CO_2 concentration and cell mass. The CO_2 concentration is measured online on a high-resolution timescale (5 min) while CDW is measured offline with a four-hour resolution starting from 18 hours after inoculation.

To estimate growth rates, we separated the growth into 5 different phases:

1. Lag phase - immediate phase after inoculation with no / low growth
2. Exponential growth - rapid growth after the initial lag phase

3. First linear growth rate - until phosphate depletion
4. Second linear growth rate – immediate phase after phosphate where there is still growth
5. Third linear growth rate – no or very low growth

From both **Figure 2A and 3A** we find a clear discrepancy between the CO2 curve and the CDW measurements after phosphate depletion. Thus, despite the lower resolution we decided to use the CDW measurements for the growth rate estimation except for the exponential growth phase.

Exponential growth rate from CO_2

The exponential growth rate was estimated by fitting an exponential curve on the form

$$X(t) = X_0 e^{\mu t}$$

to the selected region of the CO_2 measurements (**Figure S10A and S10B**), leading to an estimated growth rate of 0.25 h^{-1} ± 0.06 h^{-1} and 0.18 h^{-1} ± 0.02 h^{-1} for M145 and M1152, respectively. The uncertainty is estimated in a heuristic approach by observing the minimum and maximum values observed when changing the boundaries for the fitted function.

Linear growth rates from CDW

The growth rate is estimated by fitting linear slopes to the three different linear phases of growth (**Figure S10C and S10D**). The specific growth rate is then calculated using the following equation

$$\frac{dX}{dt} = \mu X \;\rightarrow\; \mu = \frac{1}{X} \cdot \frac{dX}{dt}$$

where μ is the growth rate, X the CDW and $\frac{dX}{dt}$ is the slope of the linear fit. Because the inverse of the CDW the rates can become very large when the cell mass is low, but we use the estimated growth rate in the exponential phase as an upper bound. Predicted growth rates and CDW estimates at the timepoints for the proteome samples are given for M145 and M1152 in **Table S1** and **Table S2**, respectively.

Uptake rates of glucose and glutamic acid

The uptake rates for glucose and glutamate were also fitted using a piecewise linear function (**Figure S10E-H**). Using the same time intervals as for the CDW estimates gave a very poor fit

for M1152 and we therefore decided to use different time intervals. From the fitted slopes we estimated the uptake rates using the equation given below:

$$\frac{dS}{dt} = \mu_s X$$

where S is the substrate, μ_s the uptake rate and X the CDW at the given time. The uptake rates at 21 hours after inoculation seems to be too low for M145 and is caused by a too low estimate of the CDW. The uptake rates for glucose and given for M145 and M1152 in **Table S1** and **Table S2**, respectively.

Undecylprodigiosin (RED) production rate

We used the same method as for the uptake rates of glucose and glutamic acid to estimate the production rate of undecylprodigiosin (RED). The M1152 did not produce any RED (as expected). However, for the M145 the amount of undecylprodigiosin was measured both using MS (mass spectrometry) and OD (optical density). From the MS data it looks like the production of RED stops after approximately 53 hours, but from the OD measurements we observe a continuous increase until the end of the experiment. The hypothesis is that RED is continuously degraded into derivatives which are still measurable using OD but not using MS because of the different masses of the derivatives. Therefore, we have extrapolated the production rate of RED using the timepoints between 40 and 53 hours to estimate the production rate of RED at 57 hours (**Figure S10I**) .

Germicidin A and B production rates

Production rates of germicidin A and B were fitted using linear regression of the last 6 data points across all three biological replicates for M145 (**Table S1**). For M1152, only the measured concentrations at 45 and 65 hours after inoculation were used to estimate the production rate of germicidin A and B (**Table S2**).

memote snapshot report of Sco-GEM

The following report (next page) was prepared by running memote version 0.9.12 in the command-line from the directory of the cloned Sco-GEM repository with the command: *memote report snapshot –custom-tests ComplementaryScripts/tests*

Independent Section

Contains tests that are independent of the class of modeled organism, a model's complexity or types of identifiers that are used to describe its components. Parameterization or initialization of the network is not required. See readme for more details.

Consistency

Stoichiometric Consistency	37.9%
Mass Balance	84.6%
Charge Balance	96.8%
Metabolite Connectivity	100.0%
Unbounded Flux In Default Medium	84.9%
Sub Total	69%

Annotation - Metabolites

Presence of Metabolite Annotation	100.0%
Metabolite Annotations Per Database	Info
pubchem.compound	18.5%
kegg.compound	82.4%
seed.compound	1.6%
inchikey	0.0%
inchi	18.6%
chebi	80.3%
hmdb	0.0%
reactome	0.0%
metanetx.chemical	88.2%
bigg.metabolite	95.9%
biocyc	70.2%

Specific Section

Covers general statistics and specific aspects of a metabolic network that are not universally applicable. See readme for more details.

SBML

SBML Level and Version	SBML Level 3 Version 1
FBC enabled	true

Basic Information

Model Identifier	
Total Metabolites	2,073
Total Reactions	2,612
Total Genes	1,778
Total Compartments	2
Metabolic Coverage	1.47

Metabolite Information

Unique Metabolites	1,836
Duplicate Metabolites in Identical Compartments	0
Metabolites without Charge	0
Metabolites without Formula	0
Medium Components	22

Reaction Information

Purely Metabolic Reactions	2,011
Purely Metabolic Reactions with Constraints	1
Transport Reactions	325

kegg.compound	100.0%
seed.compound	100.0%
inchikey	0.0%
inchi	100.0%
chebi	99.9%
hmdb	0.0%
reactome	0.0%
metanetx.chemical	99.8%
bigg.metabolite	100.0%
biocyc	99.4%
Uniform Metabolite Identifier Namespace	100.0%
Sub Total	79%

Annotation - Reactions

Presence of Reaction Annotation	100.0%
Reaction Annotations Per Database	Info
rhea	37.4%
kegg.reaction	52.4%
seed.reaction	0.0%
metanetx.reaction	79.2%
bigg.reaction	93.6%
reactome	0.0%
ec-code	64.4%
brenda	0.0%
biocyc	44.3%
Reaction Annotation Conformity Per Database	Info

Reactions With Partially Identical Annotations	0.09
Duplicate Reactions	0.00
Reactions With Identical Genes	0.48

Gene-Protein-Reaction (GPR) Associations

Reactions without GPR	342
Fraction of Transport Reactions without GPR	0.26
Enzyme Complexes	199

Biomass

Biomass Reactions Identified	10
Biomass Consistency	Info
MISC_PSEUDO	Errored
CARBOHYDRATE_PSEUDO	Errored
PROTEIN_PSEUDO_tRNA	Errored
LIPID_PSEUDO	Errored
CELL_WALL_PSEUDO	Errored
BIOMASS_SCO_tRNA	Errored
DNA_PSEUDO	Errored
RNA_PSEUDO	Errored
BIOMASS_SCO	Errored
PROTEIN_PSEUDO	Errored
Biomass Production In Default Medium	Info
MISC_PSEUDO	0.07
CARBOHYDRATE_PSEUDO	0.07
PROTEIN_PSEUDO_tRNA	0.07
LIPID_PSEUDO	0.07

seed.reaction	0.0%
metanetx.reaction	100.0%
bigg.reaction	100.0%
reactome	100.0%
ec-code	97.2%
brenda	0.0%
biocyc	100.0%
Uniform Reaction Identifier Namespace	100.0%
Sub Total	80%

Annotation - Genes

Presence of Gene Annotation	89.5%
Gene Annotations Per Database	Info
refseq	89.5%
uniprot	89.5%
ecogene	0.0%
kegg.genes	0.0%
ncbigi	0.0%
ncbigene	0.0%
ncbiprotein	0.0%
ccds	0.0%
hprd	0.0%
asap	0.0%
Gene Annotation Conformity Per Database	Info
refseq	11.1%
uniprot	100.0%

DNA_PSEUDO	0.07
RNA_PSEUDO	0.07
BIOMASS_SCO	0.07
PROTEIN_PSEUDO	0.07
Unrealistic Growth Rate In Default Medium	Info
MISC_PSEUDO	false
CARBOHYDRATE_PSEUDO	false
PROTEIN_PSEUDO_tRNA	false
LIPID_PSEUDO	false
CELL_WALL_PSEUDO	false
BIOMASS_SCO_tRNA	false
DNA_PSEUDO	false
RNA_PSEUDO	false
BIOMASS_SCO	false
PROTEIN_PSEUDO	false
Biomass Production In Complete Medium	Info
MISC_PSEUDO	123.45
CARBOHYDRATE_PSEUDO	123.45
PROTEIN_PSEUDO_tRNA	123.45
LIPID_PSEUDO	123.45
CELL_WALL_PSEUDO	123.45
BIOMASS_SCO_tRNA	123.45
DNA_PSEUDO	123.45
RNA_PSEUDO	123.45
BIOMASS_SCO	123.45
PROTEIN_PSEUDO	123.45

ncbigi	0.0%
ncbigene	0.0%
ncbiprotein	0.0%
ccds	0.0%
hprd	0.0%
asap	0.0%
Sub Total	40%

Annotation - SBO Terms

Metabolite General SBO Presence	100.0%
Metabolite SBO:0000247 Presence	99.6%
Reaction General SBO Presence	100.0%
Metabolic Reaction SBO:0000176 Presence	99.8%
Transport Reaction SBO:0000185 Presence	100.0%
Exchange Reaction SBO:0000627 Presence	100.0%
Demand Reaction SBO:0000628 Presence	100.0%
Sink Reactions SBO:0000632 Presence	Skipped
Gene General SBO Presence	89.5%
Gene SBO:0000243 Presence	89.5%
Biomass Reactions SBO:0000629 Presence	100.0%
Sub Total	89%
Total Score	77%

Total Score

CARBOHYDRATE_PSEUDO	0
PROTEIN_PSEUDO_tRNA	20
LIPID_PSEUDO	0
CELL_WALL_PSEUDO	0
BIOMASS_SCO_tRNA	0
DNA_PSEUDO	0
RNA_PSEUDO	0
BIOMASS_SCO	0
PROTEIN_PSEUDO	0
Blocked Biomass Precursors In Complete Medium	Info
MISC_PSEUDO	0
CARBOHYDRATE_PSEUDO	0
PROTEIN_PSEUDO_tRNA	20
LIPID_PSEUDO	0
CELL_WALL_PSEUDO	0
BIOMASS_SCO_tRNA	0
DNA_PSEUDO	0
RNA_PSEUDO	0
BIOMASS_SCO	0
PROTEIN_PSEUDO	0
Ratio of Direct Metabolites in Biomass Reaction	Info
MISC_PSEUDO	0.10
CARBOHYDRATE_PSEUDO	0.00
PROTEIN_PSEUDO_tRNA	0.00
LIPID_PSEUDO	0.00
CELL_WALL_PSEUDO	0.00

77%

Score per Category

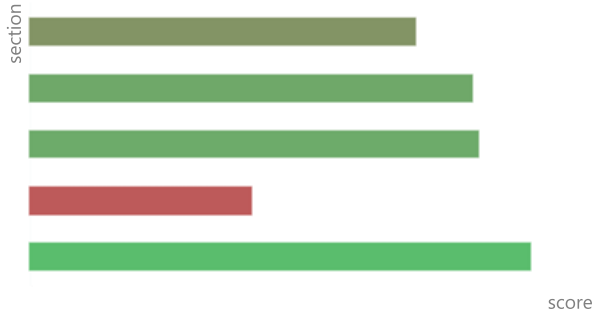

RNA_PSEUDO	0.00
BIOMASS_SCO	0.00
PROTEIN_PSEUDO	0.00
Number of Missing Essential Biomass Precursors	Info
MISC_PSEUDO	29
CARBOHYDRATE_PSEUDO	36
PROTEIN_PSEUDO_tRNA	37
LIPID_PSEUDO	37
CELL_WALL_PSEUDO	1
BIOMASS_SCO_tRNA	1
DNA_PSEUDO	1
RNA_PSEUDO	1
BIOMASS_SCO	1
PROTEIN_PSEUDO	17

Energy Metabolism

Non-Growth Associated Maintenance Reaction	Errored
Growth-associated Maintenance in Biomass Reaction	Info
MISC_PSEUDO	false
CARBOHYDRATE_PSEUDO	false
PROTEIN_PSEUDO_tRNA	false
LIPID_PSEUDO	false
CELL_WALL_PSEUDO	false
BIOMASS_SCO_tRNA	false
DNA_PSEUDO	false
RNA_PSEUDO	false
BIOMASS_SCO	false

Erroneous Energy-generating Cycles	Info
MNXM3	Skipped
MNXM63	Skipped
MNXM51	Skipped
MNXM121	Skipped
MNXM423	Skipped
MNXM6	Skipped
MNXM10	Skipped
MNXM38	Skipped
MNXM208	Skipped
MNXM191	Skipped
MNXM223	Skipped
MNXM7517	Skipped
MNXM12233	Skipped
MNXM558	Skipped
MNXM21	Skipped
MNXM89557	Skipped

Network Topology

Universally Blocked Reactions	683
Orphan Metabolites	140
Dead-end Metabolites	232
Stoichiometrically Balanced Cycles	156
Metabolite Production In Complete Medium	714
Metabolite Consumption In Complete Medium	876

Matrix Conditioning

Rank	1915
Degrees Of Freedom	697

Experimental Data Comparison

Growth Prediction	Skipped
Gene Essentiality Prediction	Skipped

Misc. Tests

Test if all metabolites have been given a name	1.00
Test CDA production	0.07
Test germicidinB production	0.37
Test growth for knockout-mutants from the transposon mutagenesis study by Xu et al.(2017)	0.76
Test germicidinA production	0.37
Test RED production	0.13
Test germicidinC production	0.33
Test that the growth rate is around 0.075	0.07
Test growth for knockout-mutants from the litterature in given environments	0.63
Test growth for WT in given environments	0.96
Test if all reactions have been given a name	1.00
Test ACT production	Errored

Environment

Python Version	3.7.3
Platform	Windows
Memote Version	0.9.12

Supplemental references

Amara, A., Takano, E., and Breitling, R. (2018). Development and validation of an updated computational model of Streptomyces coelicolor primary and secondary metabolism. BMC Genomics *19*, 519.

Andrews, S. (2016). FastQC: a quality control tool for high throughput sequence data.

Bar-Even, A., Flamholz, A., Noor, E., and Milo, R. (2012). Thermodynamic constraints shape the structure of carbon fixation pathways. Biochimica et Biophysica Acta (BBA) - Bioenergetics *1817*, 1646–1659.

Battke, F., and Nieselt, K. (2011). Mayday SeaSight: combined analysis of deep sequencing and microarray data. PLoS ONE *6*, e16345.

Bordel, S., Agren, R., and Nielsen, J. (2010). Sampling the Solution Space in Genome-Scale Metabolic Networks Reveals Transcriptional Regulation in Key Enzymes. PLOS Computational Biology *6*, e1000859.

Bystrykh, L.V., Fernández-Moreno, M.A., Herrema, J.K., Malpartida, F., Hopwood, D.A., and Dijkhuizen, L. (1996). Production of actinorhodin-related “blue pigments” by Streptomyces coelicolor A3(2). J. Bacteriol. *178*, 2238–2244.

Caspi, R., Altman, T., Billington, R., Dreher, K., Foerster, H., Fulcher, C.A., Holland, T.A., Keseler, I.M., Kothari, A., Kubo, A., et al. (2014). The MetaCyc database of metabolic pathways and enzymes and the BioCyc collection of Pathway/Genome Databases. Nucleic Acids Res *42*, D459–D471.

Chicco, D., and Jurman, G. (2020). The advantages of the Matthews correlation coefficient (MCC) over F1 score and accuracy in binary classification evaluation. BMC Genomics *21*, 6.

Claessen, D., Rink, R., Jong, W. de, Siebring, J., Vreugd, P. de, Boersma, F.G.H., Dijkhuizen, L., and Wösten, H.A.B. (2003). A novel class of secreted hydrophobic proteins is involved in aerial hyphae formation in Streptomyces coelicolor by forming amyloid-like fibrils. Genes Dev. *17*, 1714–1726.

Cokelaer, T., Pultz, D., Harder, L.M., Serra-Musach, J., and Saez-Rodriguez, J. (2013). BioServices: a common Python package to access biological Web Services programmatically. Bioinformatics *29*, 3241–3242.

Courtot, M., Juty, N., Knüpfer, C., Waltemath, D., Zhukova, A., Dräger, A., Dumontier, M., Finney, A., Golebiewski, M., Hastings, J., et al. (2011). Controlled vocabularies and semantics in systems biology. Mol. Syst. Biol. *7*, 543.

Distler, U., Kuharev, J., Navarro, P., Levin, Y., Schild, H., and Tenzer, S. (2014). Drift time-specific collision energies enable deep-coverage data-independent acquisition proteomics. Nat. Methods *11*, 167–170.

Ebrahim, A., Lerman, J.A., Palsson, B.O., and Hyduke, D.R. (2013). COBRApy: COnstraints-Based Reconstruction and Analysis for Python. BMC Systems Biology *7*, 74.

Elbourne, L.D.H., Tetu, S.G., Hassan, K.A., and Paulsen, I.T. (2017). TransportDB 2.0: a database for exploring membrane transporters in sequenced genomes from all domains of life. Nucleic Acids Research *45*, D320–D324.

Feist, A.M., Henry, C.S., Reed, J.L., Krummenacker, M., Joyce, A.R., Karp, P.D., Broadbelt, L.J., Hatzimanikatis, V., and Palsson, B.Ø. (2007). A genome-scale metabolic reconstruction for Escherichia coli K-12 MG1655 that accounts for 1260 ORFs and thermodynamic information. Molecular Systems Biology *3*, 121.

Flamholz, A., Noor, E., Bar-Even, A., and Milo, R. (2012). eQuilibrator—the biochemical thermodynamics calculator. Nucleic Acids Res *40*, D770–D775.

Fritzemeier, C.J., Hartleb, D., Szappanos, B., Papp, B., and Lercher, M.J. (2017). Erroneous energy-generating cycles in published genome scale metabolic networks: Identification and removal. PLOS Computational Biology *13*, e1005494.

Gomez-Escribano, J.P., and Bibb, M.J. (2011). Engineering Streptomyces coelicolor for heterologous expression of secondary metabolite gene clusters. Microbial Biotechnology *4*, 207–215.

Gubbens, J., Janus, M., Florea, B.I., Overkleeft, H.S., and van Wezel, G.P. (2012). Identification of glucose kinase-dependent and -independent pathways for carbon control of primary metabolism, development and antibiotic production in *Streptomyces coelicolor* by quantitative proteomics. Molecular Microbiology *86*, 1490–1507.

Haraldsdóttir, H.S., Cousins, B., Thiele, I., Fleming, R.M.T., and Vempala, S. (2017). CHRR: coordinate hit-and-run with rounding for uniform sampling of constraint-based models. Bioinformatics *33*, 1741–1743.

Hu, H., Zhang, Q., and Ochi, K. (2002). Activation of Antibiotic Biosynthesis by Specified Mutations in the rpoB Gene (Encoding the RNA Polymerase β Subunit) of Streptomyces lividans. Journal of Bacteriology *184*, 3984–3991.

Huang, D.W., Sherman, B.T., and Lempicki, R.A. (2009a). Bioinformatics enrichment tools: paths toward the comprehensive functional analysis of large gene lists. Nucleic Acids Res. *37*, 1–13.

Huang, D.W., Sherman, B.T., and Lempicki, R.A. (2009b). Systematic and integrative analysis of large gene lists using DAVID bioinformatics resources. Nat Protoc *4*, 44–57.

Jeske, L., Placzek, S., Schomburg, I., Chang, A., and Schomburg, D. (2019). BRENDA in 2019: a European ELIXIR core data resource. Nucleic Acids Res *47*, D542–D549.

Kanehisa, M. (2000). KEGG: Kyoto Encyclopedia of Genes and Genomes. Nucleic Acids Research *28*, 27–30.

Kanehisa, M., Sato, Y., Furumichi, M., Morishima, K., and Tanabe, M. (2019). New approach for understanding genome variations in KEGG. Nucleic Acids Research *47*, D590–D595.

Karp, P.D., Latendresse, M., Paley, S.M., Krummenacker, M., Ong, Q.D., Billington, R., Kothari, A., Weaver, D., Lee, T., Subhraveti, P., et al. (2016). Pathway Tools version 19.0 update: software for pathway/genome informatics and systems biology. Brief Bioinform *17*, 877–890.

Karp, P.D., Billington, R., Caspi, R., Fulcher, C.A., Latendresse, M., Kothari, A., Keseler, I.M., Krummenacker, M., Midford, P.E., Ong, Q., et al. (2019). The BioCyc collection of microbial genomes and metabolic pathways. Briefings in Bioinformatics *20*, 1085–1093.

Kaufman, D.E., and Smith, R.L. (1998). Direction Choice for Accelerated Convergence in Hit-and-Run Sampling. Operations Research *46*, 84–95.

Keesey, J.K., Bigelis, R., and Fink, G.R. (1979). The product of the his4 gene cluster in Saccharomyces cerevisiae. A trifunctional polypeptide. J. Biol. Chem. *254*, 7427–7433.

Kieser, T., Bibb, M.J., Buttner, M.J., Chater, K.F., and Hopwood, D.A. (2000). Practical Streptomyces Genetics (Norwich, UK: John Innes Foundation).

Kim, D., Langmead, B., and Salzberg, S.L. (2015). HISAT: a fast spliced aligner with low memory requirements. Nat. Methods *12*, 357–360.

King, Z.A., Lu, J., Dräger, A., Miller, P., Federowicz, S., Lerman, J.A., Ebrahim, A., Palsson, B.O., Lewis, N.E., and J., H. (2016). BiGG Models: A platform for integrating, standardizing and sharing genome-scale models. Nucleic Acids Research *44*, D515–D522.

Kumelj, T., Sulheim, S., Wentzel, A., and Almaas, E. (2019). Predicting Strain Engineering Strategies Using iKS1317: A Genome-Scale Metabolic Model of *Streptomyces coelicolor*. Biotechnol. J. *14*, 1800180.

Li, H., Handsaker, B., Wysoker, A., Fennell, T., Ruan, J., Homer, N., Marth, G., Abecasis, G., Durbin, R., and 1000 Genome Project Data Processing Subgroup (2009). The Sequence Alignment/Map format and SAMtools. Bioinformatics *25*, 2078–2079.

Liao, Y., Smyth, G.K., and Shi, W. (2014). featureCounts: an efficient general purpose program for assigning sequence reads to genomic features. Bioinformatics *30*, 923–930.

Lieven, C., Beber, M.E., Olivier, B.G., Bergmann, F.T., Ataman, M., Babaei, P., Bartell, J.A., Blank, L.M., Chauhan, S., Correia, K., et al. (2018). Memote: A community-driven effort towards a standardized genome-scale metabolic model test suite. BioRxiv 350991.

Love, M.I., Huber, W., and Anders, S. (2014). Moderated estimation of fold change and dispersion for RNA-seq data with DESeq2. Genome Biol. *15*, 550.

Maurer, K.H., Pfeiffer, F., Zehender, H., and Mecke, D. (1983). Characterization of two glyceraldehyde-3-phosphate dehydrogenase isoenzymes from the pentalenolactone producer Streptomyces arenae. J. Bacteriol. *153*, 930–936.

Megchelenbrink, W., Huynen, M., and Marchiori, E. (2014). optGpSampler: An Improved Tool for Uniformly Sampling the Solution-Space of Genome-Scale Metabolic Networks. PLOS ONE *9*, e86587.

Michael Waskom, Olga Botvinnik, Drew O'Kane, Paul Hobson, Joel Ostblom, Saulius Lukauskas, David C Gemperline, Tom Augspurger, Yaroslav Halchenko, John B. Cole, et al. (2018). mwaskom/seaborn: v0.9.0 (July 2018) (Zenodo).

Moretti, S., Martin, O., Van Du Tran, T., Bridge, A., Morgat, A., and Pagni, M. (2016). MetaNetX/MNXref – reconciliation of metabolites and biochemical reactions to bring together genome-scale metabolic networks. Nucleic Acids Res *44*, D523–D526.

NCBI Resource Coordinators (2017). Database Resources of the National Center for Biotechnology Information. Nucleic Acids Research *45*, D12–D17.

Nieselt, K., Battke, F., Herbig, A., Bruheim, P., Wentzel, A., Jakobsen, Ø.M., Sletta, H., Alam, M.T., Merlo, M.E., Moore, J., et al. (2010). The dynamic architecture of the metabolic switch in Streptomyces coelicolor. BMC Genomics *11*, 10.

Noor, E. (2018). Removing both Internal and Unrealistic Energy-Generating Cycles in Flux Balance Analysis. ArXiv:1803.04999 [q-Bio].

Noor, E., Haraldsdóttir, H.S., Milo, R., and Fleming, R.M.T. (2013). Consistent Estimation of Gibbs Energy Using Component Contributions. PLOS Computational Biology *9*, e1003098.

Okonechnikov, K., Conesa, A., and García-Alcalde, F. (2016). Qualimap 2: advanced multi-sample quality control for high-throughput sequencing data. Bioinformatics *32*, 292–294.

Rappsilber, J., Mann, M., and Ishihama, Y. (2007). Protocol for micro-purification, enrichment, pre-fractionation and storage of peptides for proteomics using StageTips. Nat Protoc *2*, 1896–1906.

Rauch, G., Ehammer, H., Bornemann, S., and Macheroux, P. (2008). Replacement of two invariant serine residues in chorismate synthase provides evidence that a proton relay system is essential for intermediate formation and catalytic activity: Proton relay system in chorismate synthase. FEBS Journal *275*, 1464–1473.

Saier, M.H., Reddy, V.S., Tsu, B.V., Ahmed, M.S., Li, C., and Moreno-Hagelsieb, G. (2016). The Transporter Classification Database (TCDB): recent advances. Nucleic Acids Res *44*, D372–D379.

Sánchez, B.J., Zhang, C., Nilsson, A., Lahtvee, P.-J., Kerkhoven, E.J., and Nielsen, J. (2017). Improving the phenotype predictions of a yeast genome-scale metabolic model by incorporating enzymatic constraints. Molecular Systems Biology *13*, 935.

Schendel, F.J., Mueller, E., Stubbe, J., Shiau, A., and Smith, J.M. (1989). Formylglycinamide ribonucleotide synthetase from Escherichia coli: cloning, sequencing, overproduction, isolation, and characterization. Biochemistry *28*, 2459–2471.

Szklarczyk, D., Gable, A.L., Lyon, D., Junge, A., Wyder, S., Huerta-Cepas, J., Simonovic, M., Doncheva, N.T., Morris, J.H., Bork, P., et al. (2019). STRING v11: protein-protein association networks with increased coverage, supporting functional discovery in genome-wide experimental datasets. Nucleic Acids Res. *47*, D607–D613.

Talfournier, F., Stines-Chaumeil, C., and Branlant, G. (2011). Methylmalonate semialdehyde dehydrogenase from Bacillus subtilis : substrate specificity and coenzyme A binding. J. Biol. Chem. jbc.M110.213280.

The UniProt Consortium (2019). UniProt: a worldwide hub of protein knowledge. Nucleic Acids Res *47*, D506–D515.

Thiele, I., and Palsson, B.Ø. (2010). A protocol for generating a high-quality genome-scale metabolic reconstruction. Nature Protocols *5*, 93–121.

Virtanen, P., Gommers, R., Oliphant, T.E., Haberland, M., Reddy, T., Cournapeau, D., Burovski, E., Peterson, P., Weckesser, W., Bright, J., et al. (2020). SciPy 1.0: fundamental algorithms for scientific computing in Python. Nat Methods *17*, 261–272.

Wang, H., Marcišauskas, S., Sánchez, B.J., Domenzain, I., Hermansson, D., Agren, R., Nielsen, J., and Kerkhoven, E.J. (2018). RAVEN 2.0: A versatile toolbox for metabolic network reconstruction and a case study on Streptomyces coelicolor. PLOS Computational Biology *14*, e1006541.

Wentzel, A., Bruheim, P., Øverby, A., Jakobsen, Ø.M., Sletta, H., Omara, W.A.M., Hodgson, D.A., and Ellingsen, T.E. (2012). Optimized submerged batch fermentation strategy for systems scale studies of metabolic switching in Streptomyces coelicolor A3(2). BMC Systems Biology *6*, 59.

Wessel, D., and Flügge, U.I. (1984). A method for the quantitative recovery of protein in dilute solution in the presence of detergents and lipids. Anal. Biochem. *138*, 141–143.